VOLUMETRIC TOMOGRAPHIC IMAGING

A DISSERTATION
SUBMITTED TO THE DEPARTMENT OF APPLIED PHYSICS
AND THE COMMITTEE ON GRADUATE STUDIES
OF STANFORD UNIVERSITY
IN PARTIAL FULFILLMENT OF THE REQUIREMENTS
FOR THE DEGREE OF
DOCTOR OF PHILOSOPHY

Grant Morey Stevens
December 2000

I certify that I have read this dissertation and that in my opinion it is fully adequate, in scope and quality, as a dissertation for the degree of Doctor of Philosophy.

Norbert Pelc
(Principal Adviser)

I certify that I have read this dissertation and that in my opinion it is fully adequate, in scope and quality, as a dissertation for the degree of Doctor of Philosophy.

Sebastian Doniach

I certify that I have read this dissertation and that in my opinion it is fully adequate, in scope and quality, as a dissertation for the degree of Doctor of Philosophy.

Sandy Napel

Approved for the University Committee on Graduate Studies:

Abstract

With the recent advances in digital flat-panel x-ray detector technology, interest has been strengthened in the application of volumetric tomographic imaging to medicine. This dissertation deals with the development of a test-bed digital volumetric tomography system, and its application to in-vitro circular tomosynthesis. Issues addressed include: sensitivity to geometrical misalignments, software-based correction for misalignments, and filtering to improve reconstructed image quality. In addition, clinically relevant phantoms were imaged in order to examine the potential application of tomosynthesis to mammography and imaging of the upper cervical spine.

An analysis of the system's sensitivity to geometrical misalignment laid the groundwork for a software correction technique. By using the x-ray system itself to measure the system geometry using a calibration phantom or fiducial markers, along with a projection simulator, high quality tomosynthesis images can be produced without requiring precise mechanical alignment of the system. Further improvement in the reconstructed images can be obtained through filtering of the projected data in order to alter the 3D impulse response of the system. An analysis of the Fourier space sampling of circular tomosynthesis leads to the development of a filter which allows a circular motion system to mimic systems using more complex motions. In particular, a filter is constructed which blurs out-of-plane objects into a disk rather than a ring, while faithfully reproducing in-plane objects. Computer simulations and noise analysis were used to further characterize this filtering technique. Its use in realistic imaging conditions demonstrated the importance of removing overlying structures in complex objects.

Use of the volumetric tomography system with the geometry correction technique

allows the generation of tomosynthesis images with in-plane spatial resolution equaling the predicted limit, even with an unaligned system. The disk-filter is successful in improving the visualization of in-plane objects by more uniformly blurring out-of-plane objects. Images of anatomic phantoms with the test-bed system are encouraging. Application to mammography would provide 3D localization of calcifications and removal of overlying structures. Tomosynthesis of the upper cervical spine improves the imaging of vertebrae with reduced confusion from overlying jaw structures.

Acknowledgements

I would first like to express my gratitude for the contributions from the members of my reading committee: Dr. Seb. Doniach, Dr. Sandy Napel, and Dr. Norbert Pelc; and for the contributions from the additional members of my orals committee: Dr. Robert Byer and Dr. Dwight Nishimura (who was kind enough to act as chairman of my orals committee). Their input has been very beneficial, and this dissertation has been much improved by their assistance.

I would especially like to thank Norbert for acting as my research advisor. Norbert has made my learning experience a very memorable one. I thoroughly enjoyed my time at Stanford, and a large part of that was because of my work with Norbert.

During this research project, I have received a large amount of help from a great number of people. I am thankful for the contributions of Dr. Robyn Birdwell, Dr. Debra Ikeda, Dr. Fred Dirbas, Dr. Teri Longacre, Barbara Smith, and Dr. Russell Vang in investigating the application of tomosynthesis to mammographic imaging, and Dr. Chris Beaulieau and Dr. Martin Murphy in the application to cervical spine imaging. Their insight into potential clinical applications is greatly appreciated.

All of the members of the Lucas Center have made my time at Stanford very enjoyable. In particular, I would like to thank Dr. Rebecca Fahrig for our research collaborations on several x-ray projects. I am indebted to Dr. Marc Alley and Dr. Tom Brosnan for their friendship and support. Tom (who could not care less whether or not the margins in this document were correct) deserves a medal for his patience and kindness to me while I completed this work. Donna Cronister managed to keep the Lucas Center running, even with all of my pestering. Long after I have forgotten the details described in the pages that follow this one, I will remember the people at

Stanford who made my time there special.

Our collaboration with GE Medical Systems has been a very rewarding aspect of this project. While I was an intern at GE, Dr. Paul Granfors and Rowland Saunders played crucial roles in my research. Rowland, without whose selfless help this project would not have been possible, deserves more thanks than I can give here. In addition, many scientists at GE Corporate Research & Development were very supportive of the project. I would like to thank Mehmet Yavuz, in particular, for modifying a backprojection reconstruction routine for our system.

In addition to the technical support, this research project has received financial support from a number of sources: GE Medical Systems, Lunar Corporation, the Lucas Foundation, and the Stanford-NIH Graduate Training Program in Biotechnology.

Outside of the academic realm, my time at Stanford has been incredible. I would like to thank the members of the Stanford University Cycling Team for all of the wonderful hours spent hammering away on the roads around the Bay Area. My fiancée, Amy Gall, has supported me in all of my endeavors, and has made all of the ups and downs of graduate school better by her presence.

My path to Stanford was made much smoother by many excellent role models in the early part of my academic career. In particular, Dr. Hugh Haskell and Dr. Susan Schmidt were excellent mentors at the North Carolina School of Science and Mathematics. Dr. Scott Habermehl and Dr. Plinio Santos-Filho were tremendous role models as scientists, as well as good friends, while working in Dr. Gerald Lucovsky's research group at North Carolina State University.

This section cannot be complete without acknowledging my family. My parents tried to instill a great respect for education in my sister, Vanessa, and I. We must have listened, since we will both complete our doctoral degrees this year. This dissertation is dedicated to John and Dale Stevens, as a small token of my appreciation for everything that they have done.

Contents

List of Tables

List of Figures

Chapter 1

Introduction

1.1 Scope of the Thesis

The recent advances in digital x-ray detector technology have the potential to improve the performance of diagnostic x-ray imaging. Not only will radiologists be able to collect conventional radiographs digitally, but they will also have the option of collecting images for which conventional x-ray detectors were inadequate. One example of this is tomosynthesis, in which a number of radiographs are collected while the x-ray tube and detector are moved through a specific path about the patient. Modification of the manner in which these images are combined allows the user to select a plane in the reconstructed image to be in focus. Objects lying outside this plane are blurred, according to the type of motion used during the image acquisition. A single dataset can be used to generate many reconstructed images, each with a different focal plane. In addition, because the images are added during the reconstruction process, the overall dose can be similar to that from a single radiograph.

This dissertation is focused on the development of a volumetric tomography system, and the application of this system for digital circular tomosynthesis. A demonstration of the system's sensitivity to geometrical misalignments motivates the need for a correction technique. By performing this correction in software, an inexpensive, adjustable gantry can be used. Further improvement in image quality can be obtained using a filtering technique described in this dissertation. Finally, potential clinical applications in mammography and imaging of the cervical spine are examined.

1.2 Contents and Organization

A review of tomosynthesis imaging is given in Chapter 2. We examine the principles of tomosynthesis from both spatial domain and frequency domain perspectives. The volumetric tomography system we have developed for circular tomosynthesis applications is based on a prototype digital x-ray detector. While a detailed description of digital x-ray detectors is beyond the scope of this dissertation, a short description is given in order to motivate how this new technology is reviving interest in imaging modalities such as tomosynthesis, which did not work well with conventional x-ray detectors.

The system that we have developed for volumetric tomography is described in Chapter 3. This apparatus is based on a flat-panel detector and an x-ray tube mounted on an adjustable gantry. This system can be used to image phantoms, which are placed on a custom, computer-controlled, rotational positioning stage. In addition to using this system for circular tomosynthesis, radiographic and volumetric computed tomography data can be collected (without altering the position of the phantom) by changing the position of the gantry.

Chapter 4 gives a demonstration of the sensitivity of the system to geometrical misalignments. Rather than building the tomography system with an expensive, precisely aligned gantry, our approach is to use a low cost gantry. Because of the less precise mechanical alignment of the system, however, uncorrected image reconstructions have poor image quality. This chapter describes an analysis designed to highlight the effects of these misalignments.

The errors shown in Chapter 4 can be corrected using a technique described in Chapter 5. In order to correct for the errors, the geometry of the system must be precisely known. A technique is described to fit the geometry using simulated and measured projections compared in an iterative fashion. Once a fit is achieved, the data can be remapped prior to image reconstruction. The goal of this chapter is not to accurately measure the geometry of the system, but rather to adequately correct the errors in the reconstructed images resulting from the geometrical misalignments.

Chapter 6 describes a filtering technique which can be used to modify the impulse response of circular tomosynthesis. Through a Fourier space approach, the blur function for off-plane objects can be altered. In particular, the technique is used to change the blur function from a ring to a disk in order to reduce the conspicuity of off-plane objects. A noise analysis is presented, as are applications of the filtering technique to simulated and experimental data.

Possible clinical applications for the tomosynthesis imaging techniques presented in this dissertation are discussed in Chapter 7. In particular, mammographic imaging and imaging of the cervical spine are examined. After a brief description of the limitations of conventional imaging techniques for these anatomies, tomosynthesis results are presented for experimental phantoms.

Finally, Chapter 8 summarizes the contributions of this dissertation. This chapter outlines possible future work in this area.

In addition, Appendix A consists of a paper indirectly related to this work. It describes a detector with which the polychromatic nature of x-ray imaging is exploited, rather than ignored. This may have several applications, such as quantification of the amount of bone present, when screening for and monitoring osteoporosis.

Chapter 2

Review: X-ray Imaging

This chapter gives a review of x-ray tomosynthesis imaging. We examine the fundamentals of this type of imaging first in the spatial domain. A second approach describes tomosynthesis from a frequency domain perspective. Circular tomosynthesis falls somewhere between radiography and computed tomography (CT) in terms of frequency space coverage, and hence in terms of the ability to faithfully reconstruct the object being imaged. A brief overview of digital x-ray detectors is given to motivate the re-emergence of tomosynthesis in medical imaging.

2.1 X-ray Imaging Overview

X-ray imaging began just over 100 years ago, when William K. Roentgen discovered x-rays in 1895. Interest in the newly discovered phenomenon was great, with over fifty books and one thousand scientific articles appearing on x-rays in the next year [1]. Scientists quickly realized the usefulness of transmitting these new rays through the human body in order to see within, with the first medical x-ray image published less than three months after the x-ray discovery [2], and the first x-ray units being placed in hospitals less than six months after the discovery [3].

Conventional medical imaging with x-rays is based on transmission through the patient. X-ray transmission is useful because structures in the body differ in their x-ray absorption, and thus alter the transmitted x-ray beam based on their particular absorption properties. The monoenergetic transmission of an x-ray beam along path s through an object of thickness t with an (energy-dependent) attenuation coefficient μ can be written as:

$$I = I_o e^{-\int_0^t \mu(s)\, ds}, \tag{2.1}$$

where I_o and I are the number of x-rays incident on, and transmitted through the body, respectively. The projected attenuation coefficient is then the natural logarithm of the measured transmission:

$$\int_0^t \mu(s)\, ds = \log \frac{I_o}{I}. \tag{2.2}$$

X-ray beams typically contain x-rays with a range of energies, which adds a layer of complexity to their transmission behavior. The energy dependence of x-ray attenuation is utilized in some techniques, such as dual energy x-ray absorptiometry used to measure bone mineral density (as in Appendix A). In CT, a correction step is usually performed to correct for the beam hardening effect of polychromatic x-rays, and the energy dependence is ignored in radiography. For the tomosynthesis work presented here, we ignore the effects of the polychromatic beam since our imaging goals are qualitative rather than quantitative.

A radiographic image is generated from the measured transmission of an x-ray beam from a single source position, yielding a 2D image. Equations (2.1) and (2.2) are true for a radiograph for each pixel on the detector. Clearly, no depth information is retained with a single projection, i.e., the 3D x-ray attenuation coefficient is projected onto a 2D plane. This can be analyzed in Fourier space. Assuming parallel rays, the Projection-Slice Theorem (also known as the Central Slice Theorem) states that the region in Fourier space sampled by a 2D projection is the plane through the origin and orthogonal to the direction of the x-rays. This is shown in Fig. 2.1, and is proven here. Consider the transmission of a 2D parallel beam through a 3D object, with the

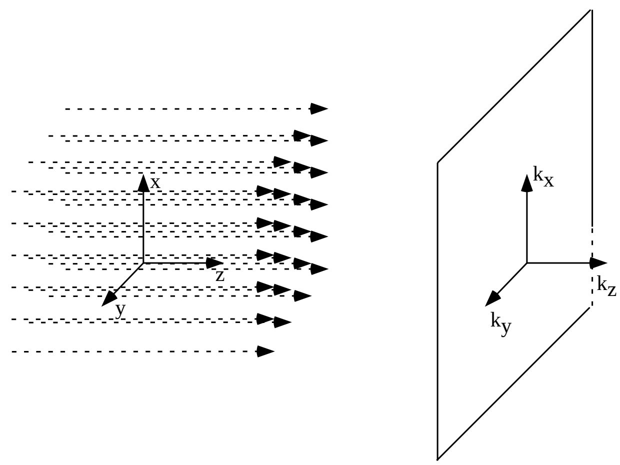

Figure 2.1: Frequency space sampling for a 2D parallel ray projection. The left side illustrates the direction of a projection in image space and the right side shows the planar region in k-space sampled by the projection.

rays parallel to the z-axis. The 2D measured signal is:

$$I(x, y) = I_o(x, y)e^{-\int_0^t \mu(x,y,z)\,dz}, \tag{2.3}$$

As before, ignoring beam hardening,

$$\int_0^t \mu(x, y, z)\,dz = \log \frac{I_o(x, y)}{I(x, y)} \equiv L(x, y), \tag{2.4}$$

where $L(x, y)$ is the measured log signal. Let $M(k_x, k_y, k_z)$ denote the 3D Fourier transform of the object's attenuation coefficient. That is,

$$M(k_x, k_y, k_z) = \int\int\int \mu(x, y, z)e^{-i2\pi(k_x x + k_y y + k_z z)}\,dx\,dy\,dz. \tag{2.5}$$

On the plane $k_z = 0$, Eq. (2.5) becomes:

$$M(k_x, k_y, 0) = \int\int\int \mu(x, y, z)e^{-i2\pi(k_x x + k_y y)}\,dx\,dy\,dz. \tag{2.6}$$

This can be rearranged:

$$M(k_x, k_y, 0) = \int \int \left(\int \mu(x, y, z)\, dz \right) e^{-i2\pi(k_x x + k_y y)}\, dx\, dy. \tag{2.7}$$

Substituting Eq. (2.4) into Eq. (2.7) yields:

$$M(k_x, k_y, 0) = \int \int L(x, y) e^{-i2\pi(k_x x + k_y y)}\, dx\, dy, \tag{2.8}$$

which is the 2D Fourier transform of the log signal. Thus the 2D Fourier transform of the projection is a 2D slice through the 3D Fourier transform of the object's x-ray attenuation, i.e. the 2D projection samples the plane in Fourier space through the origin, orthogonal to the direction of projection. Because only these frequencies are measured in a radiographic projection, the image yields no spatial information along the projection direction. This type of imaging suffers from the inability to differentiate a structure of interest in the body from overlying structures.

At the other end of the x-ray imaging spectrum, computed tomography (CT) uses many collected projection images to recover the spatial information in the third dimension. In conventional 2D CT, many 1D projections are collected over at least 180° and used to reconstruct a 2D slice through the 3D x-ray attenuation coefficient distribution. Proper collimation of the x-ray beam approximately limits the radiation exposure to the slice being imaged (except for x-ray scattering events). Assuming parallel rays, each 1D projection measures the radial line in Fourier space orthogonal to the direction of projection, as shown in Fig. 2.2. This is the 1D analog of the plane in Fourier space measured by a 2D radiographic image. Collecting data through at least 180° about the body fills in all of k-space, assuming an infinite number of views. This data can be Fourier transformed to reconstruct the slice through the body.

It should be noted that CT does not sample Fourier space evenly, as can be seen in Fig. 2.2. This is important because it affects backprojection, which is a common reconstruction technique. In this approach, the measured signal at each detector element is projected back along the original projection line. It can be shown that backprojection is equivalent to depositing all the energy of the measured Fourier

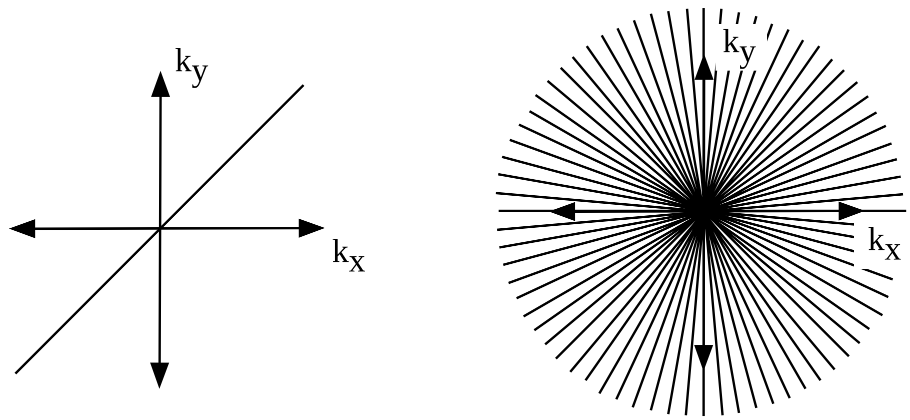

Figure 2.2: Fourier space coverage for a single 1D projection in a CT dataset (left) and for many projections (right).

samples onto the Fourier transform of the image. When this is done for all of the data, the uneven sampling in Fourier space results in a poor reconstruction. Correction for this uneven sampling density improves the quality of reconstructed images [4].

In addition, computed tomography can be used to image a volume of the body, rather than a single slice (or series of slices). Volumetric CT (VCT) uses a 2D detector instead of the conventional 1D CT detector to collect many 2D projections, which are used to reconstruct the 3D x-ray attenuation coefficient.

In the case of non-parallel rays, the Projection-Slice Theorem no longer holds. In the 2D case, exact backprojection reconstruction techniques exist for the fan-beam geometry. This is not true for the 3D cone-beam geometry.

Volumetric computed tomography is made more feasible by technological developments in 2D detectors. Digital flat-panel detector technology allows the projection images formerly recorded by x-ray film-screen systems to be directly acquired in digital format, and allows isotropic resolution 2D CT detectors. This technology also enables imaging techniques which were difficult to perform using older systems. One type of imaging, tomosynthesis, can be used as an intermediate modality between radiography (2D) and CT (2D or 3D) imaging. Tomosynthesis, as will be shown, falls in between radiography and CT in terms of frequency space coverage, and therefore in terms of the ability to faithfully reconstruct an object. We use the term volumetric tomography to describe the general 3D tomographic imaging including VCT and tomosynthesis.

2.2 Tomosynthesis

Radiography yields high spatial resolution in two dimensions and no resolution in the third. While CT provides spatial resolution in all three dimensions, it typically has lower resolution in all three dimensions than the in-plane resolution of conventional radiography. This, however, is a property of most commercially available systems, rather than a fundamental property of CT. In comparison, tomosynthesis [5] can be used to generate 3D images with high spatial resolution in two dimensions, and limited resolution in the third. Generally, this results in focused image reconstructions of objects lying on the plane of interest, while objects lying outside the focal plane are blurred. In comparison, the entire object (including objects not on the plane of interest) appears sharp in radiography, and objects not on the plane of interest are removed in CT. In order to understand tomosynthesis, it is useful to first examine motion tomography because tomosynthesis is an extension of motion tomography. While the resolution in the third dimension is limited in tomosynthesis and motion tomography, this type of imaging still has a clinical role because of the more flexible imaging geometry, higher in-plane resolution, lower data collection requirements, and lower cost of the equipment as compared to CT.

Motion tomography [4] is performed by moving the x-ray tube and detector during the exposure through a specific path in opposite directions about a stationary body. An example of a motion tomography system incorporating a circular path for the x-ray tube and detector is shown in Fig. 2.3. There is a mechanical fulcrum plane, which is always in focus on the detector. Objects in the body lying on the focal plane (which can be selected by moving the patient relative to the tube and detector prior to the exposure) always project onto the same location on the detector, while objects off this plane have projections which move on the detector in a path dictated by the path of the x-ray tube and detector. The x-ray tube is on during the entire motion

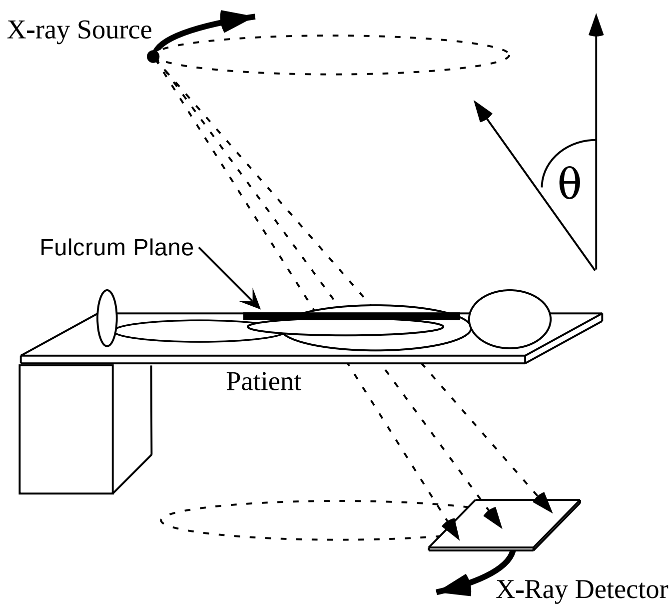

Figure 2.3: Example of a motion tomography system using circular motion. The projection angle θ is equal to half the tomographic angle.

path, and a single integrated image is recorded. After the extended exposure, the image consists of a sharp image of the focal plane, and superimposed blurry images of other planes in the object. While the energy from off-focal-plane objects is still present in the image, the blurring improves visualization of the details of objects lying in-plane because the contrast of the rest of the volume is decreased by the blurring.

The relative motion of the tube and detector and the location of the object define the focal plane, and a new exposure must be taken for a different focal plane. In addition, the extent of the motion determines the effective thickness of the slice through the object which is in focus in the image. The motion path can be characterized by the tomographic angle, as shown in Fig 2.3. The tomographic angle is twice the angle between the axis of symmetry for the motion and the central ray of the beam at the most extreme portion of the motion path. Therefore, the slice thickness will vary as a function of the tomographic angle. The slice thickness is a difficult parameter to uniquely define because of the nature of the blurring. We define the slice thickness as the range in plane heights for which the extent of a blurred object on this plane is less than a characteristic distance d_c. A natural choice for d_c is some fraction of a pixel in the image. As is derived below for circular motion, the extent of the blurring is proportional to $\tan\theta$. Therefore, the slice thickness is inversely proportional to $\tan\theta$. Alternatively, a Fourier space derivation can be made [6], which yields the same dependency on the tomographic angle. As the tomographic angle decreases, the slice thickness increases.

The type of blurring is dependent on the type of motion used during data collection. Simple linear motion blurs objects in one dimension only. This leads to linear streak artifacts, caused by high contrast off-focal-plane objects, which can obscure useful information in the images [7]. Circular motion of the source and detector results in out-of-plane points being blurred into rings, while more complex motions, such as hypocycloidal, result in blur functions which are more appealing (i.e., less disturbing) to the observer [8]. More complex motions, however, require more costly equipment and can lead to longer exposures [9].

One drawback of motion tomography is that each extended exposure of the patient produces only one focal plane image, even though the entire volume is irradiated. If multiple planar images are needed, then the patient would have to be exposed to ionizing radiation each time. Tomosynthesis provides a way to circumvent this requirement, so that a single dataset can be used to reconstruct any plane. Rather than collecting a single exposure while the x-ray tube and detector are moving about the body, one could take a series of radiographs during the same time period. Before digital x-ray detectors, this was performed with rapid film changers or image intensifiers with television cameras to capture the images. Adding up the radiographs yields the same fulcrum plane image as motion tomography. One can, however, select the focal plane retrospectively by altering the manner in which the images are combined. Thus, a single exposure can be used to generate an image of any slice through the body. Because the images are added during reconstruction, the dose can be made similar to that of a single radiograph or tomography image. As compared to CT, the imaging geometry of tomosynthesis is more flexible, so that imaging can still be performed in areas where human anatomy dictates requirements on the imaging geometry, such as in mammography.

The requirements for tomosynthesis do not differ greatly from other x-ray techniques. The mechanical engineering required for the gantry of a clinical tomosynthesis scanner is equivalent to that for motion tomography. The radiographic (or fluoroscopic) detector does not need to be modified from the existing design, except for the need to rapidly capture a series of views. If the number of views is small or if the motion per view is large, x-ray tube pulsing may be needed.

As described above, the blurring of the out-of-plane objects is dependent on the type of motion used during image acquisition. We focus, in particular, on circular tomosynthesis. This type of tomosynthesis is favorable both because of the improved blurring relative to linear motion, and because of the theoretical framework which it shares with CT. In addition, as will be shown, the information content is equivalent to more complex motions such as hypocycloidal. This allows a circular motion system to mimic systems with more complex mechanical requirements.

2.2.1 Circular Tomosynthesis

The volumetric tomography system we have developed can be used for circular tomosynthesis applications. We give here a more detailed description of circular tomosynthesis, both in the spatial and frequency domains. This approach demonstrates the continuum of x-ray imaging from 2D imaging to 3D approaches, with circular tomosynthesis falling somewhere between radiography and VCT.

Circular tomosynthesis images are generated from a dataset consisting of 2D projections taken while the x-ray tube and detector rotate in a circular path about the patient. This is similar to the motion for CT, except that the axis of rotation for tomosynthesis is not perpendicular to the x-rays paths, as it is in CT. While in a clinical system the tube and detector move about a stationary object (i.e., patient), it is equivalent (up to a rotation of the detector) to rotating the object while the tube and detector are fixed in space at an angle relative to the object's axis of rotation. This is the case for our system, as shown in Fig. 2.4. The tomographic angle for tomosynthesis is in the range $(0, \pi)$, with an angle of 0 equivalent to A-P projection radiography, and π equivalent to VCT.

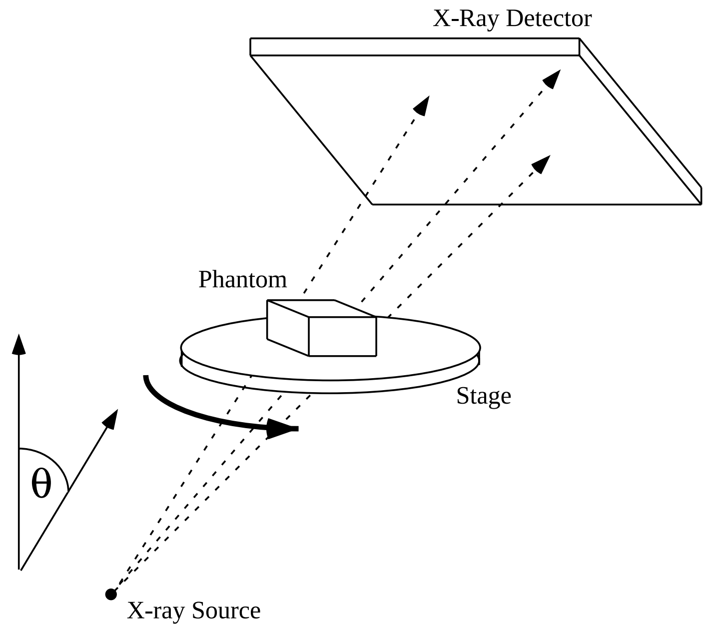

Figure 2.4: Circular tomosynthesis system with stationary tube and detector. The projection angle θ is equal to half the tomographic angle.

Each of the projections in the dataset looks like a conventional radiograph, albeit at an angle relative to the conventional imaging plane. We define the conventional imaging plane as a plane which is orthogonal to the axis of rotation of the positioning stage. As in CT, the information in the additional spatial dimension comes from the combination of all the projections. For our description of a circular system, we will focus on a phantom-based system in which the object is rotated. The same formalism, however, can be adapted to the clinical scanner in which the x-ray tube and detector are rotated while the patient remains stationary.

Spatial Domain Analysis

We first approach tomosynthesis from a spatial domain (i.e., real space) analysis. Consider a perfectly aligned system as shown in Fig. 2.4, with the x-ray tube at height z_t and the detector at height z_d. At tomographic angle 2θ (θ denotes the angle of the central ray of the x-ray beam relative to the axis of rotation of the positioning stage), the tube and detector are located at $(z_t \sin\theta, 0, z_t \cos\theta)^T$ and $(z_d \sin\theta, 0, z_d \cos\theta)^T$, respectively. Consider a point object located at $(x_o, y_o, z_o)^T$. We will examine the effect of circular tomosynthesis on this point for reconstructions at a plane containing the point and for a plane away from this point. With the object at angle ϕ, the projection of the point object falls on the detector at:

$$\overrightarrow{x_p} = \frac{\begin{bmatrix} (x_o \cos\phi - y_o \sin\phi)(z_t \cos^2\theta - z_d) - z_t \sin\theta(z_o \cos\theta - z_d) \\ (x_o \sin\phi + y_o \cos\phi)(z_t - z_d) \\ -(x_o \cos\phi - y_o \sin\phi) z_t \cos\theta \sin\theta - z_d(z_o - z_t \cos\theta) + z_o z_t \sin^2\theta \end{bmatrix}}{z_t - (x_o \cos\phi - y_o \sin\phi)\sin\theta - z_o \cos\theta}. \tag{2.9}$$

While Eq. (2.9) gives the location of the detector pixel on which the projection ray falls, it is useful to re-express this location in terms of a coordinate system in the reference frame of the detector. This is beneficial, in particular, when examining the backprojection of measured images. In terms of the natural coordinate system of the detector (i.e., a 2D coordinate system on the surface of the detector with the origin at the detector center), the projection data is located at:

$$\overrightarrow{u} = \frac{\begin{bmatrix} (z_t - z_d)((x_o \cos\phi - y_o \sin\phi)\cos\theta - z_o \sin\theta) \\ (z_t - z_d)(x_o \sin\phi + y_o \cos\phi) \end{bmatrix}}{z_t - (x_o \cos\phi - y_o \sin\phi)\sin\theta - z_o \cos\theta}. \tag{2.10}$$

Consider now the simple backprojection of this projection data to a plane at height $z = z_b$. This is equivalent to asking what a planar object would have to look like to give rise to the projection data from the actual object. This may seem trivial since we are examining the behavior for a point object (which by definition is already a planar object), but this methodology extends to a 3D object broken down into small voxels. On this plane, in order for a point object to project onto the location given by Eqs. (2.9) and (2.10), it must be located (for positioning stage at angle ϕ) at:

$$\overrightarrow{x_b} = \begin{bmatrix} x_o \frac{z_b - z_t\cos\theta}{z_o - z_t\cos\theta} - \frac{(z_b - z_o) z_t \cos\phi \sin\theta}{z_o - z_t \cos\theta} \\ y_o \frac{z_b - z_t\cos\theta}{z_o - z_t\cos\theta} - \frac{(z_b - z_o) z_t \sin\phi \sin\theta}{z_o - z_t \cos\theta} \\ z_b \end{bmatrix}. \tag{2.11}$$

Equation (2.11) describes the intersection of the backprojection ray with the plane at height $z = z_b$. If the reconstruction plane includes the point object, i.e., $z_b = z_o$, then Eq. (2.11) reduces to $(x_o, y_o, z_o)^T$, and the image of the object focuses to a point in its original position, i.e., $\overrightarrow{x_b} = \overrightarrow{x_o}$. If the reconstruction plane is at a different plane, the (x, y) locations given by Eq. (2.11) fall on a circle. Thus, the off-plane reconstruction of the point object (in the limit of many views) is a ring with center $(x_o \frac{z_b - z_t \cos\theta}{z_o - z_t \cos\theta}, y_o \frac{z_b - z_t \cos\theta}{z_o - z_t \cos\theta}, z_b)^T$ and radius $\frac{(z_b - z_o) z_t \sin\theta}{z_o - z_t \cos\theta}$.

Equation (2.11) shows that in-plane point objects are faithfully reconstructed in circular tomosynthesis, while off-plane point-objects are blurred into rings in the limit of an infinite number of views. In the case of a finite number of views, off-plane objects are blurred into a discretely-sampled ring (i.e., a dataset with N views results in N points lying on the ring that would be produced by an infinite number of views). The blurring is 2D spatially invariant in that the blurring does not depend on the (x, y) location of the object, i.e., the blur radius in Eq. (2.11) is independent of (x_o, y_o). The 3D impulse response of circular tomosynthesis looks like the surface of a double cone, as is shown in Fig. 2.5. The tomographic angle determines the shape of the impulse response. In the limit of the projection angle $\theta \rightarrow 0$, the radius of the ring blur for off-plane objects goes to 0 and the object is reconstructed in its original (x_o, y_o) location for any z_b. The 3D impulse response goes to a line, as is consistent with projection radiography.

One of the positive attributes of circular tomosynthesis is its great imaging flexibility. While CT has strict requirements for the path of the x-ray tube and detector during image acquisition, i.e., in a plane parallel to the conventional imaging plane, tomosynthesis is able to operate over a range of motions by adjusting the tomographic angle. This can be seen by examining the 3D impulse response. As the tomographic angle decreases, the opening of the cone in the impulse response becomes smaller. The appearance of off-plane objects in the reconstructed image are modified by reducing the blurring radius. For an infinite number of views, the larger tomographic angles provide better blurring of these off-plane objects. For a limited number of views, there is a trade-off between the tomographic angle and the number of views required to adequately reconstruct an object, since the discrete nature of the impulse

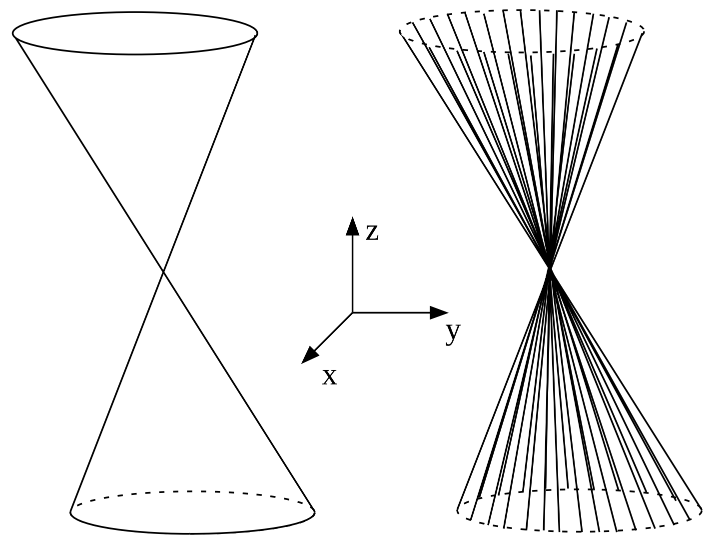

Figure 2.5: Circular tomosynthesis impulse response for an infinite number of views (left) and a finite number of views (right).

response becomes evident sooner for a larger cone angle.

An extended 3D object is affected by circular tomosynthesis in the same way as the point object described above. The extended object can be analyzed by treating it as consisting of a number of small voxels, each which act like a point object. The portion of the object lying on the imaging plane is faithfully reconstructed while the portion off the plane is blurred as above. Alternatively, one may view this by convolving the 3D impulse response (Fig. 2.5) with the 3D object.

Frequency Domain Analysis

Alternatively, one can take a frequency space approach in order to describe circular tomosynthesis, as was done above for CT. In CT, each of the 1D projections samples the line in 2D Fourier space through the origin and orthogonal to the direction of projection. In volumetric tomography (with parallel rays), each of the 2D projections samples the plane in 3D Fourier space through the origin and orthogonal to the direction of projection. As shown in Fig. 2.6, the volume in Fourier space sampled by all of the projections in circular tomosynthesis is the region outside the cone defined by $\pi/2 - \theta$ for a tomographic angle 2θ.

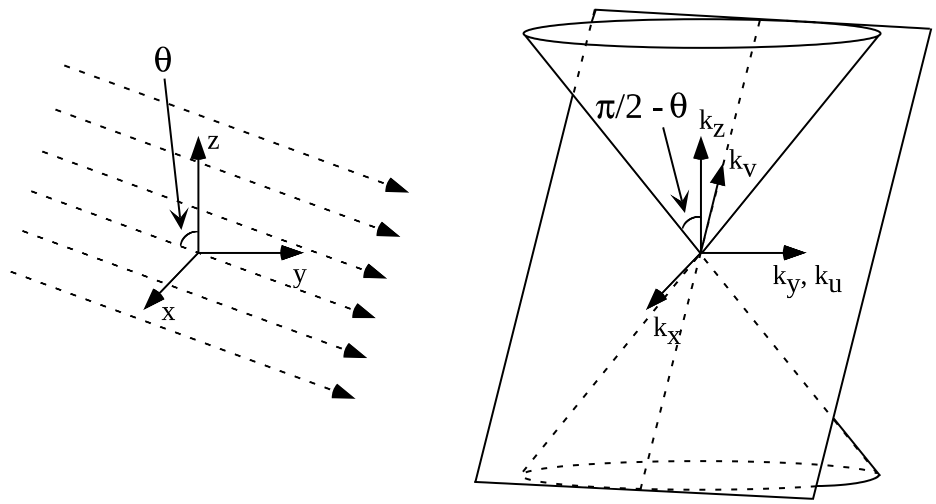

Figure 2.6: Frequency space coverage is a plane for a single projection (left), and the area outside a cone for circular tomosynthesis with many projections.

A perfect reconstruction is not possible in circular tomosynthesis, because there are frequencies which are not sampled, i.e., the cone in Fig. 2.6. As the tomographic angle increases, the region of Fourier space which is not sampled shrinks, and the reconstructions improve. In the limit of $\theta \to \pi/2$, the unsampled cone disappears and all of Fourier space is covered. This is as expected since $\theta = \pi/2$ is the VCT geometry. In the limit of $\theta \to 0$, only the $k_z = 0$ plane is sampled. This yields no resolution in the z direction, as expected since this is the projection radiography geometry.

As in CT, the sampling of Fourier space by circular tomosynthesis is not uniform. Correction for this uneven sampling density improves the reconstructed images in CT. In tomosynthesis, as in CT, filtering can be used to manipulate the effect of sampling density and alter the reconstruction of off-plane objects without corrupting in-plane objects. This is the subject of Ch. 6.

2.3 Digital X-ray Detectors

The re-emergence of interest in tomosynthesis is largely dependent on the development of digital x-ray detectors because they allow for far greater ease than conventional detectors in multiple image acquisition and digital processing. While a detailed description is beyond the scope of this thesis (see e.g. [10–12]), an overview of digital flat-panel detectors is beneficial in order to understand the underlying technology which enables volumetric tomographic imaging (in addition to ultimately replacing analog systems and ushering radiography into the digital age).

Conventional radiography has been performed using film-screen systems. These systems typically consist of a film layer and one or two fluorescent intensifying screens. When absorbed in the fluorescent material, x-rays excite electrons to the conduction band. Relaxation of the electrons to the valence band emits light photons, which expose the film. Alternatively, the x-ray can expose the film directly, but this process is much less efficient. Film-screen systems, however, have many drawbacks. A digitization step is required for post-processing techniques such as digital subtraction and tomosynthesis, and this detector system has a poor dynamic range [13, 14]. Imaging techniques which require the acquisition of images in a short amount of time require rapid film changers [15]. In addition, physical storage of x-ray films is a significant problem (although it should be noted that digital detectors present an electronic storage problem).

Conventional fluoroscopy has been performed using image intensifiers. This imaging device consists of an input fluorescent layer and photocathode, electrostatic lens, anode, and output fluorescent screen. The input fluorescent layer converts the x-rays into light photons, which are then converted to electrons by the photocathode. As the electrons are accelerated towards the anode by a high potential difference, the electrostatic lens focuses them. These electrons are then converted back to photons by the smaller output screen. The combination of geometrical reduction and electron acceleration results in a large gain in brightness for the image intensifier, which allows the device to be used in the lower dose conditions of fluoroscopy. Imaging intensifiers, however, also have many drawbacks. The output images exhibit a large amount of distortion, due to both the curvature of the input fluorescent layer and the deflection of the electrons by the earth's magnetic field [4, 16, 17]. Moreover, the latter effect is dependent on the position of the image intensifier [18], which changes in a system undergoing motion (i.e., a clinical tomosynthesis system). As in film-screen systems, a digitization step is required for post-processing techniques. For systems requiring detector motion, the large size and weight of an image intensifier may complicate mechanical engineering requirements.

To replace film-screen systems and image intensifiers, medical imaging companies have been developing digital, active matrix, flat-panel x-ray detectors, which can be divided into two main groups: direct detectors, and indirect detectors. Direct detectors directly convert x-rays to electrons for signal detection, while indirect detectors include an intermediate step which converts x-rays to light photons (which are then measured). The electronic image is stored in each pixel until the panel is read out, when a transistor acts as a switch to send the pixel charge to an Analog-to-Digital Converter (ADC), and from there to a computer. Typical pixel sizes are 40 - 100 μm for a 20 x 20 cm^2 mammographic panel, and 200 μm for a 40 x 40 cm^2 chest panel [12, 14, 19, 20]. Prototype systems are capable of fluoroscopic readout rates of 30 frames per second for a 20 x 20 cm^2 panel with 200 μm pixels (GE Medical Systems, Milwaukee, WI). It should be noted that while this research does not involve images collected in a fluoroscopic mode, the digital flat-panel detector used in the volumetric tomography system is capable of this type of imaging.

Direct detectors, as in Fig. 2.7, allow high spatial resolution because the x-ray signal is carried by electrons, which electric fields can guide to limit blurring, from the x-ray absorption point to the detector pixel [10, 21]. The x-ray is absorbed directly by the photoconductor, where it generates electron-hole pairs. The electrons (and secondary electrons) are driven by the electric field to the surface, where the charge is transferred to a storage capacitor (on a readout panel). When the panel is read out, a transistor acts as a switch to send the pixel charge to a computer via an ADC.

In contrast, indirect detectors, as in Fig. 2.8, use light photons to carry the x-ray signal. A phosphor layer, such as CsI, converts the x-rays to light photons as in

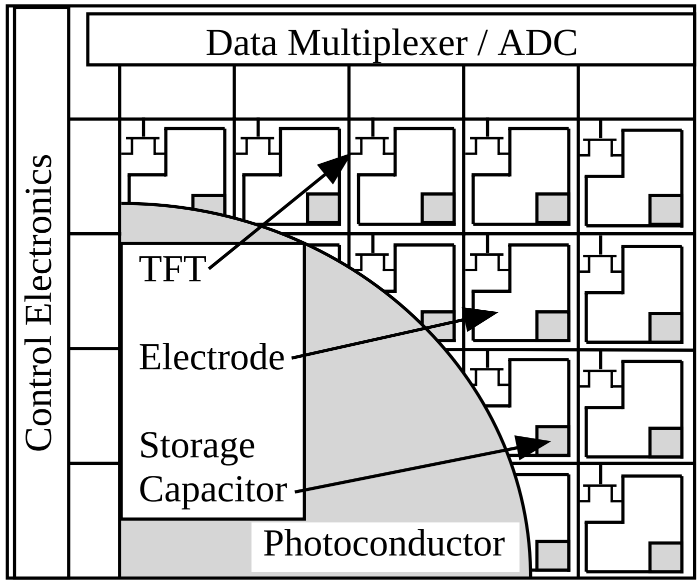

Figure 2.7: Schematic of a direct digital flat-panel detector.

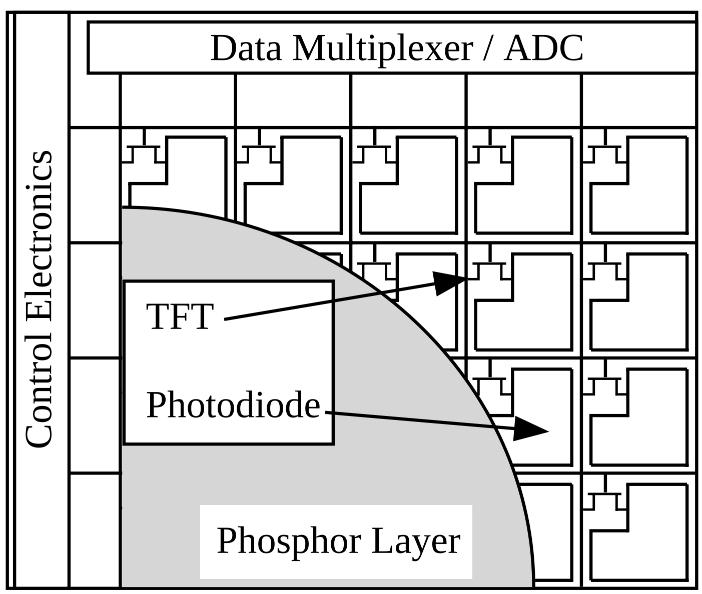

Figure 2.8: Schematic of an indirect digital flat-panel detector.

conventional detectors. The photons travel to the detector surface, where a photodiode on each pixel converts the light to electronic charge. There is less control of the spreading of the signal in indirect detectors, which can lead to lower spatial resolution capabilities. The amount of diffusion that the photons undergo, however, can be reduced by using phosphor layers grown in column-like structures [14]. Currently, however, indirect detectors are more technically feasible [10].

2.4 Current Tomosynthesis Research

With the technological advances in digital x-ray detectors, interest in tomosynthesis has been revived. A number of research groups in the last ten years have been investigating the application of tomosynthesis to medical imaging.

Niklason et al. [22] and Webber et al. [23] have studied the application of tomosynthesis to mammographic imaging, where tomosynthesis can improve visualization of suspect regions by blurring overlying objects. Other potential diagnostic imaging application being studied include dental imaging (Webber et al. [24]), angiography (Stiel et al. [25]), and lung imaging (Dobbins et al. [26]). Additionally, Zwicker and Atari [27] and Messaris et al. [28] have examined the application to radiotherapy, where tomosynthesis can aid in tumor localization.

In addition to the development of tomosynthesis units, other investigators have developed algorithms for improved tomosynthesis reconstructions. Kolitsi et al. [29] have reduced image reconstruction time by using transformations on groups of pixels. A wavelet-based approach to improve visualization in sparse objects has been developed by Badea et al. [30]. Lauritsch and Härer [31] have investigated the development of filters for filtered backprojection reconstruction.

The research described in this document contains many of these same themes, namely the development of a system for tomosynthesis, its application to clinically relevant imaging tasks, and algorithm development to improve the quality of reconstructed images. This work expands the study of the basic principles of tomosynthesis, and offers improved reconstructed images for potential clinical applications. The description of this work is the topic of the remaining chapters.

Chapter 3

Volumetric Tomography System

In order to study the basic principles of tomosynthesis, we have developed a test-bed volumetric tomography system. This chapter covers the motivation for, and the development of, this system. This system, which is built around a prototype digital flat-panel x-ray detector, can also be used to study digital radiography and volumetric computed tomography.

3.1 System Design

There are two possibilities in constructing a volumetric tomography system: either the x-ray tube and detector must both move about a stationary object, or the object must move while the tube and detector are fixed in position. The first option is more clinically relevant, but requires a more sophisticated mechanical engineering approach. We chose the latter approach, as is shown in Fig. 3.1. This restricts the use of the system to imaging phantoms and tissue samples, rather than patients, but still satisfies our main need, namely a system to study the basic principles of tomosynthesis.

Because we are interested in studying the basic fundamentals of tomosynthesis, the optimal system must have as flexible a geometry as possible in order to easily change the imaging parameters. For instance, in order to study the impact of the tomographic angle, we would like to be able to choose any angle in the range $[0, \pi]$

without altering the location of the object. The use of a rotational positioning stage to move the object in between exposures (while the x-ray tube and detector are locked in place) allows the same system to be used for circular tomosynthesis, VCT, and radiographic imaging. Except in the case of VCT, the positioning stage must be approximately transparent to x-rays since the system geometry requires that the x-rays pass through the stage prior to their detection.

One approach to developing a tomosynthesis unit is to rely on very precise mechanical alignment, followed by additional software correction, as is normally done with CT scanners. The system geometry must be very accurate in order to reconstruct high quality images. Misalignments resulting in signal mismapping of even a fraction of a pixel away from an object's position will result in blurring of the image. Intuitively, one would expect the alignment tolerance to possibly be more stringent than in CT due to the higher in-plane resolution. The task of precise alignment becomes difficult given current detectors with pixel sizes of 200 μm or less [12,14,19,20]. In addition, even if the system geometry is very well known in one position, it could change during the image acquisition, due to mechanical imperfections or sagging of the gantry [32–34]. Without correction, this geometrical distortion will limit the ability to produce high quality image reconstructions.

An alternative system design is to lessen the role of precise mechanical alignment, and augment the role of software correction techniques. For example, the tube and detector can be mounted on a conventional low-cost chassis, such as a C-arm. A software technique can be relied on to correct for the misalignments, maintaining both the imaging flexibility of the gantry and the low cost of the system. In order to do this, the system geometry must be measured precisely, which can be done with the x-ray system itself, and a correction technique must be developed to handle the system imperfections.

Using this design philosophy, we have developed a phantom-based system. The x-ray tube and detector are locked in place, while the object being imaged is rotated between x-ray exposures. In this chapter we present the components of the volumetric tomography system, and describe its construction. In Ch. 4, we present an analysis of the system sensitivity to geometrical misalignments, and discuss in Ch. 5 the software

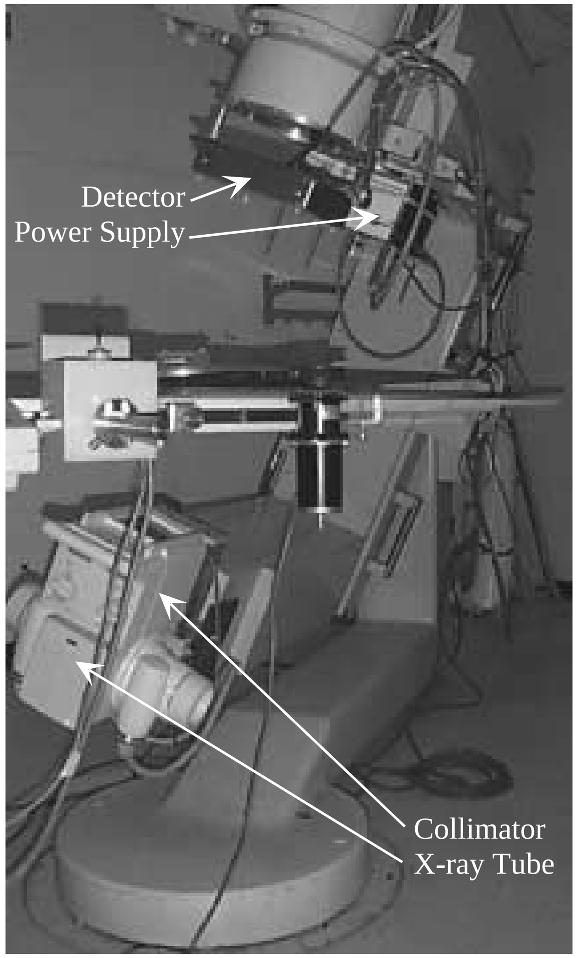

Figure 3.1: Volumetric tomographic imaging system, shown in tomosynthesis mode, with the gantry rotated to 25° (50° tomographic angle).

technique we have developed to correct for these errors.

3.2 Experimental System

3.2.1 Overview

Figure 3.1 shows the volumetric tomography system that we have developed. It is based on an x-ray tube and a digital flat-panel detector mounted on a L-U chassis (GE Medical Systems, Milwaukee, WI). The tomographic angle, source to detector distance (SD), and source to object distance (SO) are selected by adjusting the gantry, and locking it in place. The x-ray transparent positioning stage is rotated through 360° in discrete steps between x-ray exposures. Tomographic angles from 0 to π are possible, with the tomographic angle defined as twice the angle of the central ray of the x-ray beam relative to the axis of rotation. An angle of 0 yields A-P radiographic data, π yields volumetric CT data, and an angle in between yields circular tomosynthesis data.

3.2.2 Gantry

The tomography system is built on a L-U chassis, which was originally designed for angiographic applications. This system was very versatile, using an image intensifier coupled to a television camera, and a rapid film-changer. The L-U system is a precursor of the modern angiographic positioners, and allows for a great deal of flexibility in the imaging geometry. The U-arm can be rotated through a 180° range, and both the x-ray tube and detector can be moved vertically on their mountings. This allows the acquisition of images in the range from anterior-posterior (A-P) to lateral on a supine patient, with adjustable magnification. When coupled with a rotational positioning stage, Sec. 3.2.4, this allows the acquisition of images of phantoms in imaging modalities from radiography to circular tomosynthesis to VCT. Included with the L-U chassis is a patient table with 3D freedom of movement.

The gantry was modified with the addition of a prototype digital flat-panel detector, Sec. 3.2.3, and a compatible x-ray tube. The detector was mounted to the bottom of the image intensifier, and its power supply was mounted in the place of the film-changer. In addition, the x-ray tube and collimator, and their corresponding control and power electronics, were updated to be compatible with the new detector. The positioning stage was mounted to this table, which allowed proper placement of the phantom in the field of view.

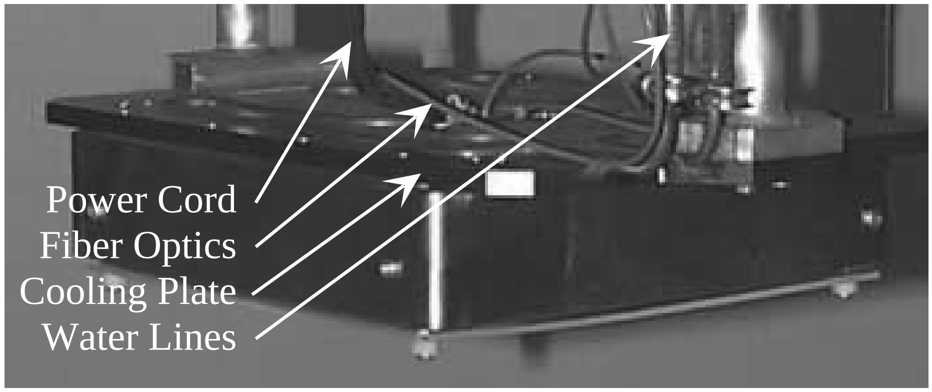

Figure 3.2: Prototype flat-panel x-ray detector from GE Medical Systems.

3.2.3 Detector

The detector, Fig. 3.2, is an indirect flat-panel x-ray detector, as described in Sec. 2.3. This prototype of the Revolution detector from GE Medical Systems is a 1024 by 1024 photodiode array, with a 200 μm pixel pitch, covered by a CsI:Tl scintillator layer. The panel can be operated either in radiographic of fluoroscopic modes, with approximately 30 ms readout times in the latter. The 12-bit pixel values are sent via fiber optic cables to an acquisition card capable of storing 128 frames in memory before writing them to a disk. The detector is water-cooled using a heat sink and an external copper coil.

Imperfections in the detector and electronics result in serious imaging artifacts in uncorrected images. Figure 3.3 shows the raw image of a 3/8" thick piece of lucite, which should be nearly uniform other than due to the angular distribution of x-ray output and quantum noise. This image demonstrates the typical imaging artifacts present for this type of detector: bad pixels, bad lines, non-uniform readout gain, dark current, and regions of non-uniform x-ray conversion. The column-like structure in Fig. 3.3 is due to the unequal gains in the readout electronics, and the difference between the top and bottom halves of the detector arise because the panel signals are sent out from the middle to top and middle to bottom, simultaneously, in order to decrease readout time.

A number of steps are taken in order to correct for these image artifacts. Bad pixels (including bad lines) are identified by thresholding the raw data, and replaced with a median value of the neighboring pixels. The gain (including the readout electronics and the x-ray conversion) and the dark current are measured by the collection of two additional images: a flat field, i.e. no object present, and a dark field, i.e. x-ray beam blocked. Using these two additional images, the true (although noisy) image intensity T can be recovered for each pixel i, j from the measured pixel intensity I according to:

$$T_{i,j} = (I_{i,j} - D_{i,j}) \frac{\overline{F_{i,j} - D_{i,j}}}{F_{i,j} - D_{i,j}}, \tag{3.1}$$

where D is the measured dark current and F is the measured flat field. The overbar in Eq. (3.1) represents the average over the entire image. Only one dark field and one flat field image are need to correct an entire dataset. Figure 3.4 shows the result of the correction technique (Eq. (3.1)) applied to the image of the 3/8" thick piece of lucite. Equation (3.1) is based on a linear signal model. Alternatively, a non-linear correction scheme can be used. We have applied a second-order model, based on a dark measurement and four flat fields at different intensities, for some applications.

3.2.4 Positioning Stage

Phantoms are placed on a custom, computer-controlled, rotational positioning stage (Tapemation, Scotts Valley, CA). The positioning stage, shown in Fig. 3.5, holds objects on an x-ray transparent platform mounted to a high-precision bearing (Kaydon, Muskegon, Michigan). The large diameter of the bearing opening (18 inches) allows images to be collected with tomographic angles up to 110° for typical imaging conditions with the current detector size, without the bearing structure blocking the x-ray beam. The bearing is coupled to a step motor via a belt, which runs in a machined slot on the exterior of the bearing. This approach was taken in order to simplify the stage design without dealing with the backlash concerns of a gear-driven system. In order to produce fine enough rotations of the stage, a 10:1 gear reducer (Bayside, Port Washington, NY) is used between the motor and positioning stage bearing. The step motor is controlled by a PC, via an indexer/controller (Compumotor, Rohnert

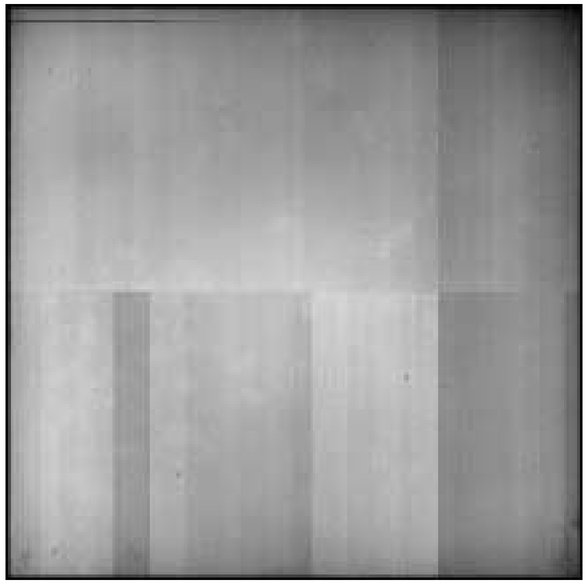

Figure 3.3: Uncorrected image of a uniform 3/8" thick piece of lucite.

Figure 3.4: Corrected image of a uniform 3/8" thick piece of lucite. The window width has been narrowed relative to Fig. 3.3.

Park, CA).

3.2.5 System Operation

Modifications were made to the system in order to allow automatic data acquisition, which is controlled by a PC via the indexer/controller. In addition to communicating with the PC, the indexer/controller communicates with the x-ray generator console via custom electronics in order to initiate an x-ray exposure. In order to collect volumetric tomography data, the gantry is first set to the desired tomographic angle. The positioning stage and phantom are centered in the x-ray field of view, and the desired number of views is given to the indexer/controller. The system automatically acquires the data, by rotating the stage between each exposure and collecting projections.

An example of the type of projection images which can be obtained with this system is shown in Fig. 3.6. These images show the 20 view projection data for a desiccated dog lung phantom, taken with a 40° tomographic angle. The automation of the image acquisition process makes the collection of larger datasets more feasible, which would otherwise be quite cumbersome.

3.3 Conclusions

Combination of the components described above yields a volumetric tomography system which produces multiple radiographic projections. These tomosynthesis projection images can be used to reconstruct volumetric information for an imaging phantom. This is made possible because each image is taken with the x-ray tube and detector in a different position relative to the phantom, providing information for the 3D spatial extent of the object. As is described in Ch. 4, this data can be used to generate high quality reconstructed images, even though the system is not precisely aligned.

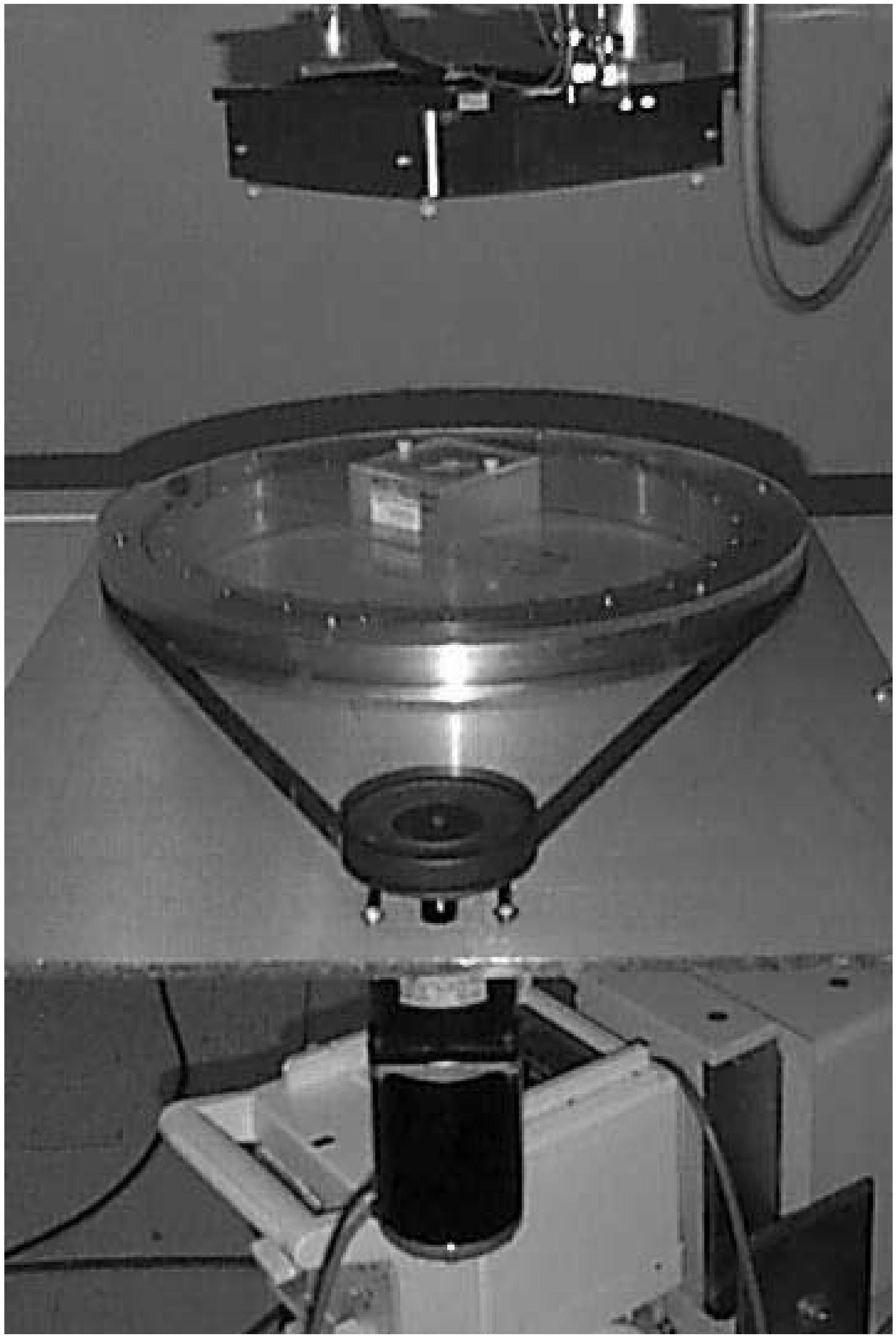

Figure 3.5: Computer-controlled rotational positioning stage for phantom imaging (ACR Mammographic phantom shown here).

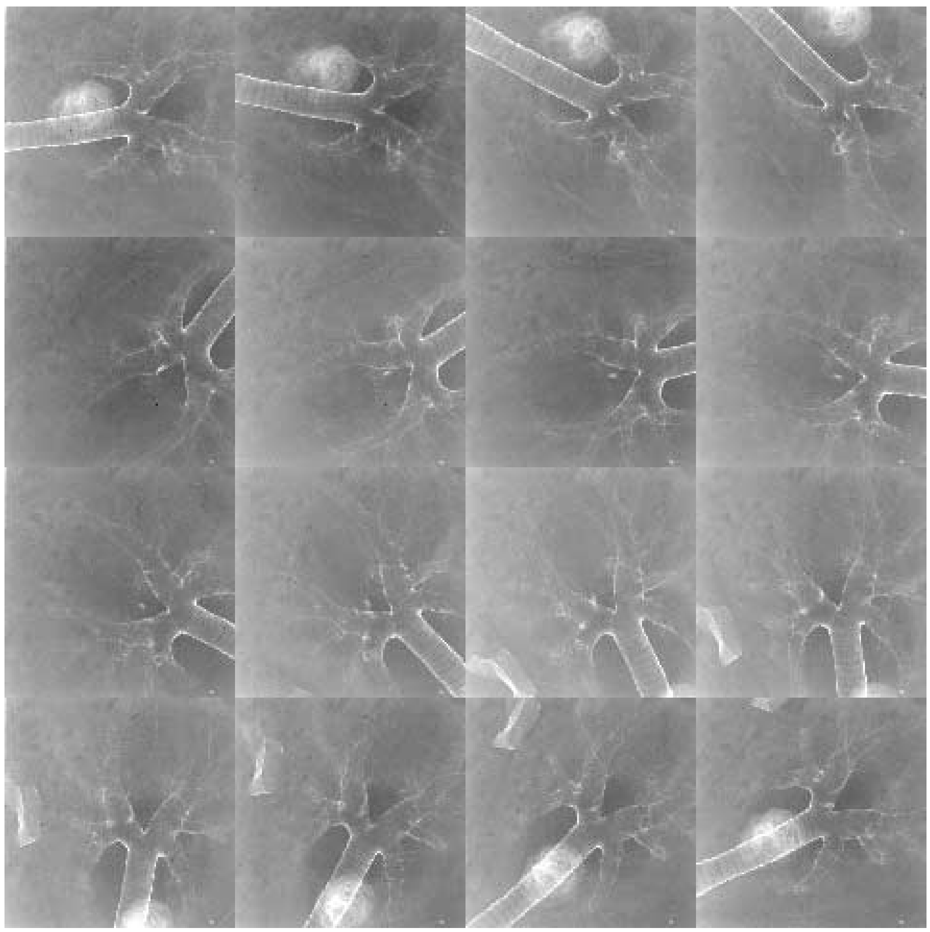

Figure 3.6: Projection data for a lung phantom. Twenty views were collected with a 40° tomographic angle.

Chapter 4

Alignment Sensitivity

4.1 Introduction

As described in Ch. 3, the design philosophy does not dictate precise mechanical alignment of the volumetric tomography system. Therefore, it can be expected that the system will have misalignments. It is useful to examine the effects of misalignments in order to gauge which ones are critical, and what artifacts are induced by their presence. In this chapter, we present a demonstration of the sensitivity of reconstructed images to geometrical misalignment. Computer simulations are used to verify the analytical work. The goal of Ch. 5 is to correct for these errors, using a software technique we have developed.

The aim of this chapter is not to fully characterize the system's sensitivity, but rather to depict the large effect of even relatively small misalignments on reconstructed images. Ultimately, it may be useful to more closely delineate the effect of each misalignment, and to examine additional geometrical parameters in order to fully understand the effect on image quality. A complete study of all these sensitivites, however, is beyond the scope of this dissertation.

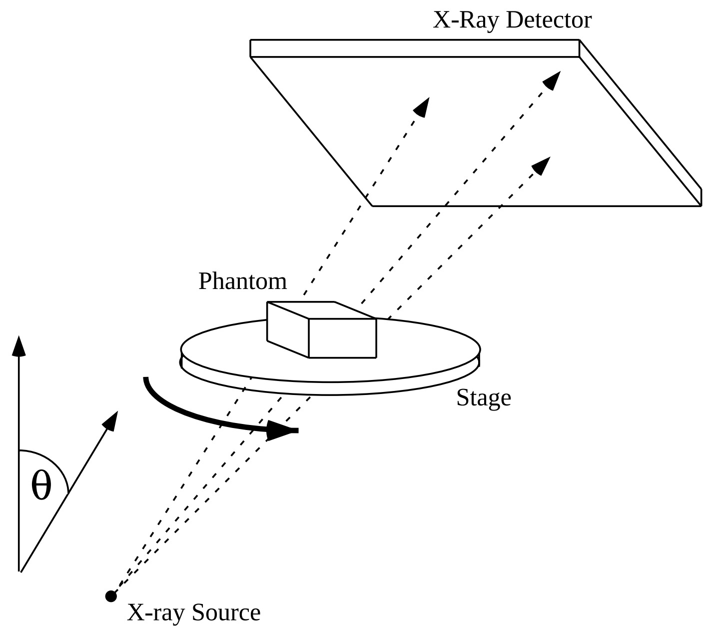

Figure 4.1: Volumetric tomography system incorporating a digital flat-panel detector. In circular tomosynthesis mode, the x-ray tube and detector are rotated from vertical by θ (half the tomographic angle), and locked in place. The imaging phantom is placed on an x-ray transparent positioning stage, and rotated between each exposure through 360°.

2θ	tomographic angle
ϕ	angle of rotation of positioning stage
z_t	x-ray tube height
z_d	detector height
$\overrightarrow{x_o} \equiv (x_o, y_o, z_o)^T$	initial object location
$\overrightarrow{x_p} \equiv (x_p, y_p, z_p)^T$	location of projection data
$\overrightarrow{u} \equiv (u_x, u_y)^T$	$(x_p, y_p, z_p)^T$ in detector coordinate system
$\overrightarrow{x_b} \equiv (x_b, y_b, z_b)^T$	location of backprojected object
$\overrightarrow{x_c} \equiv (x_c, y_c, z_c)^T$	approximate center of backprojected object

Table 4.1: Definition of variables used to describe x-ray projection and simple back-projection reconstruction.

4.2 Sensitivity Analysis & Experiments

A demonstration of the sensitivity of image quality as a function of geometrical misalignments can be beneficial in determining which geometrical parameters are most crucial in an imaging system. Consider a C-arm system with a rotational positioning stage, as depicted in Fig. 4.1. A list of parameters for this setup are given in Tbl. 4.1. The relative motion is equivalent to a tube and detector which rotate about a fixed phantom or patient. Note that in comparison with conventional circular tomography [4], the equivalent motion of this system also contains a rotation of the detector (about the normal to its surface) with respect to the object. Analyses were performed for this system for (1) an error in the tomographic angle, (2) a rotation of the detector on its mounting, (3) a translation of the detector on its mounting, and (4) a tilt of the axis of rotation of the positioning stage relative to vertical. In each case, the analysis assumed that all parameters were precisely known except the one being studied. The sensitivity to the parameter in question is explored using values comparable to the expected alignment errors: 4° in tomographic (this is a larger error than anticipated, but is used to demonstrate the relatively benign nature of this single misalignment), 3° detector rotation, 1 mm detector translation, and a 1° tilt of the positioning stage axis. Because the relative motion of this system is not exactly the same as that in a circular tomography system in which the tube and detector move about a stationary patient, some of our results may not be directly applicable to those systems. This is discussed in Sec. 4.3.

Simulations were performed in order to validate this analysis. A projection simulator (which we developed based on the analysis of circular tomosynthesis in Ch. 2) was used to generate noiseless projections of small spherical objects. Datasets with 100 views were used to show the effect of geometrical misalignments in the limit of many views. The detector was assumed to have a 200 μm pixel size, and the projection data were backprojected onto a 100 μm pixel grid. The source to object distance (SO) was 100 cm, and the source to detector distance (SD) was 125 cm. The system was simulated with a tomographic angle of 40°, unless otherwise noted.

4.2.1 Tomographic Angle

Consider the case in which the system is perfectly aligned, except that the tomographic angle is not known exactly. With θ denoting the angle of the central ray of the x-ray beam relative to the axis of rotation (see Fig. 4.1), the tomographic angle is 2θ. At tomographic angle 2θ, the tube and detector are centered at $(z_t \sin\theta, 0, z_t \cos\theta)^T$ and $(z_d \sin\theta, 0, z_d \cos\theta)^T$, respectively. For a point-object located at $(x_o, y_o, z_o)^T$ and for a positioning stage angle of ϕ, the ray from the source and passing through this object intersects the detector at:

$$\overrightarrow{x_p} = \frac{\begin{bmatrix} (x_o\cos\phi - y_o\sin\phi)(z_t\cos^2\theta - z_d) - z_t\sin\theta(z_o\cos\theta - z_d) \\ (x_o\sin\phi + y_o\cos\phi)(z_t - z_d) \\ -(x_o\cos\phi - y_o\sin\phi)z_t\cos\theta\sin\theta - z_d(z_o - z_t\cos\theta) + z_o z_t\sin^2\theta \end{bmatrix}}{z_t - (x_o\cos\phi - y_o\sin\phi)\sin\theta - z_o\cos\theta}. \quad (4.1)$$

In terms of the natural coordinate system of the detector (i.e., a 2D coordinate system on the surface of the detector with the origin at the detector center) the projection location can be written:

$$\overrightarrow{u} = \frac{\begin{bmatrix} (z_t - z_d)((x_o\cos\phi - y_o\sin\phi)\cos\theta - z_o\sin\theta) \\ (z_t - z_d)(x_o\sin\phi + y_o\cos\phi) \end{bmatrix}}{z_t - (x_o\cos\phi - y_o\sin\phi)\sin\theta - z_o\cos\theta}. \quad (4.2)$$

Suppose the tomographic angle is not known exactly, and is assumed to be $2\tilde{\theta} = 2(\theta + \delta\theta)$, where $\delta\theta$ is a small angle. The backprojection of the signal at detector location $\overrightarrow{u}$ using $\tilde{\theta} = \theta + \delta\theta$ intersects the plane at height $z = z_b$ at:

$$\overrightarrow{x_b} = \begin{bmatrix} \frac{\{u_x[z_t - z_b\cos(\theta+\delta\theta)] + z_b(z_t - z_d)\sin(\theta+\delta\theta)\}\cos\phi + u_y[z_t\cos(\theta+\delta\theta) - z_b]\sin\phi}{(z_t - z_d)\cos(\theta+\delta\theta) + u_x\sin(\theta+\delta\theta)} \\ \frac{\{-u_x[z_t - z_b\cos(\theta+\delta\theta)] - z_b(z_t - z_d)\sin(\theta+\delta\theta)\}\sin\phi + u_y[z_t\cos(\theta+\delta\theta) - z_b]\cos\phi}{(z_t - z_d)\cos(\theta+\delta\theta) + u_x\sin(\theta+\delta\theta)} \\ z_b \end{bmatrix}. \quad (4.3)$$

When the projection data from Eq. (4.2) is substituted into Eq. (4.3), the data no longer focuses at a point for $z_b = z_o$. That is, for $z_b = z_o$, $\overrightarrow{x_b}$ in Eq. (4.3) is not constant as a function of ϕ. The image at $z = z_o$ is now blurred for objects which are actually on the plane and which should be in focus.

This, however, is not surprising. Intuitively, we expect an error in θ to introduce an error in the slice thickness and slice location. We can define the slice location at which a point-object focuses as the value of z for which the transverse extent of the impulse response is narrowest. This was computed by minimizing the diameter of the transverse response as a function of reconstruction height. This was done analytically by approximating Eq. (4.3) with a Taylor's series expansion, keeping terms up to first order in $\delta\theta$. The derivative of this approximation can then be taken with respect to ϕ, calculating z_b for which the derivative is equal to zero. Further approximation can be made by discarding small terms. With this definition for the slice location, for small $\delta\theta$ and objects near the axis of rotation, an object at position $\overrightarrow{x_o}$ will appear to focus at:

$$\overrightarrow{x_c} = \begin{bmatrix} x_o\left(\frac{z_o\left(1-\frac{\delta\theta z_t\cos^2\theta}{(z_t\cos\theta-z_o)\sin\theta+\delta\theta z_t}\right)-z_t\cos\theta}{z_o-z_t\cos\theta}\right) \\ y_o\left(\frac{z_o\left(1-\frac{\delta\theta z_t\cos^2\theta}{(z_t\cos\theta-z_o)\sin\theta+\delta\theta z_t}\right)-z_t\cos\theta}{z_o-z_t\cos\theta}\right) \\ z_o\left(1-\frac{\delta\theta z_t\cos^2\theta}{(z_t\cos\theta-z_o)\sin\theta+\delta\theta z_t}\right) \end{bmatrix}. \tag{4.4}$$

This focusing is perfect (although not on the plane on which the object lies) for the case of parallel x-rays, i.e., $z_t \rightarrow \infty$.

For this simple case of an error in the tomographic angle, the artifacts caused by system misalignment are relatively benign in that they merely shift and stretch the image. The object still appears focused, just not in its true location. In addition, the image is slightly distorted. The image plane shift is stationary on each transverse plane, since z_c is independent of x_o and y_o in Eq. (4.4). These effects were verified by simulations. Figure 4.2 shows that for a 4° error in the tomographic angle $2\theta = 40°$, i.e. projection angle $\theta = 20°$ and backprojection angle $\tilde{\theta} = 22°$, small spherical objects which lie at $z_o = 2.0$ cm focus at $z \approx 1.82$ cm. This is in agreement with the prediction of Eq. (4.4). The amount of in-plane stretching seen in the simulations and predicted analytically (Eq. (4.3) or (4.4)) is summarized in Tbl. 4.2, which shows shifts in the in-plane reconstruction location of approximately 0.02 cm for objects within $\sqrt{2}$ cm of the origin. This stretching scales linearly with distance from the center of the imaging volume. As Tbl. 4.2 demonstrates, the main power of the simplified Eq. (4.4) is to estimate the slice location rather than the amount of stretching in the image. The simplified expression does an excellent job of predicting the location of the plane on which the object focuses, but not the location of the object in this plane.

4.2.2 Detector Rotation

Consider the case in which the detector is rotated by an angle $\delta\eta$ about its center (and about the central ray), but is still normal to the central ray. The projection of a point-object located at $(x_o, y_o, z_o)^T$ at stage rotation angle ϕ can again be described by Eq. (4.1). In terms of detector coordinates, the projection is:

$$\overrightarrow{u} = \frac{\begin{bmatrix} (z_t - z_d)\{[x_o \sin\phi + y_o \cos\phi] \sin\delta\eta - [z_o \sin\theta - (x_o \cos\phi - y_o \sin\phi)\cos\theta] \cos\delta\eta\} \\ (z_t - z_d)\{[x_o \sin\phi + y_o \cos\phi] \cos\delta\eta + [z_o \sin\theta - (x_o \cos\phi - y_o \sin\phi)\cos\theta] \sin\delta\eta\} \end{bmatrix}}{z_t - (x_o \cos\phi - y_o \sin\phi)\sin\theta - z_o \cos\theta}. \tag{4.5}$$

For reconstruction of a plane at height $z = z_b$ performed assuming perfect alignment, the backprojection of this ray intersects the plane at:

$$\overrightarrow{x_b} = \begin{bmatrix} \frac{\{u_x[z_t - z_b\cos\theta] + z_b(z_t - z_d)\sin\theta\}\cos\phi + u_y[z_t\cos\theta - z_b]\sin\phi}{(z_t - z_d)\cos\theta + u_x\sin\theta} \\ \frac{-\{u_x[z_t - z_b\cos\theta] + z_b(z_t - z_d)\sin\theta\}\sin\phi + u_y[z_t\cos\theta - z_b]\cos\phi}{(z_t - z_d)\cos\theta + u_x\sin\theta} \\ z_b \end{bmatrix}. \tag{4.6}$$

Because the projection data are rotated relative to data from a perfectly aligned detector, the tomosynthesis image is blurred. Simplifying this expression as above yields the center of the blurred reconstruction of the point-object falling at approximately:

$$\overrightarrow{x_c} = \begin{bmatrix} x_o\frac{z_b - z_t\cos\theta}{z_o - z_t\cos\theta} - \delta\eta y_o\frac{(z_b - z_t\cos\theta)[z_t(1+\cos^2\theta) - 2z_o\cos\theta]}{2(z_o - z_t\cos\theta)^2} \\ y_o\frac{z_b - z_t\cos\theta}{z_o - z_t\cos\theta} + \delta\eta x_o\frac{(z_b - z_t\cos\theta)[z_t(1+\cos^2\theta) - 2z_o\cos\theta]}{2(z_o - z_t\cos\theta)^2} \\ z_b \end{bmatrix}. \tag{4.7}$$

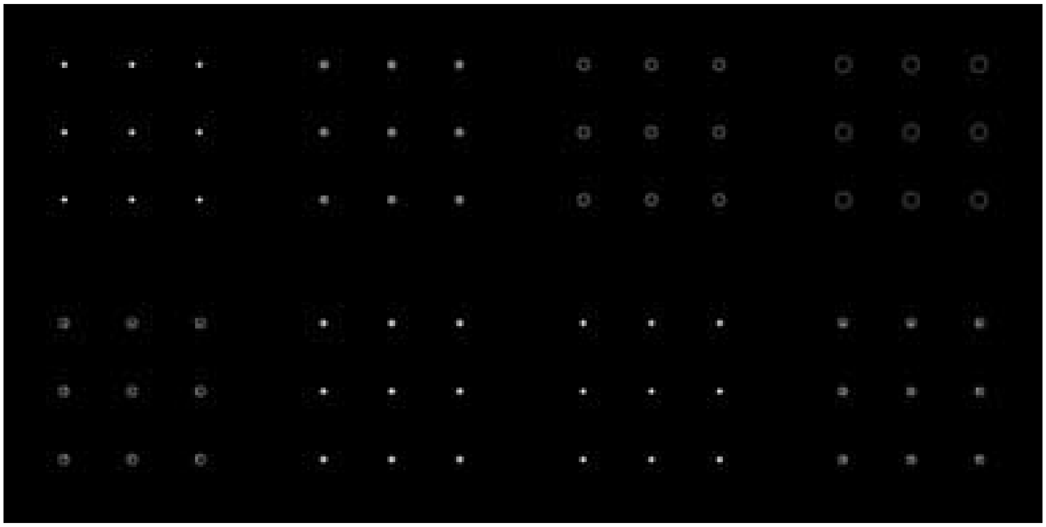

Figure 4.2: Reconstructed planes of simulated small spherical objects arranged in a grid (with 1 cm spacing) at $z_o = 2.00$ cm, using unfiltered backprojection with 100 views. The reconstruction planes are for $z = 2.00$, 1.91, 1.82, and 1.73 cm, from left to right. The top row shows images backprojected with tomographic angle 40° (error = 0°), and the bottom row shows backprojections using tomographic angle 44° (error = 4°).

(x,y) (cm)	Analytical Prediction (cm)	Simplified Prediction (cm)	Simulation Measurement (cm)
(0,0)	0.000	0.0000	0.000
(0,1)	0.018	0.0038	0.023
(1,1)	0.025	0.0054	0.032

Table 4.2: Displacement of the center of mass of reconstructed spherical objects due to a 4° error in tomographic angle for several object locations. The reconstruction plane is the one on which the objects best focus ($z = 1.82$ cm here). The analytical prediction (Eq. (4.3)) and the simplified prediction (Eq. (4.4)) are compared to the results of the simulation.

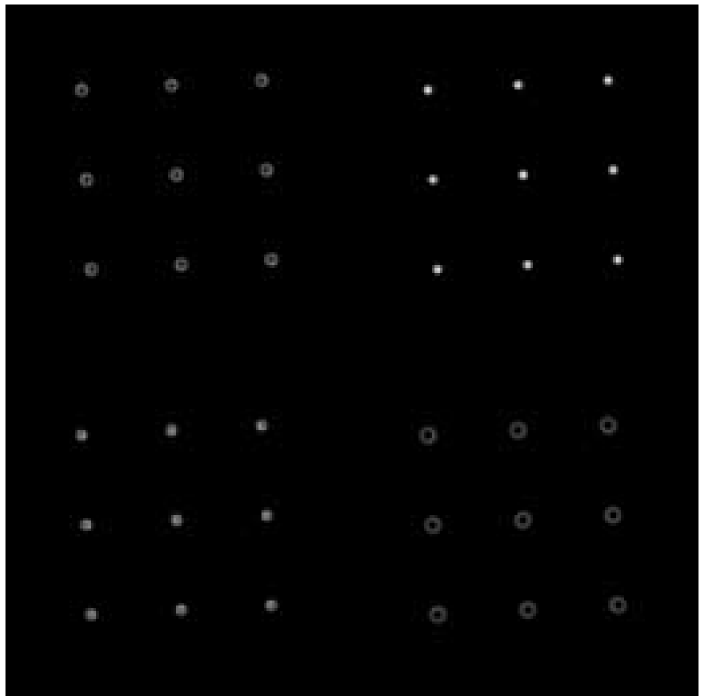

Figure 4.3: Reconstructed planes of simulated small spherical objects arranged in a grid (with 1 cm spacing) at $z_o = 2.00$ cm, using unfiltered backprojection with 100 views. The images were generated with a 3° detector rotation, and reconstructed assuming a 0° detector rotation. The reconstruction planes are for $z = 1.90$, 2.00, 2.10, and 2.20 cm, from left to right and top to bottom.

(x,y) (cm)	Analytical Prediction (cm)	Simplified Prediction (cm)	Simulation Measurement (cm)
(0,0)	0.002	0.000	0.000
(0,1)	0.105	0.105	0.101
(1,1)	0.150	0.149	0.144

Table 4.3: Displacement of the center of mass of reconstructed spherical objects due to a 3° error in detector rotation for several object locations. The reconstruction plane is the one on which the objects best focus ($z = 2.00$ cm here). The analytical prediction (Eq. (4.6)) and the simplified prediction (Eq. (4.7)) are compared to the results of the simulation.

Equations (4.6) and (4.7) predict that the object is most faithfully reconstructed (i.e., the least amount of blurring) on the plane where the object lies (i.e., $z_b = z_o$). Figure 4.3 shows an example of this for a 3° detector rotation. For this type of misalignment, focusing is imperfect. In addition to the objects being blurred, they are also rotated in the reconstructed image. Note that, although not intuitively expected, the blurring is relatively uniform on horizontal planes. Simulations verify the analytical results. The simulated objects at $z_o = 2.00$ cm focus best at $z = 2.00$ cm, which agrees with the analytical results. Table 4.3 shows that the reconstructed objects are shifted for this simulated example. Even for this small detector rotation, objects only 1 cm from the origin are shifted by more than 0.1 cm in the reconstruction plane.

4.2.3 Detector Shift

Now, consider the case in which the detector is shifted in the plane orthogonal to the central ray. The projection of a point-object located at $(x_o, y_o, z_o)^T$ with positioning stage angle ϕ is again described by Eq. (4.1). Now, however, because the detector is shifted by an amount $(x_d, y_d)^T$, the projection location in detector coordinates is:

$$\vec{u} = \frac{\begin{bmatrix} (z_t - z_d)[x_o \cos\phi - y_o \sin\phi) \cos\theta - z_o \sin\theta] - x_d \\ (z_t - z_d)(x_o \sin\phi + y_o \cos\phi) - y_d \end{bmatrix}}{z_t - (x_o \cos\phi - y_o \sin\phi) \sin\theta - z_o \cos\theta}. \tag{4.8}$$

If the reconstruction is performed assuming a perfectly aligned detector, for reconstruction at height $z = z_b$, the backprojected detector signal at detector location $\vec{u}$ intersects the plane according to Eq. (4.6). For this misalignment, the reconstructed image is blurred, with the center of the object falling at approximately:

$$\vec{x_c} = \begin{bmatrix} x_o \frac{z_b - z_t \cos\theta}{z_o - z_t \cos\theta} - x_d \frac{x_o (z_b - z_t \cos\theta)(z_o \cos\theta - z_t) \sin\theta}{(z_d - z_t)(z_o - z_t \cos\theta)^2} \\ y_o \frac{z_b - z_t \cos\theta}{z_o - z_t \cos\theta} - x_d \frac{y_o (z_b - z_t \cos\theta)(z_o \cos\theta - z_t) \sin\theta}{(z_d - z_t)(z_o - z_t \cos\theta)^2} \\ z_b \end{bmatrix}. \tag{4.9}$$

Simulations verify this analysis, and show that the effect of a shifted detector is quite severe. An example is shown in Fig. 4.4 for a detector shifted by 0.10 cm in both

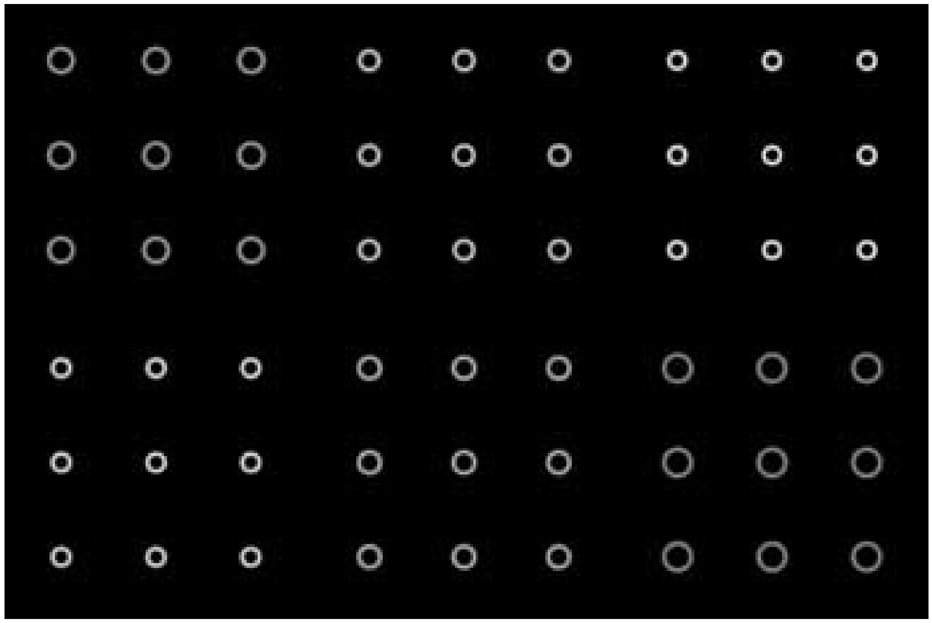

Figure 4.4: Reconstructed planes of simulated small spherical objects arranged in a grid (with 1 cm spacing) at $z_o = 2.00$ cm, using unfiltered backprojection with 100 views. The images were generated with a detector shifted by 0.10 cm in both directions, and reconstructed assuming no detector shift. The reconstruction planes are for $z = 2.00$, 2.11, 2.22, 2.33, 2.44 and 2.55 cm, from left to right and top to bottom.

directions in the plane containing the detector face. Even for this small shift, the image reconstruction plane with the least amount of blurring ($z \approx 2.22$ cm) shows blurring on the order of the size of the detector shift.

4.2.4 Axis of Rotation

The final case we consider is one in which the axis of rotation of the positioning stage is misaligned relative to vertical, i.e., the object rotates on the stage, but the axis of rotation is no longer parallel to the z-axis. Let $\delta\alpha$ define the angle between the stage axis and the z-axis, and let $\delta\beta$ be the angle between the projection of the axis onto a horizontal plane and the x-axis. The ray passing from the source through a small object located at $(x_o, y_o, z_o)^T$ with positioning stage angle ϕ intersects the detector at:

$$\overrightarrow{x_p} = \frac{\begin{bmatrix} x_s(z_t\cos^2\theta - z_d) - z_t\sin\theta(z_s\cos\theta - z_d) \\ y_s(z_t - z_d) \\ -x_s z_t\cos\theta\sin\theta - z_d(z_s - z_t\cos\theta) + z_s z_t\sin^2\theta \end{bmatrix}}{z_t - x_s\sin\theta - z_s\cos\theta}, \tag{4.10}$$

where

$$\overrightarrow{x_s} = \begin{bmatrix} -\sin\delta\beta z_o + \cos\delta\beta[x_o\cos(\delta\alpha - \phi) + y_o\sin(\delta\alpha - \phi)] \\ -x_o\sin(\delta\alpha - \phi) + y_o\cos(\delta\alpha - \phi) \\ \cos\delta\beta z_o + \sin\delta\beta[x_o\cos(\delta\alpha - \phi) + y_o\sin(\delta\alpha - \phi)] \end{bmatrix}. \tag{4.11}$$

In the detector coordinate system, the projection data lies at:

$$\overrightarrow{u} = \frac{\begin{bmatrix} (z_t - z_d)(x_s\cos\theta - z_s\sin\theta) \\ (z_t - z_d)y_s \end{bmatrix}}{z_t - x_s\sin\theta - z_s\cos\theta}. \tag{4.12}$$

The backprojection of this ray intersects the reconstruction plane for $z = z_b$ according to Eq. (4.6). For this case, the reconstructed images are blurred on all planes, with the center of the object's image falling at approximately:

$$\overrightarrow{x_c} = \begin{bmatrix} \frac{(x_o+\delta\alpha y_o)(z_b-z_t\cos\theta)}{z_o-z_t\cos\theta} + \frac{\delta\beta x_o z_t\sin\theta(z_b-z_t\cos\theta)}{(z_o-z_t\cos\theta)^2} \\ \frac{(y_o-\delta\alpha x_o)(z_b-z_t\cos\theta)}{z_o-z_t\cos\theta} + \frac{\delta\beta y_o z_t\sin\theta(z_b-z_t\cos\theta)}{(z_o-z_t\cos\theta)^2} \\ z_b \end{bmatrix}. \tag{4.13}$$

Simulations verify that misalignment of the stage's axis of rotation shifts the plane on which an object refocuses best. An example is shown in Fig. 4.5, in which small simulated spheres at $z_o = 2.00$ cm best focus at $z \approx 2.10$ cm for angular misalignments of 1° with respect to both the x-axis and the z-axis. Objects are distorted by this geometrical error, since the location of the object in the reconstructed plane depends on the (x, y) location of the object. This distortion is summarized in Tbl. 4.4.

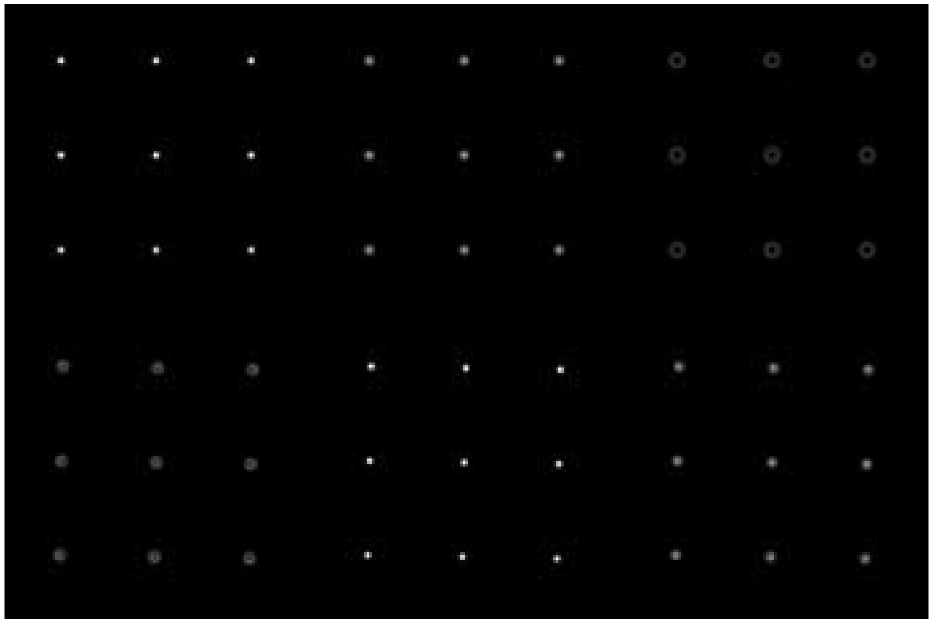

Figure 4.5: Reconstructed planes of simulated small spherical objects arranged in a grid (with 1 cm spacing) at $z_o = 2.00$ cm, using unfiltered backprojection with 100 views. The reconstruction planes are for $z = 2.00$, 2.10, and 2.20 cm, from left to right. The top row shows images backprojected with no error in the stage axis of rotation, and the bottom row shows backprojections of data collected with a stage axis misaligned with respect to the x-axis and z-axis by 1° each, and reconstructed assuming no misalignment.

(x,y) (cm)	Analytical Prediction (cm)	Simplified Prediction (cm)	Simulation Measurement (cm)
(0,0)	0.000	0.000	0.000
(0,1)	0.036	0.038	0.033
(1,1)	0.051	0.054	0.047

Table 4.4: Displacement of the center of mass of reconstructed spherical objects due to 1° error in stage axis angle with respect to both the x-axis and the z-axis, for several object locations. The reconstruction plane is the one on which the objects best focus ($z = 2.10$ cm here). The analytical prediction and the simplified prediction (Eq. (4.13)) are compared to the results of the simulation.

(a) Ring object (b) Tomosynthesis

Figure 4.6: (a) Simulated ring object located at $z = 1.0$ cm. (b) Tomosynthesis reconstruction of ring object at $z = 1.5$ cm approximately focuses to a point.

4.3 Discussion

It is interesting to note from the sensitivity demonstration that circular tomosynthesis is somewhat more immune to a single misalignment than might be expected. When a misalignment results in a blurred on-plane reconstruction of an object, the object often tends to appear better focused on another plane. Insight into this can be gained by considering a ring object, as in Fig. 4.6 (a). In the limit of many views, the on-plane reconstruction of this object looks similar to the off-plane reconstruction of a point-object at a different location (0.5 cm away from the plane for this geometry). As shown in Fig 4.6 (b), reconstruction of the ring object data at a plane 0.5 cm from the object has a strong central peak on a blurry background. The image results from the convolution of the ring (Fig. 4.6(a)) with a ring of equal diameter. This superposition of many rings into a point-like object suggests two things about circular tomosynthesis. First, anatomic objects which have a ring-like structure, such as cross-sections of arteries, can be incorrectly interpreted as point-objects in another location. Second, point-objects which are blurred into a ring by system misalignments may tend to re-focus at another plane, just as a ring can appear as a point-like structure.

For many misalignments of a single parameter, as discussed above, the reconstructed object appears better focused on a plane other than the one in which the object is located. This shift, as well as in-plane distortions, depend on the details of the system and the error in that parameter. When there are errors in multiple parameters, their combined effect may no longer be as benign due to their interaction. As a result, the effect of simultaneous misalignments of multiple parameters may be worse than one might expect based on the results for individual misalignments. A study of the effects of multiple misalignments may be warranted, since they will generally be present in an actual system. This certainly is the case for the volumetric tomography system, as demonstrated in Ch. 5. This was not done here, since the goal was to highlights some of the geometrical parameters which are important to know. This motivates the need to correct for the misalignments in order to produce high quality images.

As previously described, the reconstruction image location, i.e., the location with the least amount of blurring, was defined by minimizing the diameter of the transverse response as a function of reconstruction height. This was calculated by minimizing the derivative with respect to ϕ of the first order Taylor's series expansion of the backprojection equation for a point-object. This approach was motivated by the desire to minimize an average value of the blur diameter with respect to the reconstruction plane. The result of this operation for an aligned system would be zero on the plane in which the object lies, since, on this plane, the location of the backprojected point is independent of ϕ. For the most part, this approach worked well. However, one could imagine a blurring for which the derivative with respect to ϕ would not give a good indication of the average blur diameter. As an alternative, one could take the derivative of the width of the reconstructed point-object with respect to z. This approach is motivated by the assumption that the impulse response for a misaligned system is a slight modification of that for an aligned system (Fig. 2.5). This response would change mainly as a function of z, and the derivative of the response width with respect to z would therefore be a good basis for the definition of the slice thickness and the plane for which the object best focuses. This approach could be taken in instances where the approach used here might not be adequate.

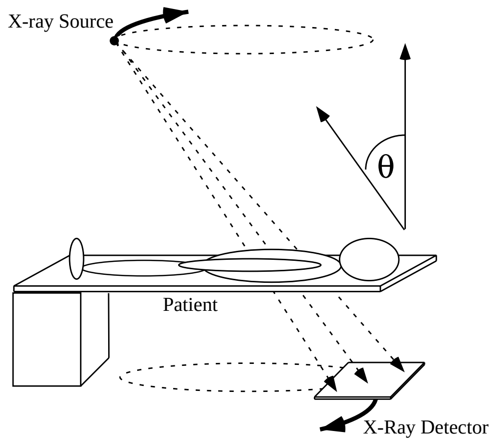

Figure 4.7: Motion of the x-ray tube and detector in a clinical circular tomosynthesis system.

The demonstration of the sensitivity to geometrical misalignments presented in this chapter applies to our in-vitro imaging system. It is useful to examine how this analysis would change for a clinical system in which the patient is stationary and the x-ray tube and detector move. One likely construction of such a system, Fig. 4.7, differs in motion relative to our system by a rotation of the detector about the detector normal, i.e., the detector in the clinical system does not rotate about its own axis as it moves under the patient, while the motion in our system is equivalent to that of the clinical system with an additional rotation. Because of this, the clinical system has a mechanical focal plane such that points in this plane always project onto the same detector pixel as the data are collected. For a system with a stationary detector, the mechanical focal plane is on the detector itself. This distinction causes two system-level differences. Certain misalignments of the detector will have minor effects on the clinical system. A lateral translation or a rotation of the detector about its axis would simply translate or rotate the image. Misalignment of the normal to the detector would have a similar effect as for the in-vitro system. On the other hand, detector nonidealities (e.g. blemishes) will focus on the mechanical focal plane of the clinical system and produce artifacts just as in a radiograph. In comparison, the detector nonidealities are circularly blurred (on all planes) in our in-vitro system.

4.4 Conclusions

The sensitivity of circular tomosynthesis to mechanical alignment errors of the volumetric tomography system was studied analytically and using computer simulations. This analysis provides the framework for a correction technique, which is presented in Ch. 5. Without this correction, the high sensitivity to misalignments would preclude useful imaging. As discussed, this sensitivity will change somewhat for an in-vivo imaging system in which the x-ray tube and detector move about a stationary patient.

Chapter 5

Correction for Misalignment

5.1 Introduction

The sensitivity demonstration in Ch. 4 shows that image quality is highly sensitive to the alignment of the image acquisition system. As described in Ch. 3, our design philosophy for the volumetric tomography system was to use a software technique to correct for misalignments, rather than to place strict requirements on the system alignment. This is desirable, because if a software technique can be relied on to correct for the misalignments, we can maintain both the imaging flexibility of the gantry and the low cost of the system. In order to do this, the system geometry must be measured precisely, which can be done with the x-ray system itself, and a correction technique must be developed to handle the system imperfections. In this chapter, we describe our technique, which uses a calibration scan or fiducial markers to measure the geometry of the system and then remaps the data prior to image reconstruction. The motivation for this work is not to develop a method to reliably determine a system's geometry. Instead, we are interested in developing a technique to correct the errors in tomosynthesis images resulting from geometrical misalignments. Therefore, a geometrical fit which is inaccurate, yet corrects the image errors, is acceptable here. Further study into fitting a system's geometry is beyond the scope of this dissertation.

Other authors have both measured system geometries [35–38], and mathematically corrected for geometrical distortions [32, 33, 39–42]. For example, Rougée et al. [35] have developed a technique to determine geometrical parameters for an x-ray imaging system using a limited number of reference points in a calibration phantom. The relative positions of the reference points are assumed to be known in this technique. This assumption is typically required in geometrical fitting techniques. Concepcion et al. [33] have included correction for a shift in the axis of rotation in a CT scanner into the image reconstruction algorithm. Correction for a larger number of geometrical parameters has been studied by Bronnikov [40]. Our approach differs from previous methods in the scope of the free parameters which are fit and corrected. We present this technique, as well as experimental validation using spatial resolution in the focal plane as the criterion for evaluating its performance.

5.2 Method for Misalignment Correction

The general approach is to measure the system geometry via multiple projections of small objects, and to find a set of geometrical parameters which are most consistent with the measured projections. This can be accomplished either by acquiring separate data of a calibration phantom (which requires the assumption that the gantry alignment is stable), or by using fiducial markers which are present when the object is imaged. We have used both techniques; the former approach is described here. The latter approach is identical, except that the projections of the bearings are included in the object projections, rather than in an additional scan of a calibration phantom. A numerical, iterative process was developed to determine the geometry which best matches the projection data of the calibration phantom or fiducial markers.

The calibration phantom consists of small ball bearings, which yield projections of point-like objects. The positions of the bearings need not be known, and only a small number are needed. This differs from most previous approaches to characterize a system's geometry in which at least the relative positions were assumed to be known [35,37,41,43]. A typical arrangement for our calibration phantom is 6 bearings separated by plastic or foam over a 10 cm x 15 cm x 15 cm volume. The phantom is imaged at a number of views, e.g. 10 views over 360°, with the gantry in the desired imaging geometry. The center of mass of the projection of each sphere is computed for each view.

An initial estimate of the geometry and an initial estimate of the location of each of the spheres is given to a projection simulator, which generates noiseless projections of simulated point-objects. The geometrical parameters for the projection simulator are: (1) the tomographic angle, (2) the distance from the x-ray tube to the positioning stage, (3) the distance from the tube to the detector, (4) the incremental rotation angle of the positioning stage between projections, (5) the relative locations of the objects in the calibration phantom, (6) the (two) translations of the detector perpendicular to the central ray, and (7) the (two) rotations of the detector relative to the central ray. The measured and simulated projection centroids are compared, and the root mean squared difference (RMS) between the predicted and measured centers is computed. One of the geometrical parameters is incremented by a small amount (within an allowed range), constrained to always have the source to detector distance greater than the source to object distance. A new RMS statistic is calculated, and the updated parameter is accepted if the fit statistic is decreased. This iterative process cycles over all of the geometrical parameters, and is continued until the change in the statistic is smaller than a threshold value.

While this approach may not give the true geometry of the system, it yields parameters which give projections that are consistent with the measured data. If the agreement is good (e.g. subpixel), the system can be expected to provide high spatial resolution at (or near) the location of the spheres. By using objects/markers throughout the volume of interest, the geometry provided by the numerical geometry fitter can be used to generate high quality backprojected images throughout the volume. This is acceptable because the goal is to reconstruct high quality images, rather than necessarily to determine the system's true geometry.

For a calibration phantom with N spheres, there are $3N + 8$ parameters. This differs from previous approaches in that, secondary to the fact that the object locations are not known, a larger set of free parameters are allowed. The free parameters can be classified into three groups: the tomographic angle, the distance from the x-ray tube to the positioning stage, the distance from the tube to the detector, and the incremental rotation angle of the positioning stage between projections are adopted by (i.e., passed to) the reconstruction program; the relative locations of the objects in the calibration phantom are just used in determining the best fit; and the (two) translations of the detector perpendicular to the central ray and the (two) rotations of the detector relative to the central ray are corrected in the remapping stage.

Figure 5.1 shows two example projection images of a typical calibration phantom used in the geometry fitting routine, taken with a 20° tomographic angle. This phantom consists of 6 small bearings. In this fit, 10 views were used over 360°. The resulting fit results are given in Fig. 5.2, which have an RMS statistic of 0.24 pixel.

The geometric fit to the data is used to remap (resample) the data onto a perfectly aligned detector. For a given pixel on the aligned detector, the projection ray from the tube to that pixel is defined. The intersection of this ray with the actual detector is calculated, and data for this output pixel is computed from the pixels on the actual detector using two successive third order 1D polynomial interpolations. The remapping of the data prior to backprojection adds an interpolation step, which blurs the data according to the type of interpolation performed. This is in addition to the interpolation done at backprojection. Alternatively, the remapping could be included in the backprojection algorithm, requiring only one interpolation step in the entire process.

5.3 Experiments

The volumetric tomography system was used to collect radiographic images and tomosynthesis datasets for a bar pattern phantom (Fig. 5.5 (a)) and a tomographic phantom with tomographic angle 40°, SO = 77 cm, and SD = 127 cm. The tomographic phantom (Fig. 5.3) contains 12 lead numerals, each on a different plane which is separated in height from its neighbor by 1 mm. The tomosynthesis datasets for each phantom were remapped as described in Sec. 5.2. For this dataset, the geometrical fitting routine measured: a 1.8° error in the tomographic angle relative to the axis of rotation of the positioning stage, a (2.3, 0.27) cm translation of the detector, and a (0.29°, 1.1°) rotation of the detector.

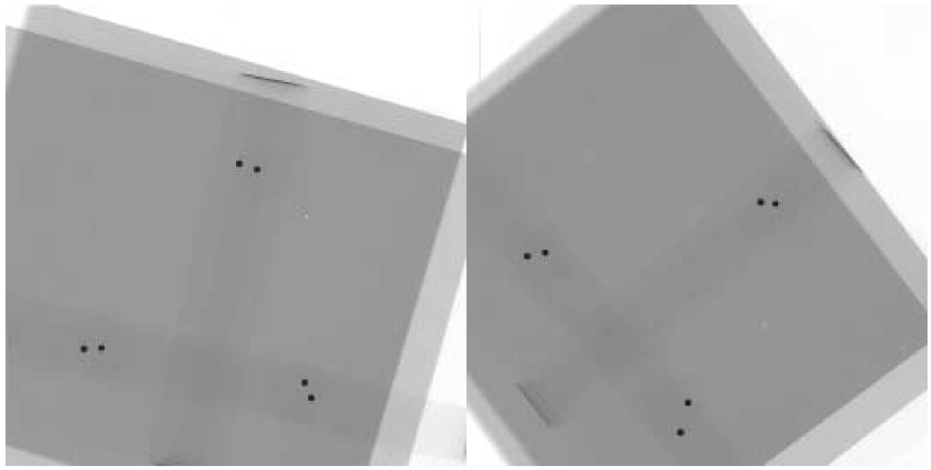

Figure 5.1: Two projection images of a calibration phantom consisting of 6 small bearings separated by a layer of foam. The stage is rotated by 36° between the left and right images.

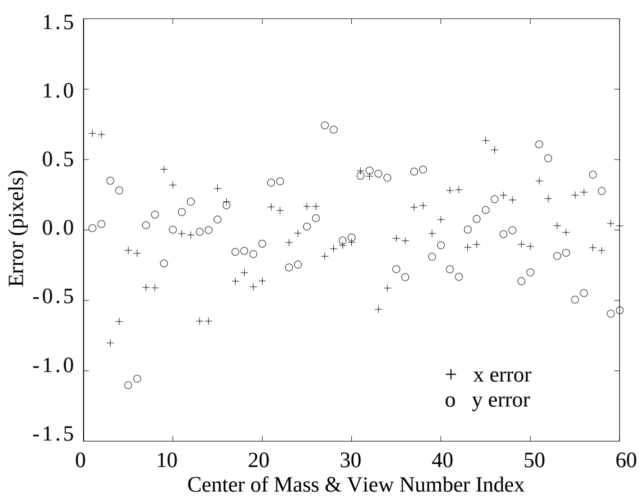

Figure 5.2: Residual errors resulting from the geometric fit to 10 views of a calibration phantom with 6 small bearings (Fig. 5.1). The RMS statistic is 0.24 pixel for this case.

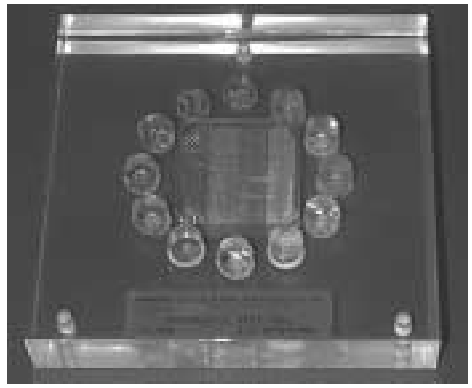

Figure 5.3: Tomographic phantom. Each of the 12 numerals is separated in height from its neighbor by 1 mm.

To qualitatively measure the performance of the software alignment technique, the raw tomographic phantom data were reconstructed using unfiltered backprojection assuming an aligned system, and then after remapping using the measured system geometry. Third order polynomial interpolation steps were used in both the remapping and reconstruction stages.

In order to quantitatively evaluate the effectiveness of the remapping technique, the bar pattern phantom data were remapped and reconstructed, and the peak-to-peak signal modulation of a (vertical) column of pixels through the bar pattern was compared to the peak-to-peak signal modulation of a radiograph acquired with the same system ($\theta = 0$). In both cases, $M(k)$ was defined as the modulation at square wave frequency k, unnormalized other than for the number of views in the tomosynthesis data. While $M(k)$ is not the true modulation transfer function (MTF) of the system, it mimics the MTF and gives information about the spatial resolution of the system. We are not attempting to measure the MTF, but rather want to evaluate the performance of the geometry correction technique by comparing $M(k)$ of a tomosynthesis image with that of a radiograph from the same system. The tomosynthesis images are expected to have lower modulation due to the effect of the two interpolation steps. To estimate the upper bound of the expected performance of the tomosynthesis system, we multiplied $M(k)$ for the radiograph ($\theta = 0$) by the square of the MTF of the cubic interpolation.

As in Press [44], a 1D third order polynomial interpolation of a function $f(x)$ at the point $x_2 \leq x \leq x_3$ can be written as:

$$\begin{aligned} f_{int}(x) = & \frac{(x-x_2)(x-x_3)(x-x_4)}{(x_1-x_2)(x_1-x_3)(x_1-x_4)} f(x_1) + \frac{(x-x_1)(x-x_3)(x-x_4)}{(x_2-x_1)(x_2-x_3)(x_2-x_4)} f(x_2) \\ & + \frac{(x-x_1)(x-x_2)(x-x_4)}{(x_3-x_1)(x_3-x_2)(x_3-x_4)} f(x_3) + \frac{(x-x_1)(x-x_2)(x-x_3)}{(x_4-x_1)(x_4-x_2)(x_4-x_3)} f(x_4). \end{aligned} \tag{5.1}$$

This interpolation has impulse response $i(x)$ which is defined as:

$$i(x) = \begin{cases} \frac{(x-x_1)(x-x_2)(x-x_3)}{(x_4-x_1)(x_4-x_2)(x_4-x_3)} & \text{if } x_0 \leq x \leq x_1, \\ \frac{(x-x_1)(x-x_2)(x-x_4)}{(x_3-x_1)(x_3-x_2)(x_3-x_4)} & \text{if } x_1 \leq x \leq x_2, \\ \frac{(x-x_1)(x-x_3)(x-x_4)}{(x_2-x_1)(x_2-x_3)(x_2-x_4)} & \text{if } x_2 \leq x \leq x_3, \\ \frac{(x-x_2)(x-x_3)(x-x_4)}{(x_1-x_2)(x_1-x_3)(x_1-x_4)} & \text{if } x_3 \leq x \leq x_4. \end{cases} \tag{5.2}$$

The Fourier transform of $i(x)$, $I(k)$, gives the expected frequency response of the interpolation scheme. Because of the two interpolation steps (remapping and back-projection), the signal magnitude $M(k)$ of the reconstructed image is modeled by $M(k)$ of the radiograph multiplied by the square of $I(k)$.

5.4 Results

Figure 5.4 (a) shows the reconstruction of the tomographic phantom with no correction (i.e., assuming an aligned system). On the plane shown, the numeral 1 should be in focus, but the entire image is blurred because of the geometrical misalignments. An image reconstructed after applying the geometry fitting and remapping technique to the same data is shown in Fig. 5.4 (b). Here, the numeral 1 is in focus, and the off-plane objects are blurred in circles with radii increasing with the distance from the focal plane, as expected.

The radiograph of the resolution phantom, shown in Fig. 5.5 (a), contains intensity modulation out to 2.5 lp/mm, consistent with the 200 μm pixel size of the detector.

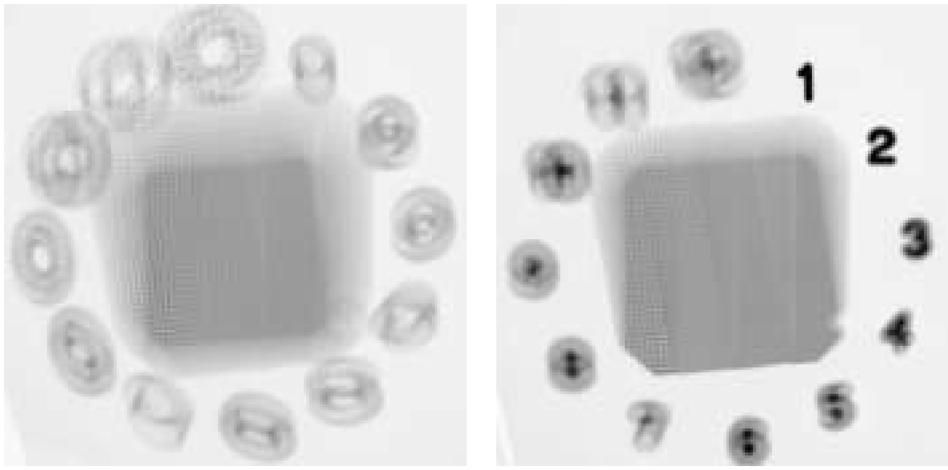

(a) Uncorrected (b) Corrected

Figure 5.4: Shown here are reconstructions of a tomographic phantom on the plane containing the numeral 1, for (a) data from a [misaligned] system which has not been corrected for geometrical misalignments and (b) reconstruction of the same data from the misaligned system, which has been remapped using the geometry fitter technique.

The tomosynthesis image of the phantom, Fig. 5.5 (b), shows somewhat poorer resolution. However, as shown in Fig. 5.6, the frequency response of the reconstructed tomosynthesis image is consistent with expectations. The degradation of the square wave modulation relative to that of the radiograph is approximately as expected from the interpolation steps.

5.5 Discussion

As discussed in Sec. 5.2, the system geometry can be measured using either fiducial markers or a separate scan of a calibration phantom. Each method has its advantages, and both can be performed using the techniques outlined in this chapter. The use of a separate scan with a calibration phantom requires the assumption that the geometry misalignments are stable, an assumption that is not needed when using fiducial markers. Fiducial markers, however, introduce artifacts into the images and can obscure part of the volume of interest. The appropriate choice depends on the

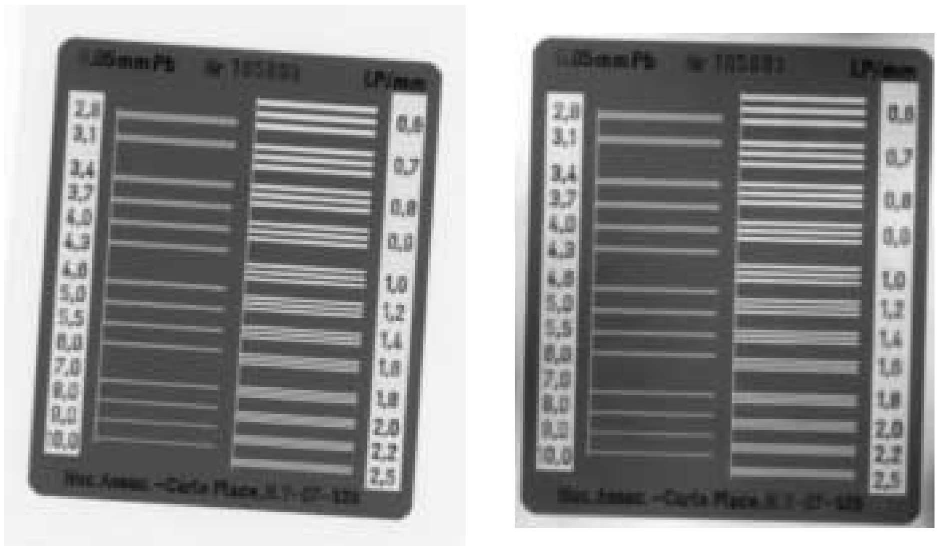

(a) Radiograph (b) Tomosynthesis

Figure 5.5: (a) Radiograph of the resolution three-bar phantom. (b) Tomosynthesis image reconstructed on the plane through the phantom demonstrating image quality maintained by the geometry software corrections technique, with loss in resolution due to the interpolation steps.

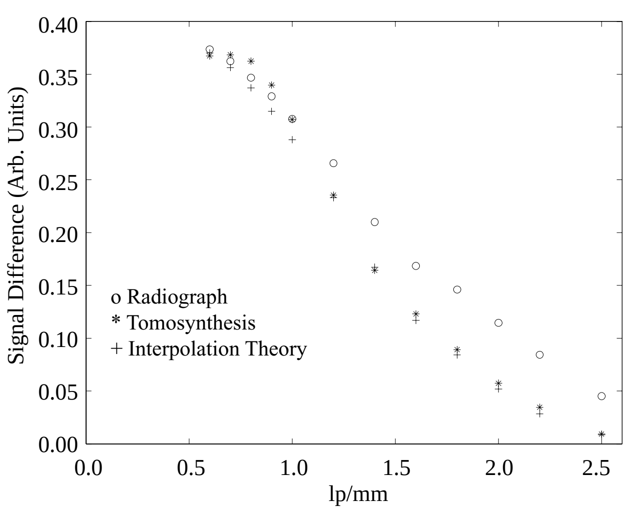

Figure 5.6: Signal modulation of a column of pixels through a three-bar resolution phantom. The data points measured in the reconstructed tomosynthesis image match well with the interpolation theory.

specific imaging conditions.

As shown in Fig. 5.6, the frequency response of the tomosynthesis system matches the theoretical expectations based on the radiographic resolution and the effect of the interpolation steps. This suggests that the spatial resolution in the final images is limited by the inherent resolution of the detector and by the interpolation steps in the remapping and reconstruction techniques, rather than by the accuracy of the geometrical alignment. Some increase in resolution (with an upper bound given by the inherent resolution of the detector) can be achieved by higher quality interpolation, at the expense of extra computation time, and/or by merging the remapping and backprojection into a single step. Thus, tomosynthesis images with spatial resolution equaling the theoretically predicted values can be obtained from a volumetric tomography system which was not precisely aligned. Examination of the output of the geometry fitter showed that the system contained many of the types of misalignments shown in Ch. 4. Without correction for these errors, the images would have been unusable (e.g. Fig. 5.4 (a)).

As described above, no claim is made regarding the accuracy of the geometrical fit. It would be interesting to measure the actual misalignments of the system, and compare them with the corresponding fit parameters. In addition, simulations could be performed to analyze the range of misalignments over which the system's geometry can be accurately fit. Our interest, however, was to produce high quality tomosynthesis images from our volumetric tomography system. The technique outlined in this chapter was able to do this for all of the imaging situations that we encountered. While further investigation into fitting the geometry may be warranted, it is beyond the scope of this work.

5.6 Conclusions

We have developed a software technique to correct for the alignment errors in our volumetric tomography system. This technique takes the place of precise mechanical alignment of the system, and retains the high degree of flexibility of the tomography system. Fitting the system geometry and remapping the data yields tomosynthesis images with spatial resolution consistent with theoretical expectations. The technique outlined here represents a viable alternative to precise mechanical alignment of a tomography system.

Chapter 6

Filtered Backprojection

6.1 Introduction

As discussed in Ch. 2, a tomosynthesis image of a 3D object consists of a plane which is in focus, while the the rest of the object is blurred. The type of blurring of off-plane objects in tomosynthesis images is dependent on the type of motion used during data acquisition. Simple linear motion blurs objects in one dimension only, leading to linear streak artifacts which can obscure useful information in the images [7]. Circular motion of the source and detector results in out-of-plane points being blurred into rings, while more complex motions, such as hypocycloidal motion, result in blur functions which are more appealing (i.e., less disturbing) to the observer [8]. The blur functions resulting from the complex motions are desirable because they more uniformly blur off-plane objects. This can avoid potential problems with the ring blurring of circular tomosynthesis, as described in Sec. 4.3. The complex motions are an attempt at creating a uniform blurring, but are limited by the mechanical motion required to produce the blur shape.

Other authors have attempted to suppress the information from objects lying outside the plane of interest by selecting an optimal imaging geometry [45] or filtering the data [30, 31, 46]. Ruttimann et al. [45] attempted to improve object visualization by filling in the circle of x-ray source position, i.e., using a more complex system motion. Post-processing filters were used by Ghosh Roy et al. [46], to suppress the signal from neighboring planes, and Badea et al. [30], to remove the signal from high frequency, high contrast objects for sparse imaging applications. A linear systems approach was used by Lauritsch and Härer [31] to study a filtered backprojection approach. Our method differs from previous approaches in its use of filtered back-projection to achieve equivalent results to those from systems with more complex motions, for general application to complex objects. This expands the linear system approach by focusing on the development of relevant filters.

In this chapter, we present a filtering technique to modify the 3D impulse response of circular motion tomosynthesis to allow the generation of images whose appearance is like those of some other imaging geometry. In particular, an off-focal plane point can be blurred into a disk (i.e., similar to the behavior that hypocycloidal motion, but even more uniform), which may be less obtrusive than the standard ring-shaped blur. This approach is desirable because the uniform blurring is created by careful weighting of the data after collection, rather than by relying on an intricate mechanical motion of the x-ray tube and detector during image acquisition. In this chapter, we describe the filtering technique, and demonstrate the ability to change the impulse response in circular motion tomosynthesis from a ring to a disk.

6.2 Motivation for Filtering

Consider a circular tomosynthesis system, like our table-top system shown in Fig. 6.1 and described in Ch. 3. In this geometry, the x-ray tube and detector are stationary while the object being imaged is placed on a positioning stage, and rotated through 360° between x-ray exposures. (The equivalent clinical system would consist of an x-ray tube and detector rotating about the stationary patient.) The projection angle, θ, is defined as the angle between the central ray of the x-ray beam and the axis of rotation of the positioning stage, i.e., the tube and detector are rotated from vertical by θ. The tomographic angle is defined as twice the projection angle.

Assume for now that the x-ray source emits parallel, monochromatic x-rays. The Projection-Slice Theorem states that for a projection angle θ and a positioning stage angle ϕ, the Fourier transform of the 2D projection data (i.e., the negative logarithm

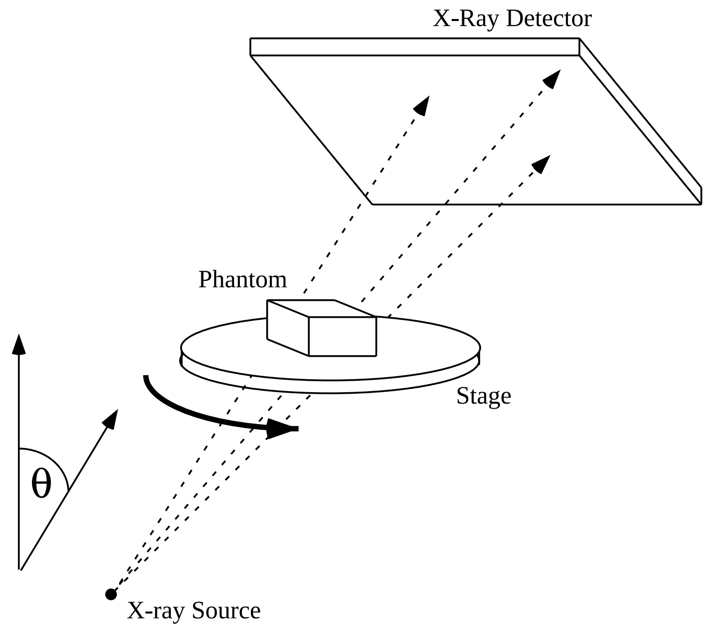

Figure 6.1: Phantom-based circular tomosynthesis system.

of the measured transmission) is equal to the 3D Fourier transform of the object on the plane through the origin with normal $(\sin\theta\cos\phi, \sin\theta\sin\phi, \cos\theta)^T$. This is depicted in Fig. 6.2. As the stage is rotated from 0 to 2π, the plane in frequency space sweeps out a cone. For an infinite number of views, every point in Fourier space outside the cone defined by the angle $\pi/2 - \theta$ is sampled, while all points inside the cone are not sampled [31, 47]. By comparison, a radiograph ($\theta = 0$) samples only the $k_z = 0$ plane, while CT ($\theta = \pi/2$) samples all of Fourier space. It is impossible to perform a perfect reconstruction in tomosynthesis, because not all of the frequencies are sampled.

The impulse response of the system depends on the frequencies that were sampled, and the weighting applied to them. Changes in the weighting of the frequencies which are sampled leads to changes in the impulse response. As an example, it is possible to reconstruct, from a circular tomosynthesis dataset, a radiograph from a source position that was not acquired as long as this source position is inside the circular path. For example, a radiograph with a source position located at the center of the circular path can be reconstructed. This is possible because the region in

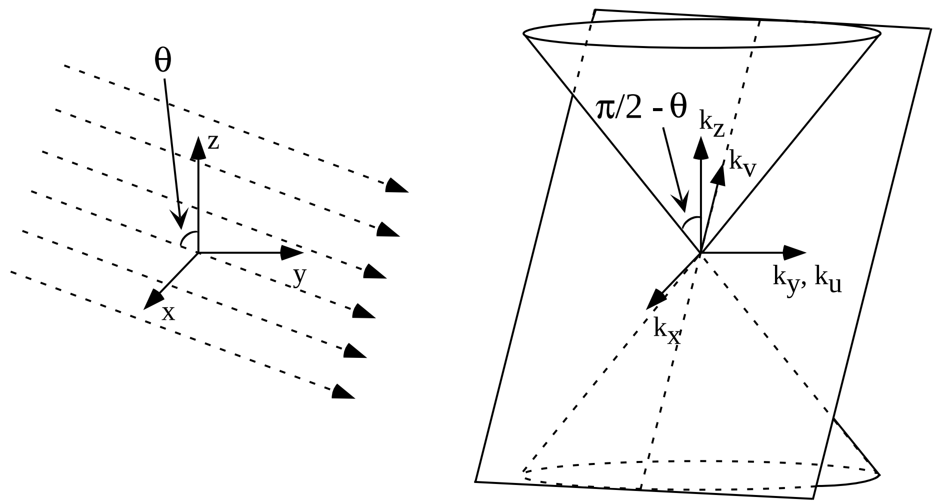

Figure 6.2: Frequency space sampling in circular tomosynthesis. The left side illustrates the direction of a projection and the right side shows the planar region in Fourier space sampled by the projection.

frequency space sampled by the radiograph is a subset of the region sampled by circular tomosynthesis. Because the radiograph (at $\theta = 0$) samples only the $k_z = 0$ plane, all other frequencies in the filtered data must be set to zero, and the frequencies within the $k_z = 0$ plane must be properly weighted. The resulting image would look like a radiographic image except for differences in the noise level, as discussed below. Similarly, data acquired with circular tomosynthesis with tomographic angle 2θ can be filtered to produce an impulse response identical to that from a system with tomographic angle $2\theta' < 2\theta$.

While the processing to alter the impulse response could be performed in 3D frequency space, it is also possible to the achieve the same results using filtered backprojection. Consider the backprojection of a 2D projection into a 3D volume. The Fourier transform of the backprojection of a single projection image is non-zero only on the plane in frequency space through the origin and orthogonal to the direction of backprojection. Therefore, filtering a 2D projection prior to backprojection affects

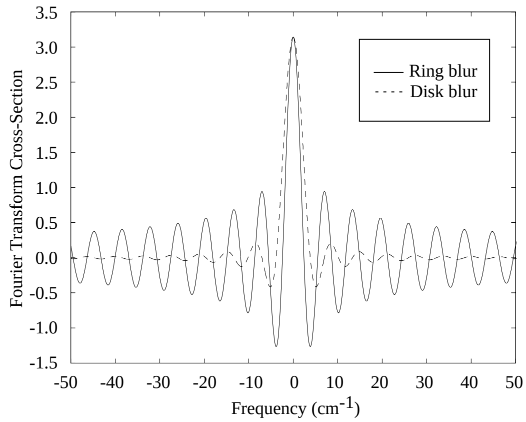

Figure 6.3: Cross-section of the Fourier transforms of a ring and a disk.

only the spatial frequencies measured by that particular projection. Thus, the reconstruction processing can be accomplished by filtered backprojection, and the 2D filter that needs to be applied to each projection image is equal to a plane through the 3D filter that would be used to filter the entire volume. In this way, filtering to alter the impulse response becomes a 2D problem, acting on the Fourier transform of each of the measured projections.

It is the goal of this chapter to create a filter which will blur off-plane objects as uniformly as possible while faithfully depicting on-plane objects. Our approach is to blur point-objects into a disk as the reconstruction plane moves away from the object, keeping the tomographic angle constant. This is desirable because the disk blur has less high frequency content than the ring blur. This can be understood by examining the Fourier transforms of a ring and a disk, which are the Bessel functions J_0 and J_1, respectively. As shown in Fig. 6.3, the Fourier transform of the disk has much lower frequency content than the ring. It is important to note that this is the frequency content of the blurring, rather than of the on-plane object, and therefore this energy at high frequencies is not necessarily good. No spatial information for the on-plane object is lost by the filtering, as is discussed below. This is an important property of the filter, since the desired effect is to alter the presentation of the off-plane objects without corrupting the on-plane image.

6.3 Filter Construction

In order to generate a disk-shaped blur response, we approximate a disk by the superposition of many rings. This, in turn, looks like the superposition of blur functions from circular tomosynthesis at many tomographic angles in the range $[0, 2\theta]$. We begin by developing a filter that, when applied to data acquired with a tomographic angle 2θ, produces images with the impulse response expected for a circular tomosynthesis system with tomographic angle $2\theta_i$ $(0 \leq 2\theta_i \leq 2\theta)$.

Two steps are needed in order to modify the impulse response. First, the frequencies not sampled by $2\theta_i$ need to be discarded. Second, for the frequencies sampled by both imaging geometries, a frequency-dependent weighting factor is needed to convert the Fourier space sampling density for 2θ to that for $2\theta_i$. Thus, it is useful to calculate the Fourier space sampling density for circular tomosynthesis with tomographic angle 2θ.

Consider an object which is imaged using circular tomosynthesis. As in Pelc [47], we define the sampling density, $D(k_x, k_y, k_z)$, to be the ratio of the Fourier transform of an image generated by unfiltered backprojection, $I(k_x, k_y, k_z)$, to the object's Fourier transform, $A(k_x, k_y, k_z)$. That is:

$$D(k_x, k_y, k_z) = \frac{I(k_x, k_y, k_z)}{A(k_x, k_y, k_z)}. \tag{6.1}$$

For circular tomosynthesis, we know that D is circularly symmetric about k_z. The sampling density D can be computed for any object. For simplicity, assume that the object is centered and symmetric about the z-axis. This will not limit the applicability of the filter in any way. As a result, the backprojected image's transform is symmetric about k_z. In addition, assume that there are enough views so that I, A, and the density D are continuous over the spatial bandwidth, and assume that the views are equally spaced through 360° in ϕ. Therefore, in spherical coordinates,

$$D(k, \alpha) = \frac{I(k, \alpha)}{A(k, \alpha)}, \tag{6.2}$$

where α is the angle between the vector $\overrightarrow{k}$ and the k_z axis. From symmetry, $I(k_o, \alpha_o)$ is equal to the average value of I over a circle at $k = k_o, \alpha = \alpha_o$, which we can calculate by integrating I over that circle and dividing by the circumference of the circle ($2\pi k_o \sin\alpha_o$). This approach is useful as a way of dealing with the delta functions in the Fourier space sampling pattern while calculating the expected value for a point on the circle. As shown in Fig. 6.2, each projection samples a plane (in the 3DFT of the object) in Fourier space, and backprojection of each projection image contributes to a plane (in the 3DFT of the image) in Fourier space, which the circular path of integration crosses twice. From symmetry, the value of the image transform at each of the crossing points is $A(k_o, \alpha_o)$ times a delta function in the direction normal to the projection image plane. Therefore, the integration along the circle, over and at an angle to this delta function, is proportional to $1/\sin\gamma$, where γ is the angle between the tangent of the circle and the plane in Fourier space. Thus, for any measured spatial frequency (i.e., $\alpha \geq \pi/2 - \theta$):

$$I(k,\alpha) = \frac{\int I(k,\alpha)\,ds}{\int\,ds} = \frac{m_\theta A(k,\alpha)}{\pi k \sin\alpha \sin\gamma} = \frac{2m_\theta A(k,\alpha)/\sin\gamma}{2\pi k \sin\alpha}, \tag{6.3}$$

where m_θ is the number of views. Since $\sin\gamma = \sin\theta\sqrt{1-\cot^2\theta\cot^2\alpha}$, Eq. (6.3) can be rewritten:

$$I(k,\alpha) = \frac{m_\theta A(k,\alpha)}{k\pi \sin\theta \sin\alpha\sqrt{1-\cot^2\theta\cot^2\alpha}}. \tag{6.4}$$

Substituting Eq. (6.4) into Eq. (6.2) yields:

$$D_\theta(k,\alpha) = \begin{cases} 0 & \text{if } \alpha < \frac{\pi}{2} - \theta, \\ \frac{m_\theta}{k\pi\sqrt{\sin^2\theta\sin^2\alpha - \cos^2\theta\cos^2\alpha}} & \text{if } \alpha \geq \frac{\pi}{2} - \theta. \end{cases} \tag{6.5}$$

Alternatively, the sampling density D can be calculated directly, as follows. The distance from a sampled point in Fourier space to the nearest sampled point from another view is the inverse of the sampling density. Consider a point (k_o, α_o), which will lie in a sampled plane, given a sufficiently large number of views. Again, examine a circle at $k = k_o$, $\alpha = \alpha_o$. Because there are m_θ equally spaced views, each of which samples a plane that intersects the circle twice, the arc length along the circle from the point (k_o, α_o) to the intersection of the circle with the sampled plane of the next view is the circumference of the circle divided by twice the number of views, i.e., $\frac{2\pi k_o \sin\alpha_o}{2m_\theta}$. In the limit of a large number of views, this is also the chord length between these two points for the circle at $k = k_o$, $\alpha = \alpha_o$. The shortest distance from the point (k_o, α_o) to the next sampled plane is along the line normal to that plane. The angle between the chord and this line is γ, the same angle as between the tangent of the circle and the sampled plane. Therefore, the shortest distance between the point (k_o, α_o) and a point in the next view is $\frac{2\pi k_o \sin\alpha_o \sin\gamma}{2m_\theta}$. Thus, for a general point (k, α), in the sampled region of Fourier space, the sampling density D is $\frac{m_\theta}{\pi k \sin\alpha \sin\gamma}$, as in Eq. (6.5).

It should be noted that these derivations are not valid for $\theta = 0$. This does not mean that one cannot generate an image which looks like that from a $\theta = 0$ dataset. Rather, a different approach is needed, since the assumption of the first method of crossing the backprojected plane twice does not hold for $\theta = 0$, and the distance between view planes is zero for the second approach.

Equation (6.5) gives the sampling density for circular tomosynthesis with tomographic angle 2θ. In order to make a 2θ dataset look like a $2\theta_i$ dataset ($2\theta_i \leq 2\theta$), we need to multiply the Fourier transform of the measured data by the ratio of the densities at $2\theta_i$ and 2θ. The value of the density ratio, assuming equal numbers of views in each geometry, is:

$$R_{\theta,\theta_i} = \begin{cases} 0 & \text{if } \alpha < \frac{\pi}{2} - \theta_i, \\ \frac{\sqrt{\sin^2\theta \sin^2\alpha - \cos^2\theta \cos^2\alpha}}{\sqrt{\sin^2\theta_i \sin^2\alpha - \cos^2\theta_i \cos^2\alpha}} & \text{if } \alpha \geq \frac{\pi}{2} - \theta_i. \end{cases} \tag{6.6}$$

Equation (6.6) gives the ratio of the sampling densities in 3D frequency space, but we are interested in the sampling densities on the planes corresponding to each projection at tomographic angle 2θ (i.e., the plane in frequency space through the origin and perpendicular to the actual projection direction) because that is how the filtering will be applied. This can be described in terms of of the natural coordinate system of the detector (i.e., a 2D coordinate system on the detector surface with the origin at the detector center). The points (k, α) which fall on this plane are related to the natural coordinates on this plane (Fig. 6.2), k_u and k_v, by:

$$k \cos\alpha = k_v \sin\theta \quad , \quad k^2 = k_u^2 + k_v^2. \tag{6.7}$$

Substituting Eq. (6.7) into Eq. (6.6) yields:

$$R_{\theta,\theta_i}(k_u, k_v) = \begin{cases} 0 & \text{if } \alpha < \frac{\pi}{2} - \theta_i, \\ \frac{|k_u|\sin\theta}{\sqrt{k^2\sin^2\theta_i - k_v^2\sin^2\theta}} & \text{if } \alpha \geq \frac{\pi}{2} - \theta_i. \end{cases} \tag{6.8}$$

The filter described in Eq. (6.8), when applied to data acquired and backprojected with tomographic angle 2θ, will produce an image which appears as though it were taken with tomographic angle $2\theta_i$. Each $2\theta_i$ filter produces a ring-shaped blur for off-plane point-objects. We can form a disk-shaped blur as a weighted superposition of rings. The filter to accomplish this is:

$$F_\theta(k_u, k_v) = \int R_{\theta,\theta_i}(k_u, k_v) s_{\theta_i}\, d\theta_i, \tag{6.9}$$

The scaling term s_{θ_i} is needed because each ring has an intensity inversely proportional to its radius, i.e., $r_{\theta_i} \propto \tan\theta_i$. The ring intensity also scales as $1/\cos\theta_i$. This latter factor arises in the unfiltered $2\theta_i$ dataset due to the angle between the backprojection direction and the reconstruction plane; it arises in our case because Eq. (6.8) produces an image identical to that from the $2\theta_i$ dataset. In addition, rings equally spaced as a function of θ_i are nonlinearly spaced as a function of r_{θ_i}. Thus:

$$s_{\theta_i} d\theta_i = \tan\theta_i \cos\theta_i d(\tan\theta_i). \tag{6.10}$$

Solving for s_{θ_i} and substituting into Eq. (6.9) gives the expression for the filter:

$$F_\theta(k_u, k_v) = \int_{\arcsin(\frac{|k_v|\sin\theta}{k})}^{\theta} \frac{|k_u|\sin\theta\sin\theta_i\sec^2\theta_i}{\sqrt{k^2\sin^2\theta_i - k_v^2\sin^2\theta}}\, d\theta_i. \tag{6.11}$$

Evaluation of Eq. (6.11) yields the filter to produce a disk-shaped blurring function:

$$F_\theta(k_u, k_v) = \frac{k_u^2 \sin\theta \tan\theta}{k^2 - k_v^2 \sin^2\theta}. \tag{6.12}$$

Again, while the derivation above was performed assuming a circularly symmetric object, the result is valid in general and can be applied to an arbitrary (i.e., asymmetric) object. This is absolutely true for parallel ray projections collected with monoenergetic x-rays. In that case, the system is linear and space-invariant, and the derivation above applies to the point-spread function. It is approximately true for more general cases (i.e., polychromatic and/or divergent beams). This has been verified with simulations, up to the accuracy of the simulator. As will be demonstrated below, if circular tomosynthesis projections collected with tomographic angle 2θ are filtered using Eq. (6.12) (i.e., Fourier transform the data, apply the filter in Fourier space, and then inverse Fourier transform) and backprojected at 2θ, on-plane objects are unaffected and the blurring function for off-plane point-objects is a uniform disk rather than a ring.

6.4 SNR Analysis

In order to examine the effect of the filtering process on the noise in the reconstructed images, the signal-to-noise ratio (SNR) for the filtered backprojections relative to the SNR for the unfiltered backprojections was derived analytically and verified using simulations.

An analysis for the increase in noise due to the filtering can be performed by considering, for simplicity, a point-object located at the origin. Also, assume that the noise is frequency independent, with noise power spectrum N_o. For a general filter, $f(k_u, k_v)$, applied to this point-object, the SNR can be written [48]:

$$SNR = \frac{\int\int f(k_u, k_v)\, dk_u\, dk_v}{\sqrt{2\pi N_o \int\int |f(k_u, k_v)|^2\, dk_u\, dk_v}}. \tag{6.13}$$

The filter is equal to unity for the unfiltered backprojections, while the filter is given

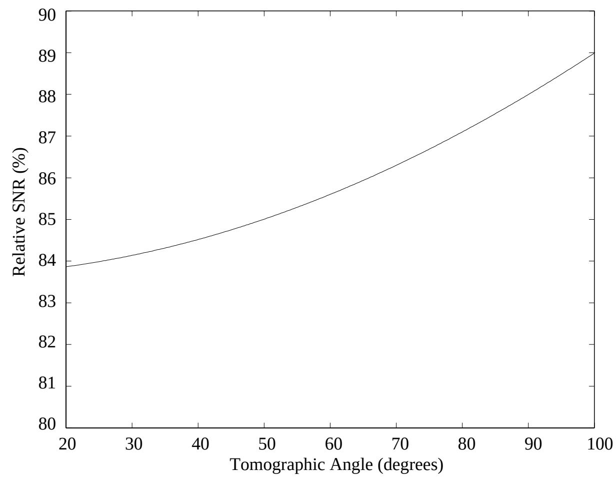

Figure 6.4: SNR for disk-filtered backprojection relative to unfiltered backprojection.

by Eq. (6.12) for the disk-filtered backprojections. Thus, the SNR of the filtered backprojections relative to the unfiltered backprojections is:

$$\frac{SNR_f}{SNR_u} = \frac{1}{2K} \frac{\int\int F_\theta(k_u, k_v)\, dk_u\, dk_v}{\sqrt{\int\int F_\theta(k_u, k_v)^2\, dk_u\, dk_v}}, \tag{6.14}$$

where K is the cutoff frequency, and the 2D integration is performed from $-K$ to K in both dimensions. Evaluation of Eq. (6.14) yields an expression for the relative SNR for the disk-filtering:

$$\frac{SNR_f}{SNR_u} = \frac{a_\theta - b_\theta \cos^2\theta + \cos\theta}{\sqrt{(a_\theta - 3b_\theta \cos^2\theta + 3\cos\theta)\cos\theta}}, \tag{6.15}$$

where $a_\theta = \arctan(\cos\theta)$ and $b_\theta = \arctan(\sec\theta)$.

The dependence of the relative SNR (on the focal plane of the reconstructed image) on the tomographic angle is shown in Fig. 6.4. In order to validate this expression for the relative SNR, noisy projections of a disk object, 4 cm in diameter and centered at the origin, were simulated. The simulated projection data were reconstructed on the plane containing the disk object, using both unfiltered and filtered backprojection with 50 views. The SNR was measured, and found to be within 3% of the analytical values for tomographic angles in the range 20° to 100°. This small discrepancy, which is independent of the number of views, is not understood at the present time, and may warrant further study.

For tomographic angles in the range 20° to 100°, the SNR is reduced by 10-15% for the disk-filtered backprojections relative to the unfiltered reconstructions. The increase in noise due to the filtering is small, however, and the improved blurring of off-plane objects may outweigh this small noise penalty.

6.5 Experiments

6.5.1 Computer Simulations

Simulations were performed in order to test the filtering process. A projection simulator (based on the analysis in Ch. 2) was used to generate noiseless projections. Projections of a small spherical object, 0.12 cm in diameter and centered at the origin, were simulated with a 40° tomographic angle. A dataset with 1000 views (equivalent to a 0.36° rotation of the stage between exposures) was generated in order to examine the filter performance with a large number of views, while datasets with 100 and 20 views were generated to study the behavior with a smaller number of views more typical of experimental tomosynthesis datasets. The detector was assumed to have a 200 μm pixel size, and the images were backprojected onto a 100 μm pixel grid. The source to object distance (SO) was 100 cm, and the source to detector distance (SD) was 125 cm. Note that while the filter derivation assumed parallel ray projections, this was not the case in the simulations.

Shown in Fig. 6.5 are unfiltered backprojection images for a simulated small spherical object for the case of 1000 views, for plane locations ranging in distance from 0 cm to 10 cm from the object location. The upper left image in the top panel is for the plane $z = 0$ cm and each plane is 2 cm higher, ending with $z = 10$ cm in the right side of the middle panel. The bottom panel shows the images for $z = 6$, 8, and 10 cm, with contrast increased by a factor of 10 (i.e., window width narrowed by a factor of 10). The image reconstructed at $z = 0$ cm shows that the object is faithfully reconstructed

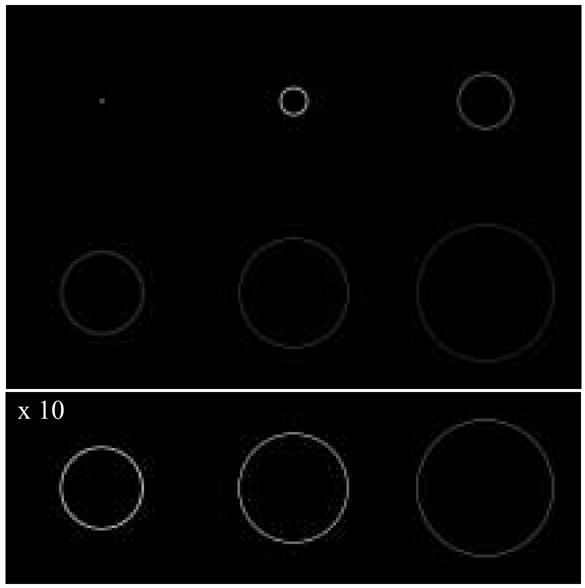

Figure 6.5: Unfiltered backprojections of a small spherical object with 1000 views.

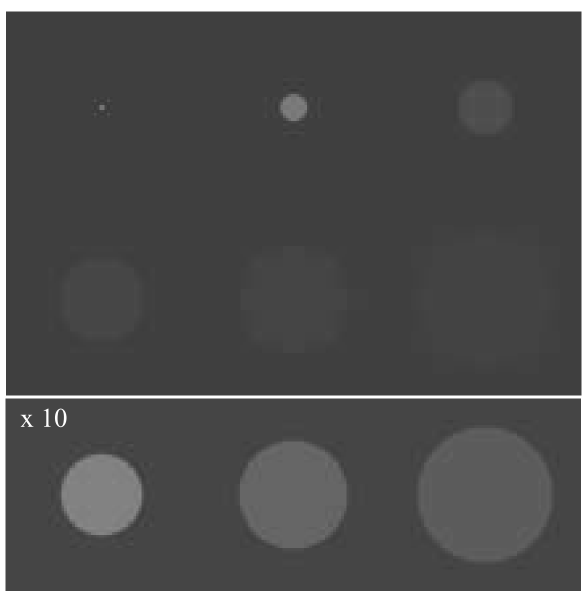

Figure 6.6: Disk-filtered backprojections of a small spherical object with 1000 views.

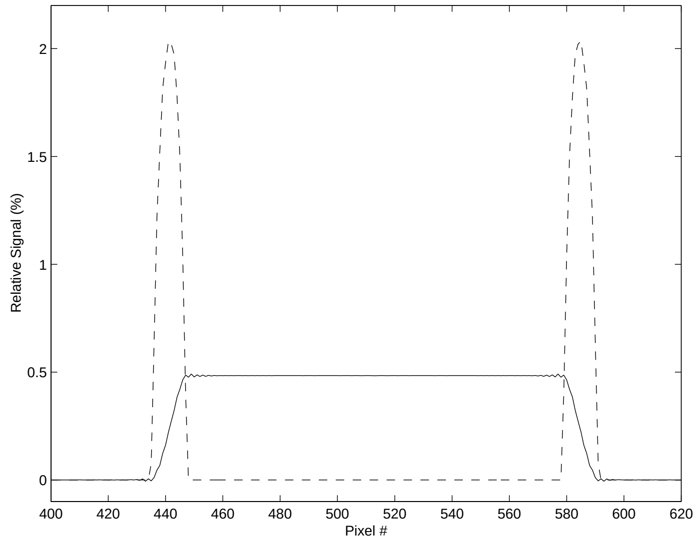

Figure 6.7: Cross-sectional plots of an off-plane reconstruction of a small spherical object for unfiltered (solid) and disk-filtered (dashed) backprojection.

on the focal plane. As the distance from this plane increases, the small sphere blurs into a ring with increasing radius and decreasing amplitude. The amplitude of the ring is inversely proportional to the ring's diameter, and therefore the distance from the focal plane. Filtering the data prior to backprojection changes the manner in which the object is blurred. Shown in Fig. 6.6 are the filtered backprojection images using the disk filter (Eq. (6.12)), corresponding to those in Fig. 6.5. The two methods give essentially identical images on the focal plane. With the disk filter, the small sphere blurs into a uniform disk away from the focal plane. The amplitude of the disk is inversely proportional to the disk's area, and therefore the square of the distance from the focal plane. Profile plots through the reconstructions at $z = 2$ cm for both unfiltered and filtered backprojection with 1000 views show the disk to be flat to better than 1%. Shown in Fig. 6.7 are the cross-sectional plots of an image reconstructed at $z = 2$ cm with 1000 views for an object located at the origin for unfiltered backprojection (dashed line) disk-filtered backprojection (solid line). The pixel intensities are shown as percentages of the intensities of the object reconstructed at $z = 0$ cm.

The reconstructions at the same plane locations for the case of 100 views are shown in Figs. 6.8 and 6.9 for unfiltered and filtered backprojections, respectively. As before, the upper left image in the top panel is for the plane $z = 0$ cm and each plane is 2 cm higher, ending with $z = 10$ cm in the right side of the middle panel. The bottom panel shows the images for $z = 6$, 8, and 10 cm, with contrast increased by a factor of 10 (i.e., window width narrowed by a factor of 10). The effect of a limited number of views if visible here. The ring blur converts to discrete points, which are especially visible at increasing distances from the object. The region over which the disk filter (or unfiltered backprojection for that matter) yields a smooth blurring function is further reduced for the 20 view case, as shown in Figs. 6.10 and 6.11. Interestingly, in the view-starved cases, the disk profile is flat in the central region of the disk, while the profile degrades to discrete dots (with negative side lobes) in a ring-like pattern at the edge of the disk. This is an extension of what happens in unfiltered backprojection. For planes near the object, unfiltered reconstructions with 100 views are indistinguishable from those with 1000 views. Eventually, as the distance from the object increases, the discrete nature of the backprojection is evident and the rings of Fig. 6.6 become discrete dots in the ring pattern. Similarly, the reconstructions with filtered backprojection with 100 and 1000 views are the same near the object. Farther from the object, the discrete dots are evident on the circumference of the disk. A plot of the pixel intensities along the circumference of the disks is shown in Fig. 6.12 for unfiltered and disk-filtered backprojection with 1000, 100, and 20 views for a reconstruction 8 cm away from the object. The pixel intensities are normalized to the intensity of the on-plane image. Away from the circumference of the disk (i.e., in the interior of the disk), the relative intensity of the disk blurring function is the same as in the 1000 view case.

6.5.2 Phantom Experiments

The filtering process was tested using experimental data of a spatial resolution pattern to verify that the image of in-plane objects is not degraded by the filtering. No loss in spatial resolution was observed in the focused image of the bar pattern phantom for the filtered backprojected image relative to unfiltered backprojection.

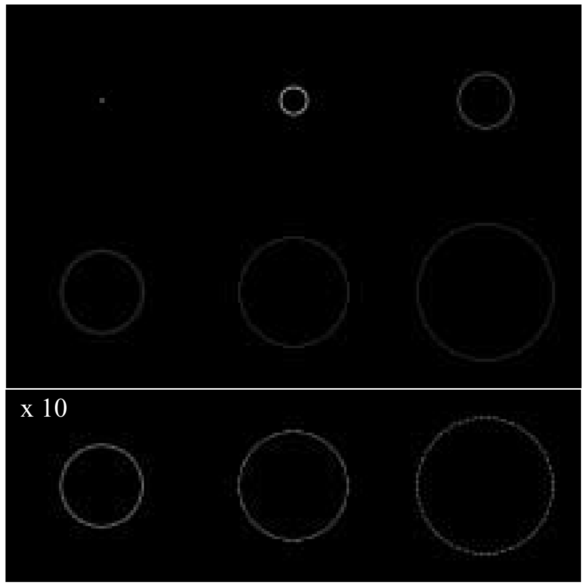

Figure 6.8: Unfiltered backprojections of a small spherical object with 100 views.

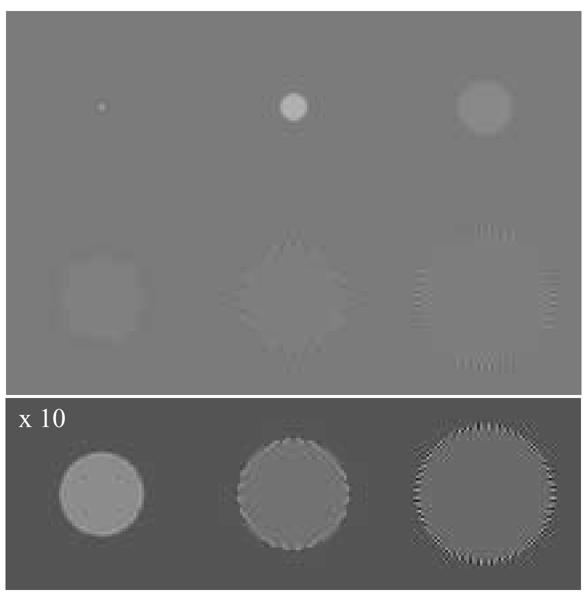

Figure 6.9: Disk-filtered backprojections of a small spherical object with 100 views.

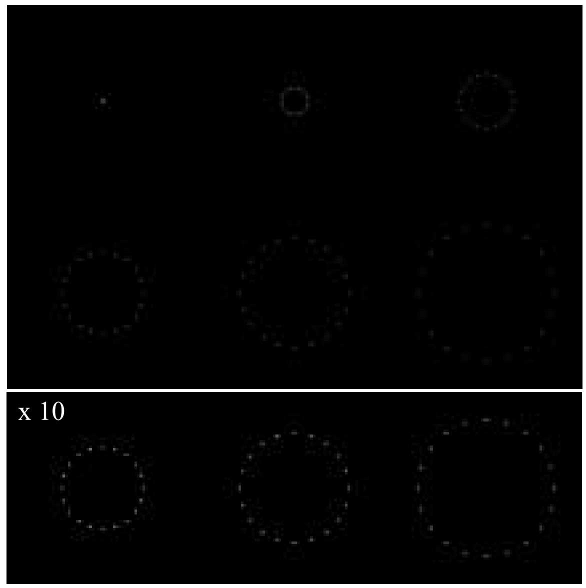

Figure 6.10: Unfiltered backprojections of a small spherical object with 20 views.

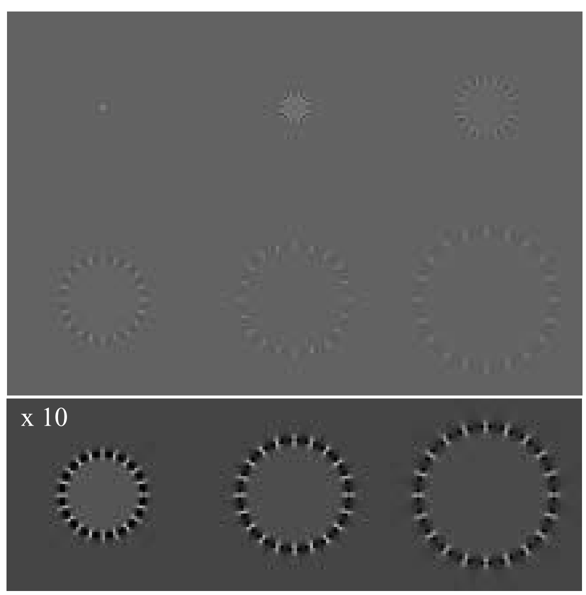

Figure 6.11: Disk-filtered backprojections of a small spherical object with 20 views.

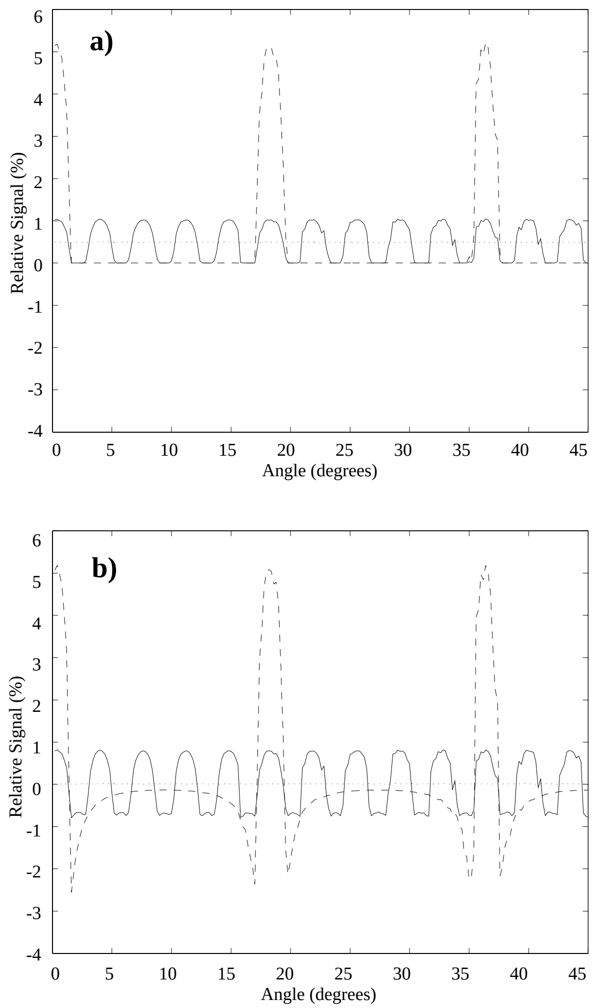

Figure 6.12: Plot of the pixel intensities along a portion of the circumference of the off-plane reconstruction of a small sphere resulting from (a) unfiltered and (b) disk-filtered backprojection for 1000 views (dotted), 100 views (solid), and 20 views (dashed).

Experimental tomosynthesis data of a desiccated dog lung (provided by Dr. Robert W. Henry, Department of Animal Science, University of Tennessee, Knoxville, TN) was collected on our volumetric tomography system (Fig. 6.1). A 100 view tomosynthesis dataset was collected for the phantom with tomographic angle 40°, $SO =$ 72 cm, and $SD = 103$ cm. The exposure parameters were 74 kVp, 80 mA, and 5 mAs per view. No attempt was made to minimize x-ray exposure. In addition, the lung phantom dataset was decimated to 20 views, and reconstructed. Note that the lung phantom images are presented as anecdotal evidence of the value of the disk filter. The benefit of this filter in clinically relevant situations is not discussed here. Rather, additional experimental applications of the disk filter to mammography and cervical spine imaging are given in Ch. 7.

Results for the application of the disk filter to the desiccated dog lung phantom are shown in Figs. 6.13 and 6.14. Figure 6.13 shows a reconstructed plane through the lung phantom using unfiltered and filtered backprojection with 100 views. The left image shows the unfiltered reconstruction focusing on the plane containing the first bifurcation of the bronchial tube. The right image shows the application of the disk-blurring filter for the same reconstruction plane. The grayscale has been inverted in order to highlight the blurred structures in both images. The arrows highlight examples of off-plane artifacts which are reduced in the filtered backprojections. Figure 6.14 shows the same plane reconstructed using only 20 views. For both reconstructions, the images with only 20 views show more discrete artifacts arising from off-plane objects. This is especially true for high spatial frequency structures, such as the smaller airways and the edges of the bronchioles. In both cases, application of the disk filter improves the blurring of the off-plane objects. The blurring of surrounding bronchioles (highlighted with arrows in Figs. 6.13 and 6.14) is less sharply defined in the filtered lung reconstructions, since the filter smoothes the artifacts as the reconstruction plane moves away from the object. This appears to help define which objects are located in the plane of interest, improving the tomographic nature of the reconstructed image.

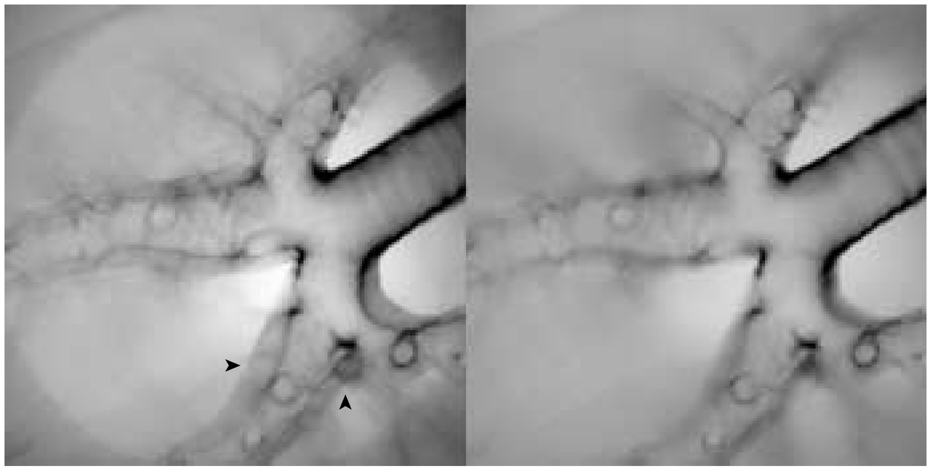

Figure 6.13: Tomosynthesis images of a desiccated dog lung phantom with 100 views, using unfiltered (left) and disk-filtered (right) backprojection.

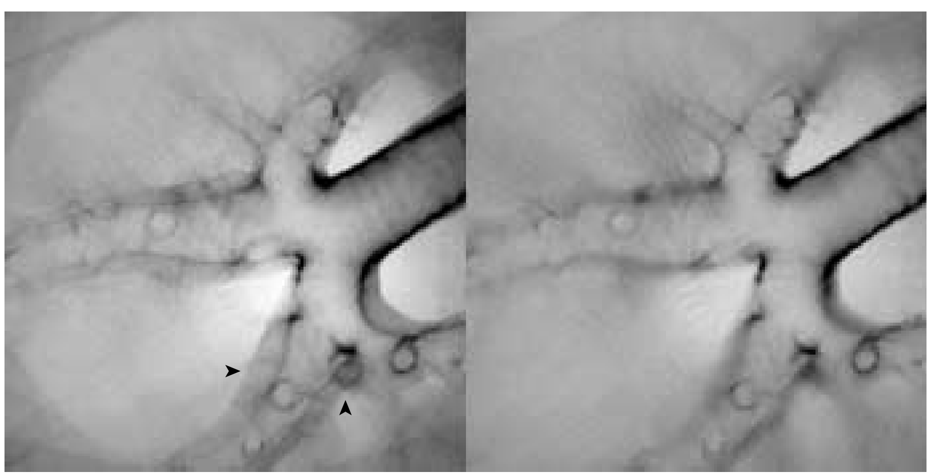

Figure 6.14: Tomosynthesis images of a desiccated dog lung phantom with 20 views, using unfiltered (left) and disk-filtered (right) backprojection.

6.6 Discussion

As shown in Fig. 6.5, the impulse response of circular tomosynthesis (in the limit of many views) blurs a point-object into a ring. Changing the blurring function to a disk is possible for datasets with many views, as is shown in Fig. 6.6. In addition, the intensity of the disk falls off faster than the ring, as the reconstruction plane moves away from the object. As the reconstruction becomes view starved, the range over which the filtering produces a uniform disk blur becomes limited. As shown in Figs. 6.9 and 6.11, the uniformity of the disk is degraded as the reconstructed plane moves away from the object, with the distance over which the blurring is uniform becoming smaller as the number of views is decreased. The interior area of the blurring function still behaves like a disk. While the area near the edge of the disk is not smooth in view-starved conditions, it is comparable to that for unfiltered backprojection. A larger number of views yields a more homogeneous blurring, as in the case of unfiltered reconstruction, but even in view-starved conditions, the filtering improves the blurring of objects close to the reconstructed plane without increasing the conspicuity of objects farther away.

The blurring of complex objects away from the focal plane is improved using the disk filter, as demonstrated in Fig. 6.13. Even with only 20 views, Fig. 6.14 shows that the disk-filtering improves the blurring of out-of-plane objects in the lung. A more homogeneous blurring, even of only the planes closest to the plane of interest, helps make the signal from neighboring objects less structured and improves the visualization of objects that lie in the focal plane. This improvement is accompanied by a small decrease in SNR. The SNR on focal plane using the disk filter is $\approx$85-90% of that for circular tomosynthesis with unfiltered backprojection. This SNR penalty may be quite acceptable.

While the filter was derived assuming parallel rays, simulations (and experiments) were performed assuming the more realistic case of non-parallel rays. From a comparison with simulations for parallel rays, we have found that this has little effect on objects near the origin. Objects away from the origin imaged with a divergent beam and reconstructed using this filter have slightly skewed disk profiles, but still improved blurring. Thus, application of the parallel-beam filter to non-parallel ray projections seems to be acceptable, although further work in this area may be warranted.

It is beneficial to once more examine the Fourier space analysis of tomosynthesis, and the application of filtering to improve image quality. Circular tomosynthesis cannot produce a perfect reconstruction of an object, because only a subset of Fourier space is sampled. In addition, the region that is sampled is not sampled uniformly. This results in non uniform weighting when simple backprojection is used for image reconstruction. This weighting, however, can be altered using filtering. One might expect that an appropriate filter choice would make these weightings more even. Indeed, the conventional CT ramp filter, which can be derived using this same framework, as in Pelc [47], operates by making the weightings uniform. It is interesting to note, however, that the disk blur improves the reconstructed images by making the frequency response even less uniform. The filter to generate a disk blur acts like the combination of many circular tomosynthesis datasets with decreasing tomographic angle. This combination of many datasets has an even greater non-uniform weighting than a single dataset since many datasets are added which are all oversampled near the origin in Fourier space. The disk filter mimics this, and hence makes the sampling less uniform than prior to filtering. It is not obvious that this would result in improved images from a Fourier space perspective. The criterion used to evaluate the filter here, however, is not frequency response uniformity, but rather the blurring defined by the impulse response of the system.

The fact that the Fourier space weighting is not uniform does not degrade the reconstruction of the focal plane. This can be seen as follows. Assume for simplicity that the focal plane is the central plane of the 3D volume (of real space). The Fourier transform of the focal plane image then is a projection through the 3DFT of the Fourier space data. The projection of the 3D frequency response in the k_z direction is uniform for both unfiltered and disk-filtered backprojection. That is, while the weighting is non-uniform, the projection of the weighting, which produces the focal plane, is uniform. This results in a faithful reconstruction of the focal plane.

Instead of generating the disk filter, Eq. (6.8) could be used directly to produce, from data projected and backprojected with tomographic angle 2θ, images which appear to have been taken with tomographic angle $2\theta_i$. Generating images with smaller tomographic angles may be desirable because of the trade-off between tomographic angle (i.e., slice thickness) and number of views. That is, it is known that tomosynthesis data collected with a smaller tomographic angle has reduced sensitivity to artifacts from an insufficient number of views [6]. Therefore, it interesting to consider whether artifacts due to a limited number of views in data acquired with tomographic angle 2θ can be reduced by filtering the data to mimic tomographic angle $2\theta_i < 2\theta$. The filtering process can only modify the frequency response on the planes in which they are measured; it cannot do anything about the finite angular sampling of the projection data, which generates gaps in the Fourier space coverage. Because of this, filtering using Eq. (6.8) generates images with slice thickness appropriate to the smaller tomographic angle, but artifacts due to the limited number of views consistent with the larger tomographic angle. This was verified experimentally. Therefore, this filter cannot be used to retrospectively select a smaller tomographic angle when the tomosynthesis images show a need for a larger number of views. This ring-to-ring filter can be used to generate images which mimic another tomographic angle, but only if the original data has an adequate number of views. This is analogous to the performance of the disk filter, which produces reconstructed images with artifacts from a limited number of views if the original data does.

6.7 Conclusions

We have developed the framework for generating a filter to alter the appearance of off-focal plane point-objects in circular tomosynthesis, specifically, to blur out-of-plane objects into a disk rather than a ring. The performance of this filter has been verified using computer simulations. Analytical predictions and simulations show that use of the filter results in a small loss in SNR. Simulations suggest that the technique works very well when applied to datasets with a large number of views. In circular tomosynthesis data with a more typical small number of views, the range over which the filtering yields a uniform disk is reduced, but the remaining discrete impulse response seems no worse than in unfiltered backprojection. Experimental results on a clinically relevant phantom suggest that the technique is potentially beneficial even for datasets without a large number of views.

Chapter 7

Clinical Applications

The ultimate goal of this research is the application of circular tomosynthesis to medical imaging. It is expected that tomosynthesis will not replace radiography or computed tomography as a general imaging tool. Rather, specific imaging requirements which are not currently being met adequately will provide the driving force. The possibilities for tomosynthesis include a number of imaging tasks. Previous studies explored its use in mammography [22, 23], dental imaging [6, 24], angiography [25, 49], and the detection of lung nodules [26]. In this chapter, we focus on the potential application of tomosynthesis to mammography and imaging of the upper cervical spine. These two applications were suggested by clinical colleagues because of the large potential health benefit from improvement in image quality, and because of the suboptimal conventional imaging techniques used in these areas. Experimental results discussed in this chapter for phantoms for these two fields demonstrate the potential usefulness of tomosynthesis in the clinical environment.

While the imaging experiments in this chapter are performed in-vitro, and mostly with phantoms, they do provide an example of the type of imaging performance that is possible with tomosynthesis. The goal is not to demonstrate positive proof of improvement in the clinical environment, which is beyond the scope of this thesis, but rather to suggest potential clinical applications for the tools developed in the previous chapters.

7.1 Mammography

7.1.1 Introduction

The potential health benefit resulting from improvements in breast cancer screening and diagnosis is enormous. Breast cancer is responsible for the largest group of new cancer patients in women [50], affecting approximately one out of ten women in the United States and Western Europe [51]. It is the number two cause for cancer-related deaths in women, second only to lung cancer [50]. Almost one million new patients are expected to suffer from breast cancer in the year 2000, with 420,000 deaths in the same year [52]. In the United States alone, there were an estimated 178,700 new cancer cases in 1998, with 43,400 deaths [50]. Given these staggering figures, considerable effort is undertaken to attempt to detect and treat breast cancer.

Mammography is used both for screening and diagnosing breast cancer, with the American Cancer Society and the National Cancer Institute recommending annual screening mammograms for asymptomatic women aged 40 and over [53]. This has resulted in a reduction in the number of deaths due to breast cancer [54]. Not all cancers are detected, however, as approximately 30% of cancers are missed by mammography [55, 56]. The cancers which are missed tend to be in radiographically dense breasts with overlying structures [56, 57], which suggests that a method for removing overlying structures would be beneficial in finding these cancers. Additionally, calcifications seen on mammograms can be classified as suspected benign or malignant based on their location and spatial distribution [58, 59]. Therefore, information on the 3D spatial extent of calcification clusters could aid in determining which should be the cause for alarm.

Projection radiography is an imperfect type of imaging, in that it gives no depth information. This makes it both difficult to discern objects due to overlying structures, and difficult to determine where the visible objects lie in the breast. Computed tomography could potentially be used to give the 3D information lacking in mammography, but this is difficult because of the tight anatomical restrictions on the imaging geometry. Because of the low contrast of the structures in the breast, x-ray paths which must pass through the torso are sub-optimal, and result in patient dose to areas not being evaluated. Additionally, the in-plane spatial resolution of conventional CT machines is well below that used in mammography. This is particularly crucial in mammography, where the small size of the objects of interest dictate a need for high spatial resolution. In addition, because of the large screening population, cost of the exam (and hence the equipment) must be kept low in order to make the screening economically viable. While projection radiography is relatively inexpensive, the same cannot be said for CT. The high in-plane spatial resolution, flexible imaging geometry, potential low cost, and limited 3D information available in tomosynthesis may be beneficial as an imaging compromise between the potential benefits of projection radiography and computed tomography. The high in-plane resolution allows the examination of small features, while the imaging geometry can be adjusted to conform to the anatomical needs and still provide some depth information.

7.1.2 Phantom Experiments

In order to evaluate typical mammographic imaging tasks, we have imaged the American College of Radiology (ACR) Mammography Quality Control phantom (Fig. 7.1). The attenuation of this phantom is equivalent to a 4.2 cm thick compressed breast consisting of 50% glandular and 50% adipose tissue. Contained in the phantom are fibers (1.56, 1.12, 0.89, 0.75, 0.54, and 0.40 mm diameters), specks (i.e. calcifications) (0.54, 0.40, 0.32, 0.24, and 0.16 mm diameters), and masses (2.00, 1.00, 0.75, 0.50, and 0.25 mm thicknesses and decreasing radii) [60]. This phantom, which is used by hospitals in order to evaluate their mammography systems, can be used to compare the application of tomosynthesis in mammography to conventional radiography. We used the ACR phantom to evaluate the ability of tomosynthesis to determine the 3D location of a calcification, and to produce images which have effectively removed overlying structures that obscure the viewing of the low contrast masses and fibers.

In addition to the objects inside the ACR phantom, there is a very high contrast disk (not shown in Fig. 7.1) attached to the top surface of the phantom. This disk, which is used in mammography clinics to determine film contrast, appears as a bright white disk in all of the images. This is acceptable here, since it does not obscure

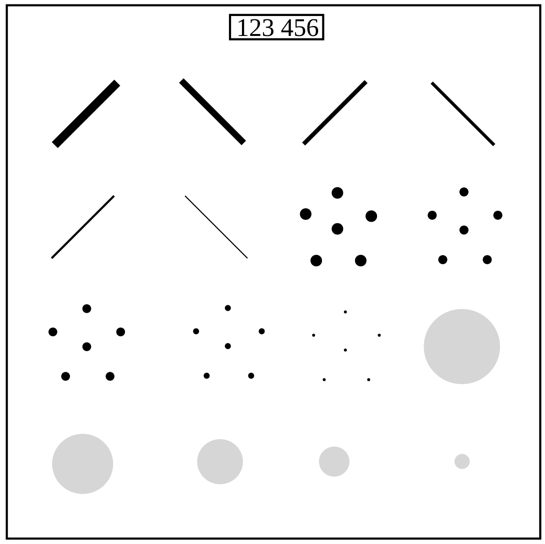

Figure 7.1: Schematic of the ACR Mammography Quality Control phantom, which contains fibers, specks, and masses.

any of the objects which we are interested in viewing. Moreover, this high contrast disk is not indicative of clinically-relevant imaging conditions, and the presence of artifacts in the reconstructed images from this disk should not negatively reflect on the system.

3D Calcification Localization

Circular tomosynthesis datasets of the ACR phantom were collected using the volumetric tomography system with tomographic angles 20° and 50°. Because all of the objects in the phantom are located in approximately the same plane, the phantom was tilted by approximately 20° during image acquisition. This allows reconstructions planes parallel to the stage axis to focus on one calcification, while neighboring calcifications are blurred (because they lie on different planes). The relative blurring of the off-plane calcifications is indicative of the ability to resolve the 3D location of a calcification in breast tissue. Alternatively, a more general image reconstruction scheme could be used to focus on an arbitrary surface, i.e., not a plane which is normal to the axis of rotation of the positioning stage [61]. We have developed a general backprojection reconstruction algorithm based on the work in Ch. 2, which we used to reconstruct an oblique plane through the objects in the tilted phantom. This further demonstrates the flexibility of tomosynthesis, in which the focal plane can be selected retrospectively.

Each dataset contained 100 projection images. In addition, the data were subsampled in order to reconstruct tomosynthesis images resulting from 10 and 20 views. An x-ray technique of 40 kVp and 160 mA, was used, with a 200 ms exposure time. The selection of this technique was limited by the x-ray tube and generator capabilities of the volumetric tomography system, as is discussed below. In order to compare tomosynthesis with radiography at equivalent SNR, 100 radiographic images of the ACR phantom were collected using the same x-ray technique. The tomosynthesis images were reconstructed using both unfiltered backprojection, and filtered backprojection using the disk filter derived in Ch. 6.

Removal of Overlying Structures

The ability to visualize suspicious objects in a mammogram is limited not only by SNR, but also by the superposition of other objects with similar or greater contrast which lie along the direction of the x-ray beam. In order to demonstrate the ability of tomosynthesis to remove overlying structures (or at least blur them enough to effectively remove them), images were acquired of the ACR phantom covered with a layer of structured beeswax. The beeswax, which has been molded into a sheet with a 3D honeycomb-like shape, was placed approximately 1 cm above the plane containing the objects in the ACR phantom (Fig. 7.2). The honeycomb structure of the beeswax, while not anatomically realistic, provides an imaging task analogous to that which arises in mammography when interfering structures are present in breast tissue. Circular tomosynthesis datasets were acquired with tomographic angles 20° and 50°. Each dataset contained 100 projection images, and the data were subsampled to reconstruct tomosynthesis images with 10, 20, and 100 views. An x-ray technique of 40 kVp, 160 mA, was used, with a 200 ms exposure time. One hundred radiographic images of the ACR phantom were collected using the same x-ray technique (Fig. 7.3). The tomosynthesis images were reconstructed using both unfiltered backprojection and filtered backprojection using the disk filter.

Figure 7.2: The ACR Mammography phantom covered with a layer of [structured] beeswax used to simulate structured overlying objects.

7.1.3 In-Vitro Tissue Imaging

In order to demonstrate the benefit of the 3D localization of objects and the removal of overlying structures with a more biologically relevant object, a mastectomy sample was imaged using the volumetric tomography system. This experiment was approved by Stanford University's Institutional Review Board (IRB). The fresh sample was imaged shortly after the surgical procedure, and prior to the pathology workup. A 50° tomographic angle was used for the tomosynthesis dataset, with 100 projection images. As before, the data were subsampled to reconstruct tomosynthesis images with 10, 20, and 100 views. An x-ray technique of 40 kVp, 160 mA, was used, with a 200 ms exposure time per view. Because of the limited time allowed for handling the sample prior to transfer to the Pathology Department, only 10 radiographic images were collected for comparison with the tomosynthesis images, and no additional tomosynthesis datasets could be collected. The tomosynthesis images were reconstructed using both unfiltered backprojection, and filtered backprojection using the disk filter.

Because of the high contrast in the tissue sample, and the resulting large dynamic range required to display the images, both the radiographic and tomosynthesis

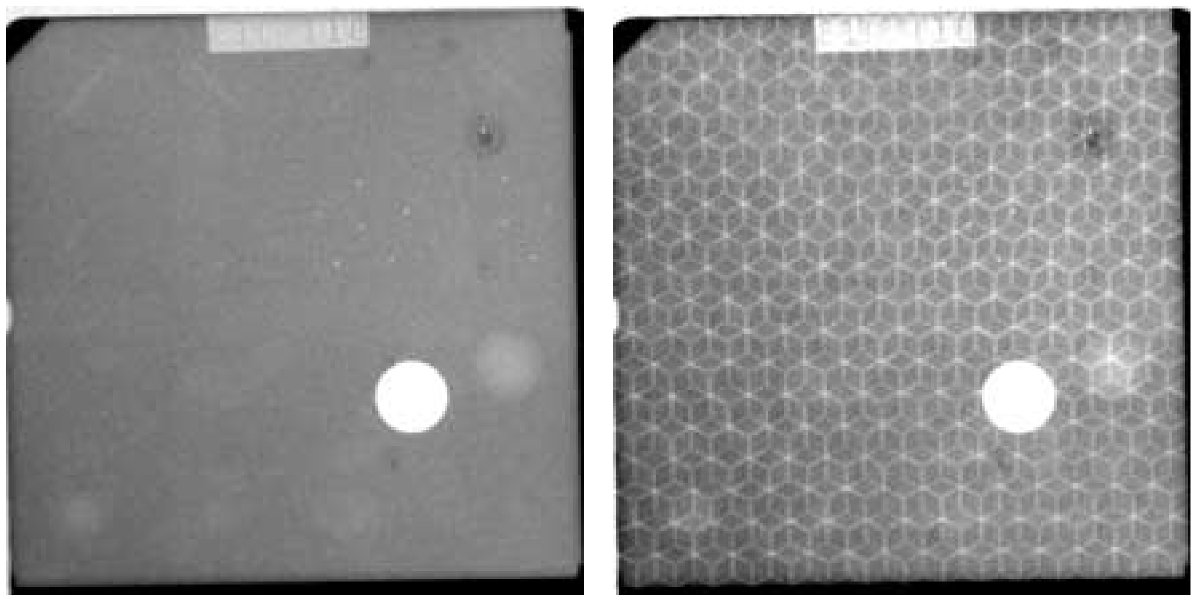

(a) Phantom alone

(b) Phantom with wax

Figure 7.3: Radiograph of the ACR Mammography phantom (a) alone and (b) with a layer of beeswax.

images were filtered using unsharp masking. This filtering was performed by subtracting 75% of the pixel intensities in a smoothed image from the original radiographic/reconstructed image. The smoothed image was generated using a 201x201 pixel Gaussian kernel, with a 52 pixel full-width at half maximum.

7.1.4 Results

3D Calcification Localization

As shown in Fig. 7.4, a radiograph of the tilted ACR phantom contains no depth information. In contrast, the tomosynthesis images of the tilted phantom, Figs. 7.5 - 7.7, clearly depict the 3D distribution of the calcifications. For each plane, a subset of the calcifications are in focus, and appear sharp, while the off-plane calcifications are blurred into rings. Additionally, the tomosynthesis data were reconstructed on an oblique plane (Fig. 7.8) which passes through all of the calcifications in the group.

Figure 7.4: Radiograph of the largest group of calcifications in the tilted ACR Mammography phantom.

The angle of the oblique plane which best focused on all of the calcifications matched well with the physical angle of the tilted phantom.

The effect on tomosynthesis images of reducing the number of views is to discretize the blurring function. This makes the blurred objects more visible by decreasing the area over which the object intensity is spread, and by increasing their high frequency content. This is difficult to gauge in this setting, however, because of the noise content in the low-contrast images and close proximity of the small calcifications. The noise level and the low contrast make it difficult to see the effects of the discrete off-plane artifacts from a limited number of views. The close proximity of the calcifications results in blurred off-plane reconstructions of rings with small radii. This makes it difficult to see the discrete nature of the blurring, which is more apparent as the ring radius increases. Therefore, one should be careful in assuming that these results imply that mammographic tomosynthesis requires only a small number of views. This is difficult to determine with this imaging phantom. The effect of a limited number of views on the 3D localization of calcifications would be more apparent in a phantom with calcifications more homogeneously distributed, and with more complex structure.

The effect of a smaller tomographic angle is to increase the slice thickness, because of the reduction of the sampled frequency bandwidth in the slice direction. Because of this, a larger volume of the object is effectively in focus for each plane. Calcifications separated in height by a smaller amount than this slice thickness appear to lie in approximately the same plane. As demonstrated in Fig. 7.6, the smaller tomographic

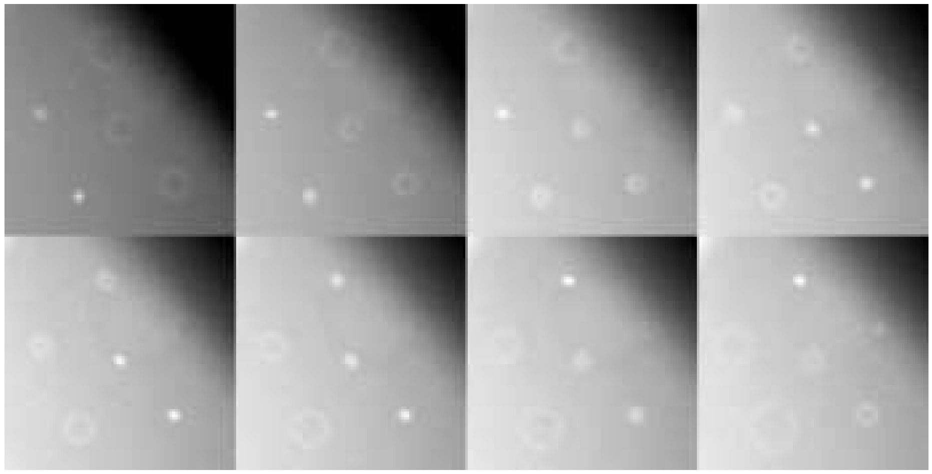

Figure 7.5: Tomosynthesis images (50° tomographic angle, 100 views, and unfiltered backprojection) of a calcification group in the tilted ACR Mammography phantom. Each view is separated from its neighbor (left to right, and top to bottom) by 1 mm.

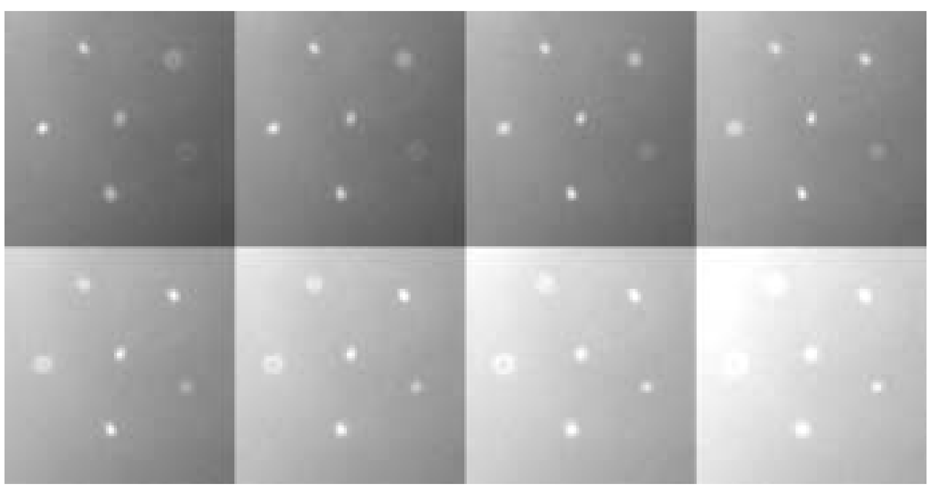

Figure 7.6: Tomosynthesis images (20° tomographic angle, 100 views, and unfiltered backprojection) of a calcification group in the tilted ACR Mammography phantom. Each view is separated from its neighbor (left to right, and top to bottom) by 1 mm. Note that the phantom was positioned somewhat rotated relative to Fig. 7.5.

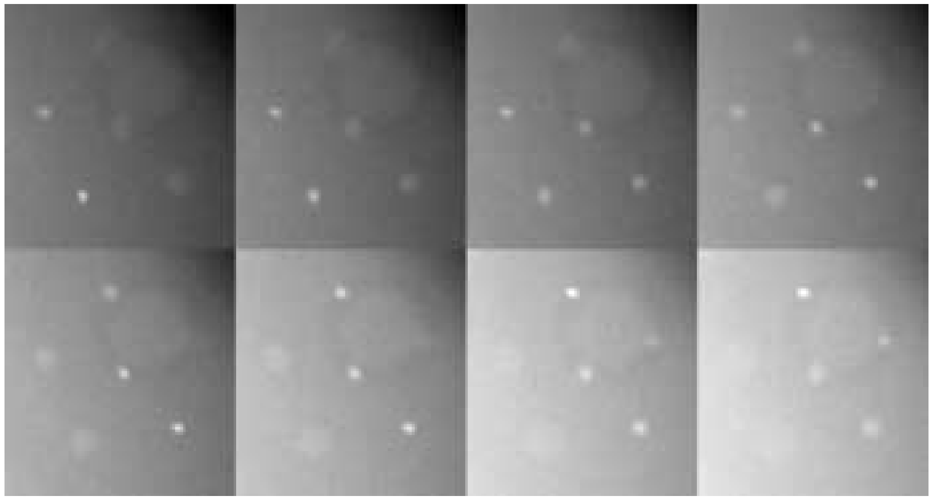

Figure 7.7: Tomosynthesis images (50° tomographic angle, 100 views, and disk-filtered backprojection) of a calcification group in the tilted ACR Mammography phantom. Each view is separated from its neighbor (left to right, and top to bottom) by 1 mm.

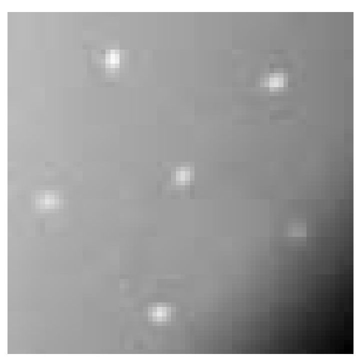

Figure 7.8: Tomosynthesis images (50° tomographic angle, 100 views, and unfiltered backprojection) along the oblique plane which contains all of the calcifications in the tilted phantom.

angle decreases the ability to resolve the 3D location of the calcifications.

The use of the disk filter, Fig. 7.7, is only a slight improvement over the unfiltered backprojection images in this simplified case. Because of the small blur radius for the calcifications which are in close proximity, unfiltered backprojection produces rings which have relatively small radii. These rings have small openings, which is where the disk filter can place part of the blurred intensity. One main contribution of the disk filter is to improve the suppression of superimposed structures, which this experiment is not equipped to examine. The performance of the disk filter to mammographic tomosynthesis would be better tested with calcifications which were more distantly located, or with more overlying structures.

Removal of Overlying Structures

The addition of a layer of structured beeswax to the ACR Mammography phantom makes it difficult to discern the objects in a radiograph of the phantom (Fig. 7.3(b)), especially the fibers and masses. While trained observers may still pick up many of the objects under ideal viewing conditions, it is clear that the diagnosis is complicated by the superimposed structures. The use of circular tomosynthesis, with the same total dose as the radiograph, improves the visualization task by blurring the overlying structures. Tomosynthesis with tomographic angle 50° and 100 views, Fig. 7.9, greatly reduces the impact of off-plane objects. This enables better visualization of the fibers and masses in the phantom. In addition, while the higher contrast calcifications are not as easily obscured by the overlying structures in a radiograph as are the masses and fibers, blurring of the superimposed structures may still allow improved visualization of the calcifications.

In more view-starved conditions, the improvement of tomosynthesis becomes less dramatic as the blurring of the overlying structures become more discrete. This causes the wax layer to be less effectively blurred, as in the 20 view case shown in Fig. 7.10. In this case, the overlying structures were approximately 1 cm from the plane of interest. As this distance increases, the number of views required to adequately blur the overlying objects increases. While 20 views is on the limit of being acceptable here, one would predict that a larger number would be required for a 4 cm compressed

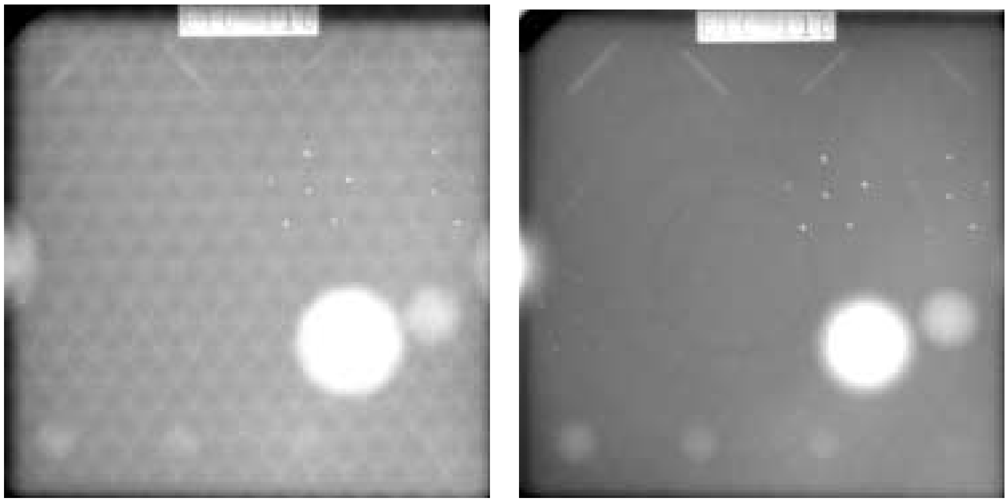

(a) Unfiltered (b) Disk-filtered

Figure 7.9: Tomosynthesis images (50° tomographic angle, 100 views) of the ACR phantom with a layer of beeswax, reconstructed using (a) unfiltered and (b) disk-filtered backprojection.

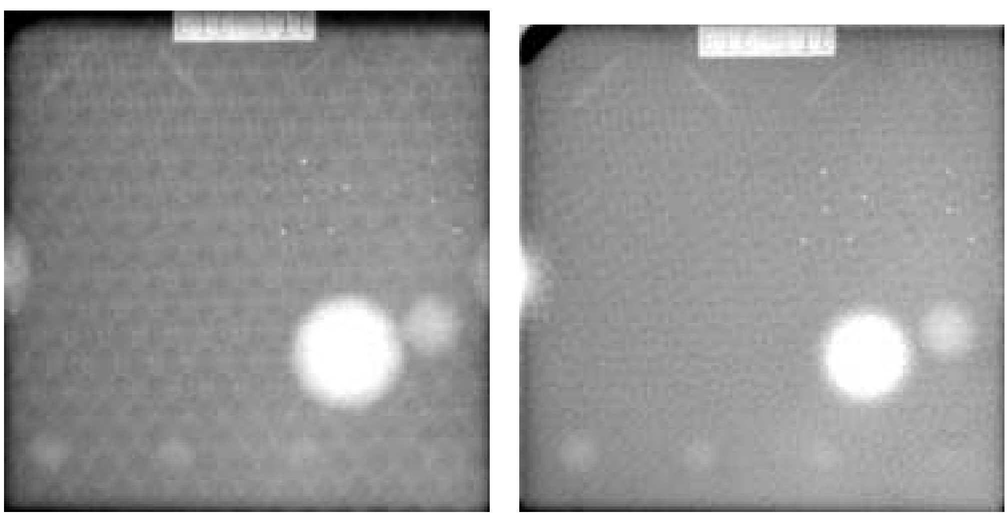

(a) Unfiltered (b) Disk-filtered

Figure 7.10: Tomosynthesis images (50° tomographic angle, 20 views) of the ACR phantom with a layer of beeswax, reconstructed using (a) unfiltered and (b) disk-filtered backprojection.

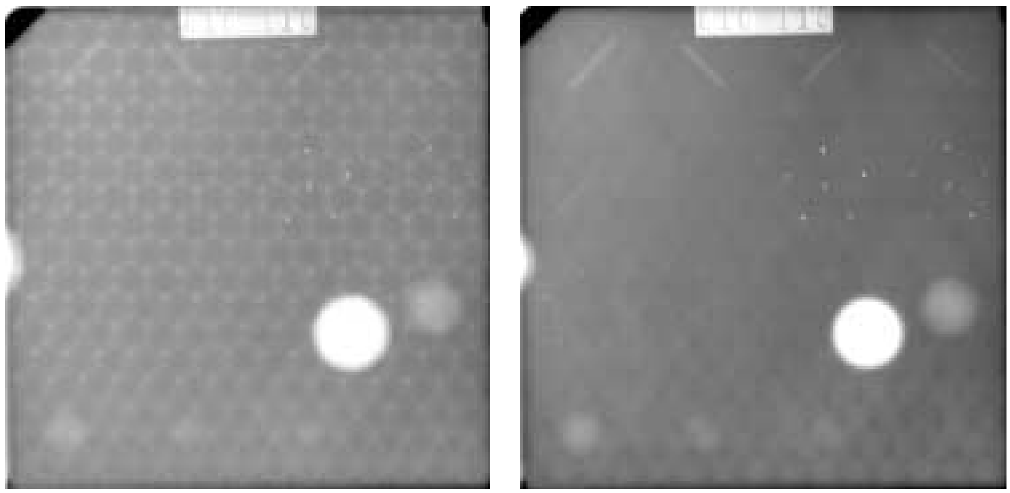

(a) Unfiltered (b) Disk-filtered

Figure 7.11: Tomosynthesis images (20° tomographic angle, 100 views) of the ACR phantom with a layer of beeswax, reconstructed using (a) unfiltered and (b) disk-filtered backprojection.

breast.

As the tomographic angle decreases, the larger slice thickness limits the ability of tomosynthesis to blur out-of-plane objects. In the 20° tomographic angle tomosynthesis images, Fig. 7.11, unfiltered backprojection with 100 views does not perform as well at removing the superimposed structures. The smaller tomographic angle increases the volume which is in focus, and decreases the blur radius of the objects outside this volume. Objects farther away than this (approximately 1 cm in this experiment) will be more effectively blurred.

Filtered backprojection using the disk filter, Fig. 7.9 (b), is very effective in removing the beeswax structure. In the case of 100 views and a 50° tomographic angle, the filtered image shows little sign of the wax layer. It appears that in more view-starved conditions, the the volume over which the disk filter is able to blur out-of-plane objects better than unfiltered backprojection is reduced. This is evident when comparing Fig. 7.10 (20 views) with Fig. 7.9 (100 views). In addition, the disk filter makes use of smaller tomographic angles more feasible by improving the

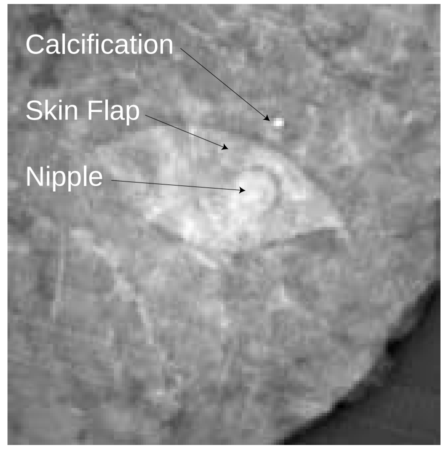

Figure 7.12: Radiograph of a fresh mastectomy sample. This image has been filtered (after reconstruction) using unsharp masking.

blurring of out-of-plane objects close to the focal plane.

In-Vitro Tissue Imaging

The difficulty of discerning structures in a radiographic image of the breast, due to the presence of the overlying structures, is evident in a radiograph of the mastectomy sample (Fig. 7.12). This is made worse because the fresh tissue sample was covered in a towel during the imaging process. The towel is evident in this image as an angled band across the bottom of the image and an interlaced pattern over the rest of the image.

As in the case of the phantom experiments, use of tomosynthesis improves visualization of the tissue sample by blurring the overlying structures. Figure 7.13 shows a tomosynthesis reconstruction of the mastectomy sample focusing just below the skin flap. The use of the disk filter (Fig. 7.13 (b)) more effectively blurs the out-of-plane objects in the tomosynthesis images of this complex object. The skin flap, nipple, and calcification which are present in the radiograph (Fig. 7.12), are effectively removed by the blurring in the disk-filtered tomosynthesis image. This allows better visualization of the volume directly below these objects.

The tomosynthesis images of the mastectomy sample reconstructed with more view-starved conditions behaved in a similar manner to that of the mammography

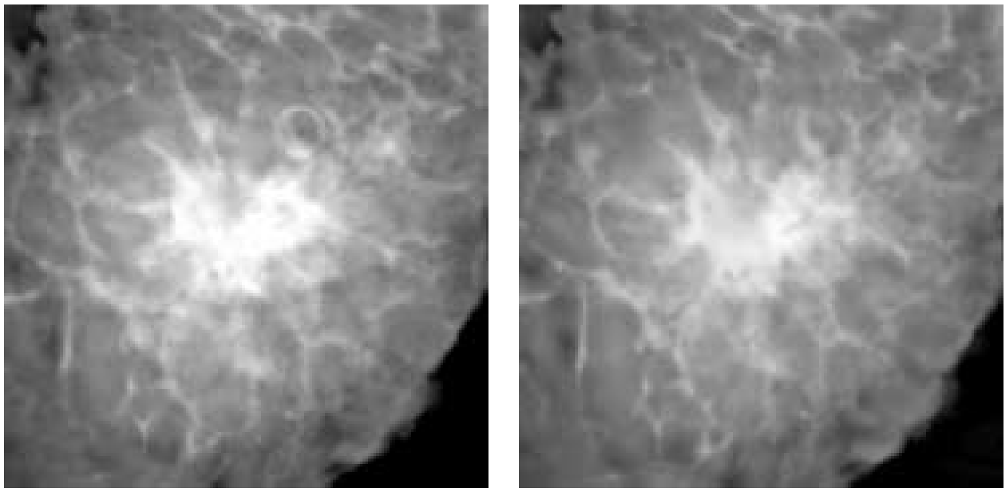

(a) Unfiltered (b) Disk-filtered

Figure 7.13: Tomosynthesis image (50° tomographic angle, 100 views) of the mastectomy sample using (a) unfiltered and (b) disk-filtered backprojection. These images have been filtered (after reconstruction) using unsharp masking.

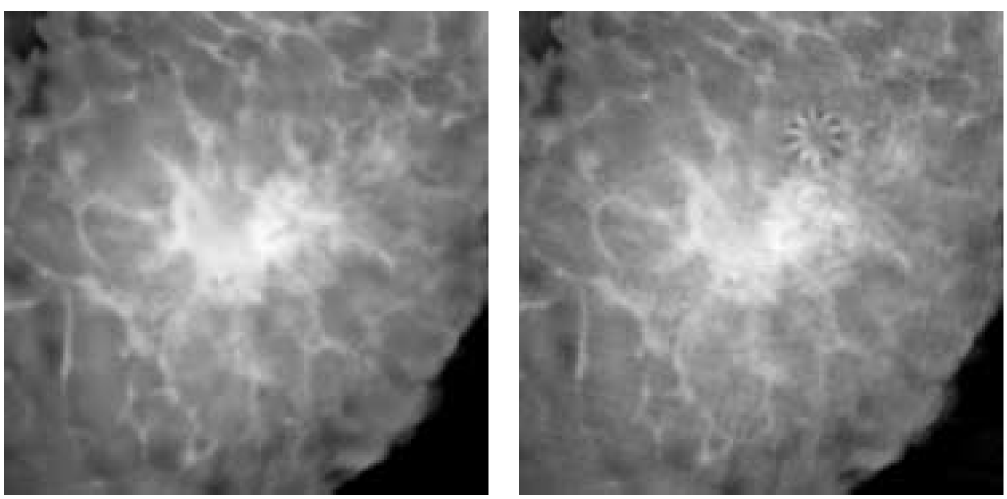

(a) 20 views (b) 10 views

Figure 7.14: Tomosynthesis image (50° tomographic angle) with (a) 20 and (b) 10 views, of the mastectomy sample using disk-filtered backprojection. These images have been filtered (after reconstruction) using unsharp masking.

phantom. As shown in Fig. 7.14 (a), a dataset with 20 views shows some artifacts from an insufficient number of views for a 50° tomographic angle, with the large calcification being blurred into discrete points. This is more evident in Fig. 7.14 (b), for the case of only 10 views. In addition, the skin flap is less adequately blurred in the case of 20 views, and is quite visible in the case of 10 views. Even so, the region below the skin flip can be seen nicely in the 20 view image. The blurring is quite poor in the case of 10 views, where the structure from the towel can be seen in the tomosynthesis image. This suggest that for a 50° tomographic angle, 20 views is close to the minimum number required to adequately image this amount of breast tissue. For in-vivo analysis, where the amount of breast tissue will be larger, this number may need to be higher accordingly.

7.1.5 Discussion

Tomographic images of the ACR phantom taken with the volumetric tomography system should be evaluated relative to radiographic images from the same system rather than by comparison to a state-of-the-art mammography system. This is important because our tomography system is not designed to perform under mammographic conditions for two main reasons. First, the x-ray tube and generator are not designed to operate at the low voltages which are required to give optimal contrast in mammographic applications. Typical mammography-specific x-ray tubes operate with a peak voltage around 28 kV, using molybdenum or rhodium targets and filters [14,19]. Mammography-specific equipment is used because the inherent contrast in breast tissue is very low, and the image contrast is maximized at low x-ray energies. On the volumetric tomography system, the lowest peak voltage is 40 kV. In addition, the tube and collimator have at least 2.5 mm aluminum equivalent filtration at 80 kV [62]. X-ray beam simulations show that this results in an x-ray beam with average energy of approximately 27 keV (compared to < 20 keV for a mammography system), and more importantly, all x-rays with energies less than 20 keV have effectively been removed by the inherent filtration. These simulations also suggest that additional k-edge filtration could do little to lower the average beam energy, because of the loss of the low energy x-rays by the inherent filtration. Second, conventional film-screen systems have spatial resolution up to 20 lp/mm (i.e., 25 μm pixels), although the contrast and SNR of mammographic imaging do not allow the full utilization of this resolution [19]. Current digital detectors aimed for mammographic applications have pixels on the order of 50 - 100 μm [14, 19], but the prototype detector in the volumetric tomography system has 200 μm pixels. This decreased spatial resolution could be apparent when viewing the smallest calcifications on this system compared with a mammography system. While the system is not optimized for mammographic applications, however, the relative performance of tomosynthesis demonstrates the fundamental improvements over projection radiography in mammography. Application of the same imaging techniques on mammography-specific equipment should improve the image quality in a similar manner, without affecting the relative quality between tomosynthesis and radiography.

In order to demonstrate that the benefit of tomosynthesis to mammographic applications is due to the fundamental imaging properties of radiography and tomosynthesis, rather than the limitations of the volumetric tomography system, radiographic images of the ACR Mammography phantom were collected on a mammography x-ray system. Radiographs were collected on a GE 600T system (GE Medical Systems, Milwaukee, WI), which has a molybdenum target and filter and a 0.3 mm focal spot. A standard imaging technique of 26 kVp and 100 mA was used. Exposure times were approximately 1.0 s for the radiographs of the ACR phantom with and without a layer of structured beeswax, and 2.2 s for the radiograph with the phantom tilted by approximately 20°. Figures 7.15 and 7.16 show radiographs of the ACR phantom with and without a layer of beeswax, respectively. These figures demonstrate that the degradation of images by overlying structures is fundamental to projection radiography, and not due to the suboptimal imaging conditions of our system. In addition, Fig. 7.17 confirms that a radiograph of the tilted phantom lacks the ability to derive any depth information, regardless of the detector pixel size or x-ray beam energy. Thus, the improvements in the tomosynthesis images on the volumetric tomography system compared to radiographic images from the same system do not arise because the starting point is a non-optimal imaging condition. Instead, the improvements are

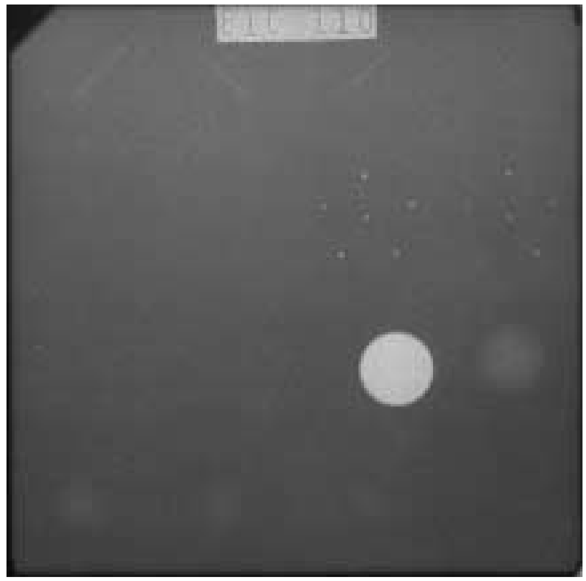

Figure 7.15: Radiograph of the ACR phantom, using an analog, mammography-specific x-ray imaging system.

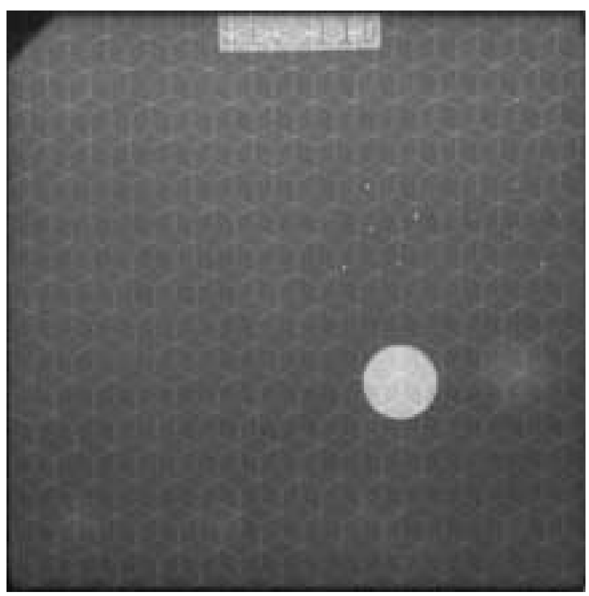

Figure 7.16: Radiograph of the ACR phantom with a layer of beeswax, using an analog, mammography-specific x-ray imaging system.

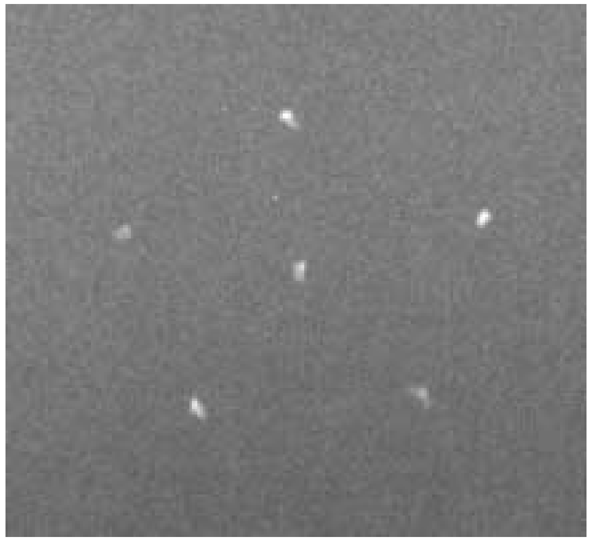

Figure 7.17: Radiograph of the tilted ACR Mammography phantom using an analog, mammography-specific x-ray imaging system.

the result of the fundamental way in which 3D information is handled in radiographic and tomosynthesis imaging. The relative performance of the volumetric system can be expected to transfer to task-specific hardware since the underlying limitations are the same.

As noted above, a smaller tomographic angle increases the slice thickness of the reconstructed image. This limits the ability of tomosynthesis to blur nearby out-of-plane objects, and decreases the ability to both visualize objects and resolve their 3D location. It should be noted, however, that at times it may be desirable to operate with lower tomographic angles. In addition to the imaging conditions which dictate small tomographic angles, e.g. when the human anatomy requires it, a smaller tomographic angle is beneficial in view-starved conditions. The smaller blur radius of out-of-plane objects relative to the blur radius for a larger tomographic angle reduces the discrete nature of the blurring. This lessens the chance of interpreting the discrete blurred objects as additional on-plane objects, and improves the visualization on objects on the focal plane.

The application of the disk filter appears quite promising in terms of removal of overlying structures in mammographic applications. It should be noted, however, that the use of this filter is predicated on the assumption that a disk-shaped blur is superior to a ring-shaped blur. In order for this to be true, low intensity rings in an object (which arise from small objects) must be more detrimental than even lower intensity disks. This might not be the case in mammography, where the disks resulting from the blurring of small objects may be interpreted as masses which are in focus. This could result in false positive findings from artifacts introduced by the tomosynthesis imaging process. If this were the case, the techniques developed in Ch. 6 could be used to generate a filter with a more optimal impulse response for this specific imaging task, i.e., a filter which blurs objects into shapes which are not reminiscent of any image targets. In addition, paging through reconstructions of multiple planes could reduce the confusion regarding suspicious objects in a tomosynthesis image.

7.2 Cervical Spine Imaging

7.2.1 Introduction

Imaging of the upper cervical spine represents another area in which tomosynthesis could potentially improve upon conventional imaging techniques. This is important, because more than 10,000 new spinal cord injuries happen each year in the United States alone, with an annual direct cost of approximately \$5-\$8 billion [63–65]. In addition to this, approximately 400,000 patients (extrapolating from study results in [66]) are admitted to trauma centers in the US per year, giving a large population for potential radiographic screening. It is estimated that 2% - 3% of the trauma patients have cervical spine injuries [67]. However, because of the dire consequences for missed injuries, virtually all patients in the U.S. admitted with major trauma or injuries above the shoulders undergo evaluation for potential spine trauma [68, 69]. Ignoring the question of whether or not this is over-aggressive screening, a large population of patients exists which could benefit from improved imaging techniques.

For patients admitted with cervical spine trauma symptoms, the American College of Radiology currently recommends three views for radiographic screening: anteoposterior (A-P), lateral, and open-mouth A-P [70]. While not all trauma centers do this, many articles in the literature accept these views as the minimum first level of screening for trauma patients [67, 71–75]. Historically, motion tomography was used as a followup to radiographic screening for further imaging [76–79], but CT is taking over this role (with the exceptions noted below) [67, 69, 72–74, 80, 81].

This chain of events is predicated on being able initially to obtain a high quality set of radiographs. The open-mouth view is needed because the jaw structures are superimposed over the top vertebrae in standard A-P images. Imaging C-1 and C-2 through the open jaw attempts to limit the impact of overlying objects. However, the highest-risk patients are often intubated (adding additional overlying structures which may not be able to be moved out of the desired field of view) or unable to comply with the imaging requirements due to their injuries, and therefore difficult to image with the open-mouth view [79, 82]. In fact, the most common location of missed fractures at the radiographic screening stage is at the C-1 to C-2 level [83, 84]. Conventional tomography [85, 86] and computed tomography [82, 83, 87] have been used to replace the open-mouth view for such patients. Conventional tomography, and hence tomosynthesis, may be preferable since approximately 10% of cervical spine fractures are located at the dens [88, 89], for which CT is inferior to conventional tomography [74, 79, 80, 84, 90]. Many of the fractures lie in the axial plane, which can be missed by CT. Our goal is to use tomosynthesis to replace the open-mouth A-P view by blurring the overlying structures for patients unable to provide an adequate radiographic image. In addition, there are other roles that tomosynthesis may inherit from motion tomography in imaging the cervical spine, where CT does not perform as well due to the limitations on imaging geometry or lower in-plane spatial resolution [72, 74, 78, 90]. We limit discussion here to the replacement of the open-mouth A-P view with tomosynthesis.

7.2.2 Phantom Experiments

In order to examine the potential usefulness of tomosynthesis in replacing the open-mouth A-P view, we have performed experiments with a head phantom (Radiology Support Devices, Long Beach, California). This anthropomorphic phantom consists of plastic-encased, bone-equivalent plastic in the shape of the skull and cervical spine. The mouth of the phantom cannot be manipulated to mimic an open-mouth view, as is discussed below. Circular tomosynthesis datasets of the head phantom were collected using the volumetric tomography system with 10°, 20°, and 50° tomographic angles. Each dataset contained 100 projection images. Additionally, the datasets were subsampled to reconstruct tomosynthesis images with 20 and 50 views. An x-ray technique of 80 kVp and 160 mA was used, with an 80 ms exposure time per view. In order to compare tomosynthesis with radiography at equivalent SNR, 100 radiographic images of the head phantom were collected using the same x-ray technique. The tomosynthesis images were reconstructed using both unfiltered backprojection and filtered backprojection using the disk filter.

Because of the high contrast differences in the phantom, and the resulting large dynamic range required to display the images, both the radiographic and tomosynthesis images were filtered using unsharp masking. This filtering was performed by subtracting 75% of the pixel intensities in a smoothed image from the original radiographic/reconstructed image. The smoothed image was generated using a 201x201 pixel Gaussian kernel, with a 52 pixel full-width at half maximum.

7.2.3 Results

The entire cervical spine is clearly depicted in a lateral view radiograph of the head phantom, as is shown in Fig. 7.18. An A-P view of the phantom, however, does not adequately display the upper cervical spine. As shown in Fig. 7.19, C-1 and C-2 are obscured due to the interference of the overlying jaw structures.

Tomosynthesis images collected with 100 views using a 50° tomographic angle, Fig. 7.20, clearly show these vertebrae. The blurring of the overlying structures is made more uniform with the use of the disk filter. A large number of views are needed to adequately blur the out-of-plane objects because of the complex nature of the overlying objects. If the number of views is not sufficient, artifacts arise (as discussed in Ch. 6). As Fig. 7.21 demonstrates, these artifacts are present for reconstruction of a 50° tomographic angle dataset with 50 views. The appearance

Figure 7.18: A lateral radiograph of the head phantom demonstrates the excellent visualization of the top of the cervical spine in this view.

Figure 7.19: An A-P radiograph of the head phantom depicts the difficulty in visualizing the top of the cervical spine in this view.

(a) Unfiltered (b) Disk-filtered

Figure 7.20: Tomosynthesis images (50° tomographic angle, 100 views) of the head phantom, reconstructed using (a) unfiltered and (b) disk-filtered backprojection. These images have been filtered (after reconstruction) using unsharp masking.

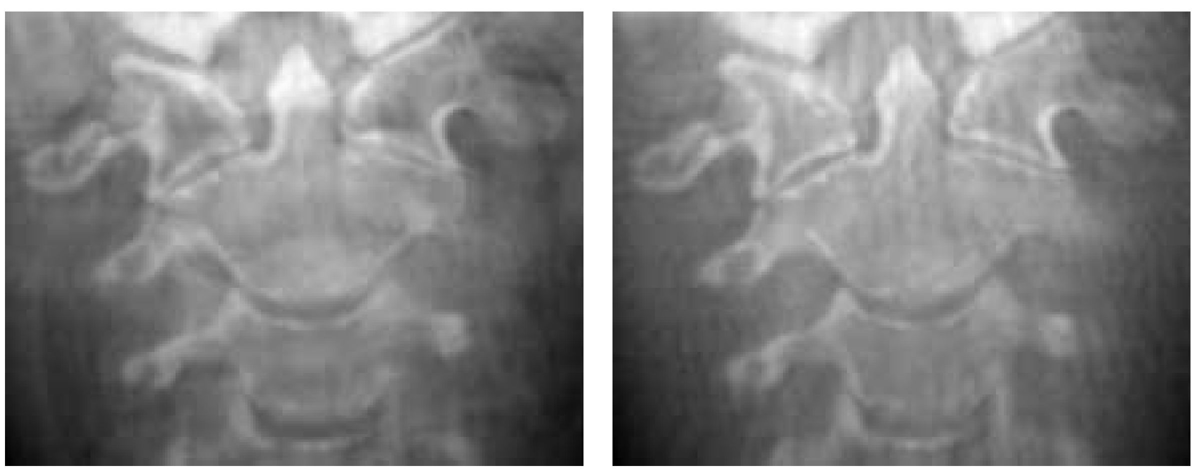

(a) Unfiltered (b) Disk-filtered

Figure 7.21: Tomosynthesis images (50° tomographic angle, 50 views) of the head phantom, reconstructed using (a) unfiltered and (b) disk-filtered backprojection. These images have been filtered (after reconstruction) using unsharp masking.

of the artifacts resulting from an inadequate number of views is even more apparent when the number of views is further decreased to 20, as in Fig. 7.22.

In order to allow the number of views necessary to adequately image this region to be decreased, the tomographic angle can be decreased. Figure 7.23 shows a reconstructed plane from a 100 view dataset with a 20° tomographic angle. As for the 50° tomographic angle, 100 view image, C-1 and C-2 are clearly depicted. For this smaller tomographic angle, however, 50 views are sufficient, as shown in Fig. 7.24. This comes at the expense of a larger slice thickness, which reduces the ability to blur out-of-plane objects. This is evident by the loss of some detail in Fig. 7.23 relative to 7.20, but this compromise may be acceptable if the protocol requires a reduction in the number of views. When the number of views is reduced to 20 for a 20° tomographic angle, artifacts arise from the lack of a sufficient number of views.

Again, the drawback of choosing a smaller tomographic angle in order to limit the number of views to adequately image an object is that the slice thickness increases. For complex objects such as the upper cervical spine, too large of a slice thickness limits the ability to separate a slice through the object from the objects lying outside this plane. This is starting to occur for a 20° tomographic angle with the head phantom, which can be seen by comparing Fig. 7.20 with Fig. 7.23. The effect is even more apparent when the tomographic angle is reduced to 10°, as is evident in Fig. 7.26.

7.2.4 Discussion

The motivation for studying the application of tomosynthesis to imaging this anatomic region was to replace the open-mouth A-P radiograph. Because the mouth of the phantom cannot be manipulated, however, an open-mouth view cannot be collected using this phantom. Instead, images are compared with A-P radiographs of the phantom. This is equivalent to the worst-case clinical scenario in which the patient is unwilling or unable to comply with the open-mouth view. This comparison to radiography is most appropriate to a subset of trauma patients, but can be extrapolated to general improvement in the imaging of this anatomic region. Comparisons to

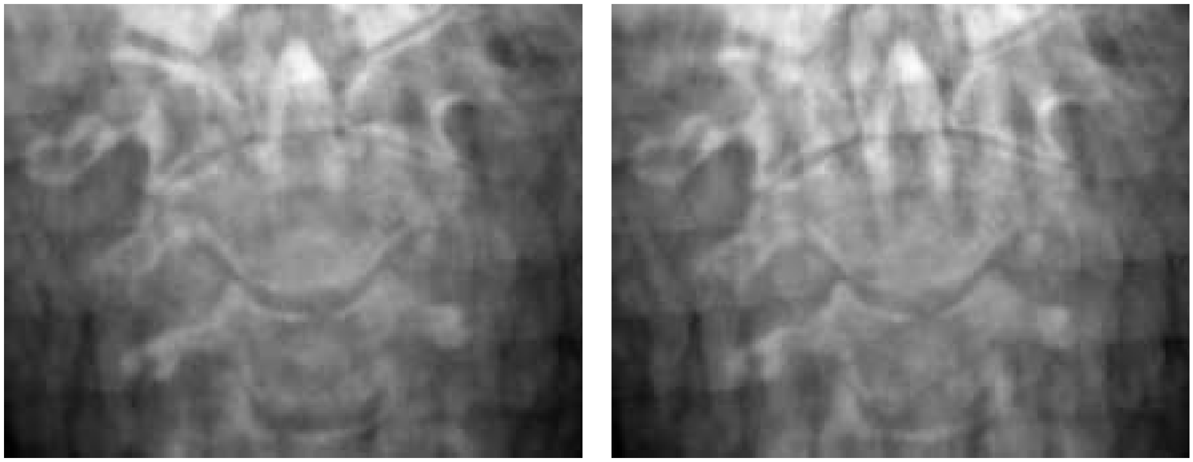

(a) Unfiltered (b) Disk-filtered

Figure 7.22: Tomosynthesis images (50° tomographic angle, 20 views) of the head phantom, reconstructed using (a) unfiltered and (b) disk-filtered backprojection. These images have been filtered (after reconstruction) using unsharp masking.

(a) Unfiltered (b) Disk-filtered

Figure 7.23: Tomosynthesis images (20° tomographic angle, 100 views) of the head phantom, reconstructed using (a) unfiltered and (b) disk-filtered backprojection. These images have been filtered (after reconstruction) using unsharp masking.

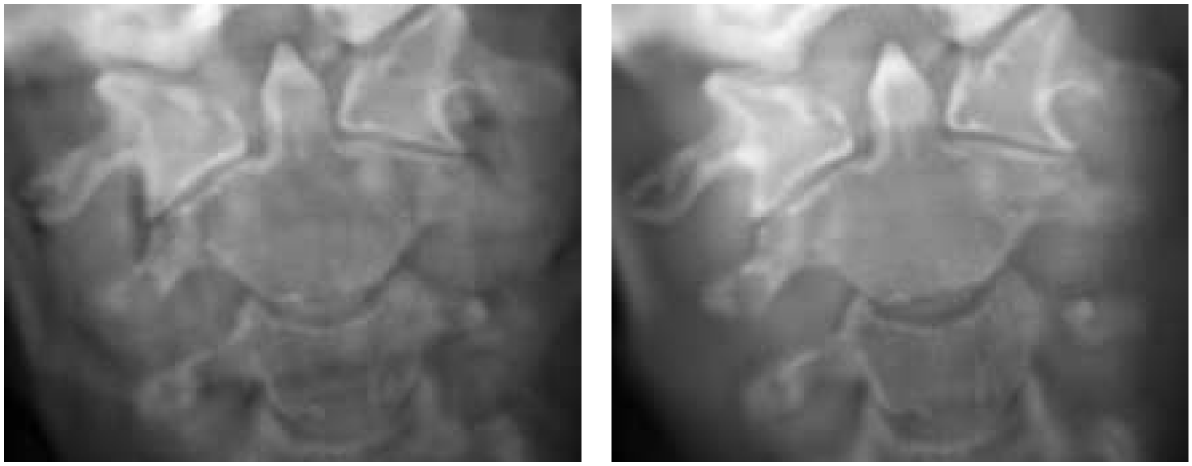

(a) Unfiltered (b) Disk-filtered

Figure 7.24: Tomosynthesis images (20° tomographic angle, 50 views) of the head phantom, reconstructed using (a) unfiltered and (b) disk-filtered backprojection. These images have been filtered (after reconstruction) using unsharp masking.

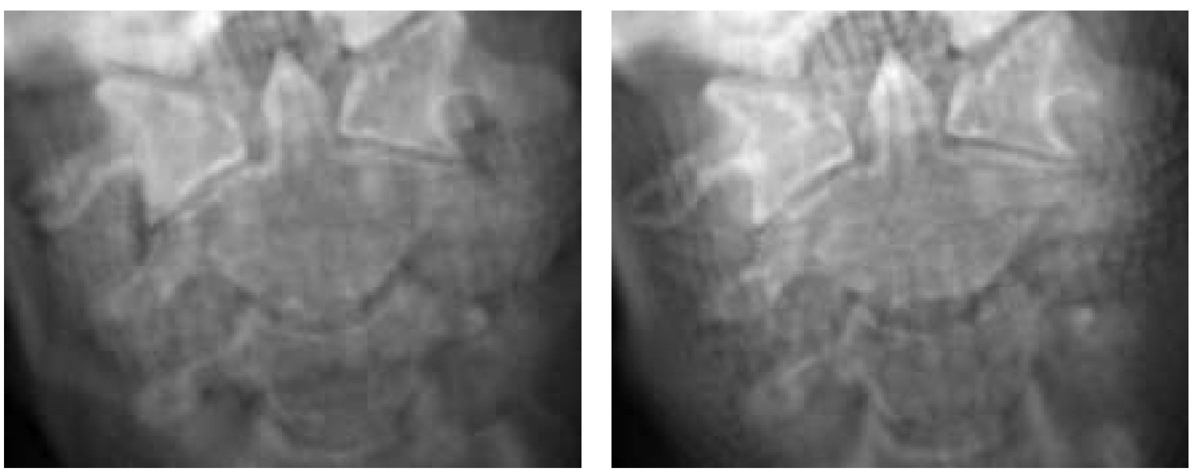

(a) Unfiltered (b) Disk-filtered

Figure 7.25: Tomosynthesis images (20° tomographic angle, 20 views) of the head phantom, reconstructed using (a) unfiltered and (b) disk-filtered backprojection. These images have been filtered (after reconstruction) using unsharp masking.

(a) Unfiltered (b) Disk-filtered

Figure 7.26: Tomosynthesis images (10° tomographic angle, 100 views) of the head phantom, reconstructed using (a) unfiltered and (b) disk-filtered backprojection. These images have been filtered (after reconstruction) using unsharp masking.

the open-mouth view in more ideal conditions cannot be made with this volumetric tomography system, and is beyond the scope of this dissertation.

The trade-off in tomosynthesis imaging between slice thickness in the reconstructed image and the number of views required is evident in the images of the cervical spine. The tomographic angle can be chosen by determining the appropriate slice thickness to adequately image the region of interest. This choice, along with the overall thickness of the object, then decides the number of views needed. The artifacts present in the reconstructed images suggest that at least 100 views are needed for a 50° tomographic angle dataset of the head phantom. This tomographic angle is sufficient to adequately remove the overlying structures in order to visualize the upper cervical spine. If a larger slice thickness is acceptable, then a 20° tomographic angle can be used with 50 views. It is uncertain whether or not this scenario would be sufficient, however, since out-of-plane objects begin to become apparent in images of C-1 and C-2 for a 20° tomographic angle. A 10° tomographic angle yields images which have strong artifacts from the large slice thickness.

It appears that the number of views required for visualizing the cervical spine is quite high, because of the complex structures present in this region. This is certainly the case for simple backprojection, as demonstrated in this chapter. It is possible, however, that this restriction could be less stringent for an alternative reconstruction scheme. We have limited our evaluation of tomosynthesis to unfiltered and disk-filtered backprojection, but other techniques such as iterative reconstructions could be examined if the current techniques prove too limiting for a clinical application.

An additional layer of complexity for in-vivo imaging of the cervical spine which was not present in the experiments with the head phantom is the presence of dental fillings. Since many patients have fillings, an examination of the imaging ramifications may be an important aspect for further exploration. Dental fillings represent a difficult imaging task because of the high density of these out-of-plane objects. Presumably, they will be less effectively blurred by tomosynthesis than the other overlying jaw and mouth structures. It should be noted that this is also a problem in CT [72]. The problem is somewhat different in radiography, where a filling would project onto a single location. Whether or not this would be preferable to the streaking in CT or incomplete suppression in tomosynthesis would depend on whether the radiographic artifact obscured an area of interest, and whether the blurred artifacts in the tomographic applications were of low enough intensity as to not mask any areas of interest. If not, this may place restrictions on the tomographic angle in order to produce a blurring radius large enough in order to place the blurred (and reduced intensity) reconstruction of the fillings outside the region of interest. It is reasonable to expect that this is possible, since the same difficulty applies for motion tomography, which has been successfully used to image the cervical spine.

Overall, the application of tomosynthesis to imaging of the upper cervical spine appears quite promising. The visualization of C-1 and C-2 is far superior to a standard A-P radiograph. In addition, there is flexibility in the choice of imaging parameters with tomosynthesis, based on the desired final images. In addition, the disk filter improves visualization of these vertebrae by more uniformly blurring the overlying jaw structures.

7.3 Conclusions

Application of circular tomosynthesis appears quite promising in the areas of mammography and imaging of the upper cervical spine. Experiments with the mammography phantom suggest that tomosynthesis can improve image quality over conventional radiography in terms of both removing overlying structures and providing information regarding the 3D location of calcifications. This is validated by the images of the mastectomy sample. Tomosynthesis datasets with the head phantom suggest that visualization of C-1 and C-2 can be improved compared to A-P radiographs due to the removal of the overlying jaw structures. In addition, use of the disk filter derived in Ch. 6 appears beneficial in these complex, clinically-relevant imaging scenarios. The use of disk-filtered backprojection more effectively blurs off-plane objects, which allows better perception of the imaging plane in complex 3D objects.

Chapter 8

Summary and Future Work

This dissertation has focused on the development of a test-bed system for volumetric tomographic imaging. This system was designed for in-vitro digital x-ray imaging. While much of this work has been presented for application to circular tomosynthesis, the same system and tools can be applied to more general volumetric imaging.

The main contributions of this dissertation include:

• The development of a volumetric tomography system based on a prototype digital flat-panel x-ray detector. This test-bed system allows automatic digital data acquisition for objects placed on a custom computer-controlled rotational positioning stage. The work in this chapter has been submitted for publication [91].

• A study of the sensitivity of the system to geometrical misalignments. It demonstrates the need for either precise mechanical alignment or a software-based correction technique, as well as highlights some of the critical geometrical parameters. This work motivated the development of a technique to correct for the geometrical misalignments of the x-ray system. The work in this chapter has been submitted for publication [91].

• A software-based technique to correct for geometrical misalignments without requiring precise system alignment. This approach uses the x-ray system itself to measure the system geometry using either a calibration phantom or fiducial markers. This data is used with a projection simulator to numerically fit the system geometry, which can then be used to re-map the data for proper image reconstruction. The work in this chapter has been submitted for publication [91].

• The development of a filtering technique to more uniformly blur out-of-plane objects in circular tomosynthesis. While tomosynthesis can never perfectly reconstruct an object because it does not sample all of frequency space, the impulse response can be altered in order to improve the visualization of in-plane objects relative to out-of-plane objects. In particular, the ring-shaped blur of circular tomosynthesis can be changed to a disk-shaped blur (which may be superior) without the collection of any additional information. This allows the system to mimic systems with more complex motions. The work in this chapter has been submitted for publication [92].

• The demonstration of the potential application of the tools developed in this dissertation to the clinical environment. We have examined the application of tomosynthesis to mammography and cervical spine imaging. In mammography, tomosynthesis is superior to current radiographic techniques due to its ability to localize calcifications in 3D space, and to suppress the display of overlying tissue structures. In cervical spine imaging, tomosynthesis is superior to current open-mouth radiographic views in its ability to image C-1 and C-2 while blurring the overlying jaw structures. A portion of this work has been submitted for publishing [92], and additional portions have been presented [93] and will be submitted for publication.

• The analysis of a potential detector for polychromatic x-ray imaging. This indirectly-related project is the optimization of imaging techniques for dual energy x-ray imaging. Such an approach is beneficial when making quantitative measurements of tissue parameters, such as measuring bone calcification when diagnosing osteoporosis. The work in this chapter has been published [94].

The main areas of future work include:

• Construction of other filters for tomosynthesis. The framework developed in Ch. 6 for the disk filter can be used to generate other filters for altering the blurring of out-of-plane objects. For instance, filters could be developed which optimize a given image metric.

• Generalization of the tools to volumetric CT imaging. In addition to circular tomosynthesis, the volumetric tomography system can be used for radiographic and VCT imaging. Some of the geometrical requirements of VCT differ from volumetric imaging, but the same approach can be taken to allow the proper reconstruction of images in this modality. In addition, the approach to developing filters for image reconstruction can be modified for this mode of operation.

- Examination of alternative reconstruction techniques. The images presented in this dissertation were reconstructed using unfiltered and filtered backprojection. Alternative techniques, such as iterative reconstruction, could be used instead. Important imaging parameters, such as the number of views required for an imaging task, or image noise, could change based on the type of reconstruction scheme. Examination of alternative techniques would allow the optimization of imaging techniques for specific applications.

- Development of a patient-based system. The volumetric tomography system developed in this dissertation is a test-bed system for in-vitro imaging. Given the success of this system, a patient-based system could be developed in order to study volumetric tomographic imaging in a clinical setting. This would allow for in-vivo demonstration of the techniques developed in this dissertation.

Appendix A

Dual Energy X-Ray Imaging

This appendix consists of a paper for analyzing the optimization of a theoretical detector for polychromatic x-ray imaging. The formatting has been modified slightly in order to conform to the style of this dissertation. The dissertation author was the primary author of this paper, and contributed to all aspects of its research and production. Because of the indirect relationship of this appendix with the body of the dissertation, this appendix is left in a more self-contained format.

Depth-Segmented Detector X-ray Absorptiometry

Grant M. Stevens and Norbert J. Pelc

Med. Phys. 27(5), May 2000

Abstract

A new energy-dependent multi-cell detector, which is a generalization of the conventional front-back detector, was studied using computer simulations. The noise performance of the detector for bone quantitation was examined in comparison to an ideal energy discriminating detector, and front-back detectors with and without inter-detector filters. The front-back detectors were optimized for a reference object composed of water and bone, and then compared to the new detector over a range of object compositions. In this appendix, precision in calculated bone thickness is used as the criterion for evaluating detector performance. Simulations show that the segmented detector always performs better than the front-back detector without an inter-detector filter. It out-performs the detector incorporating a filter by an amount that depends on the heterogeneity of the x-ray spectrum. In addition, for single component radiographic images, this multi-cell detector retains information which is lost in the front-back detector with a filter layer.

A.1 Introduction

X-ray measurements at two energies can be used for selective material imaging [95]. While applications such as imaging of chest [96] and breast [97] have been explored, the most common use for this type of imaging, is in the quantitative measurement of bone. Dual energy x-ray absorptiometry is the dominant bone measurement technique in the US [98]. With the recent FDA approval of new drugs for treating the loss in bone resulting from osteoporosis, interest in performing bone mineral measurements has been strengthened [99–101].

Dual energy imaging can be performed using monoenergetic sources, such as radionuclides. This can lead to motion artifacts during the long scan times required or poor precision in the images, due to the low output of the sources. Alternatively, high output monoenergetic sources can be approximated by using kV-switched x-ray tubes with appropriate filtration [102]. While this method is viable, it is technically complex. A single x-ray exposure can be used with a front-back detector, and its performance can be improved with the incorporation of a filter layer between the two cells [103–108]. While this method is simpler to implement, its precision is inferior to that of the dual kVp approach for the same dose [109].

Alternatively, consider a detector in which the energy deposited could be measured as a function of depth in the detector. Information about the spectrum of the x-ray beam would be extracted from the signal as a function of depth. This is essentially a generalization of the front-back detector. We hypothesized that this detector would outperform the front-back detector, both with and without an inter-detector filter.

In addition to making "material selective" images, multi energy imaging systems may be called upon to generate "radiographic" images [106]. For example, dual energy x-ray absorptiometry (DEXA) systems yield not only images and quantitation of bone mineral using dual energy subtraction, but also high SNR single energy anatomic images. Therefore, this mode was included in our evaluation of the relative performance of the multi-cell detector.

In this appendix, we report the results of computer simulations which compare the precision in quantitating bone using front-back detectors, with and without a filter, and the multi-cell detector. X-ray measurements are simulated for a range of tissue and bone thicknesses, and the resulting bone precision is determined. In order to provide a reference for these comparisons, a perfect energy-discriminating detector is simulated as an ideal detector.

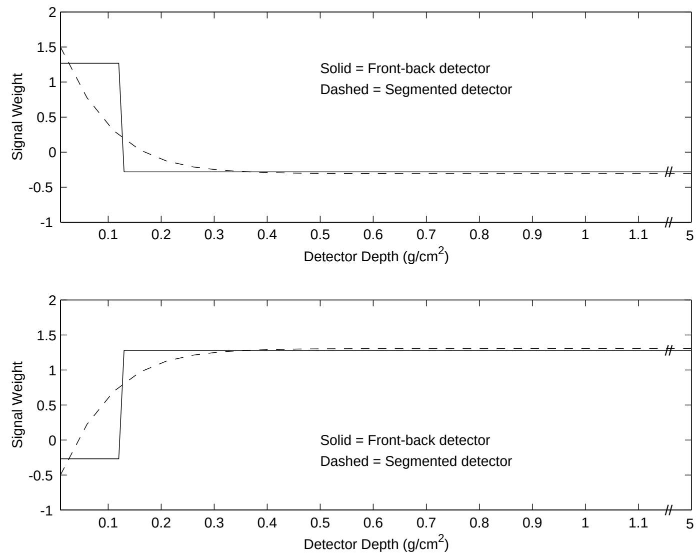

Figure A.1: Weighting functions of a two cell detector (solid) and a segmented detector (dashed) for the calculation of intensity at each energy in a dual energy spectrum. The top subplot shows the weights to generate the low energy signal and the bottom subplot shows the high energy weights. In this example, the detector is NaI, the two energies are 44 and 100 keV, and $\alpha_j = E_j$.

A.2 Motivation

A.2.1 Two Cell Detector

Consider the case of an x-ray beam containing photons of two energies incident on a front-back detector. The detector signals from the two cells are:

$$S_F = \alpha_1 \eta_{F1} N_1 + \alpha_2 \eta_{F2} N_2 \quad , \quad S_B = \alpha_1 \eta_{B1} N_1 + \alpha_2 \eta_{B2} N_2 \tag{A.1}$$

Here, S_F is the signal from the front cell, and S_B is the signal from the back cell. The detection efficiency for the front cell at energy E_j (j=1 ... 2) is η_{Fj}, and η_{Bj} is the detection efficiency for the back cell at energy E_j. Note that the back cell efficiencies include the effect of the x-rays absorbed in the front cell. The term α_j is a constant which has value 1 for a photon-counting detector and value equal to the energy, E_j, for an intensity-based detector. N_1 and N_2 are the expected number of x-rays of energy E_1 and E_2 transmitted through the body.

From the signals given in Eq. (A.1), the number of x-rays transmitted through the body at each of the two energies can be obtained:

$$N_1 = \left(\frac{1}{\alpha_1}\right)\left(\frac{\eta_{B2}S_F - \eta_{F2}S_B}{\eta_{F1}\eta_{B2} - \eta_{F2}\eta_{B1}}\right) \quad , \quad N_2 = \left(\frac{1}{\alpha_2}\right)\left(\frac{-\eta_{B1}S_F + \eta_{F1}S_B}{\eta_{F1}\eta_{B2} - \eta_{F2}\eta_{B1}}\right) \tag{A.2}$$

Thus, the number of photons at each energy in Eq. (A.2) can be expressed as a weighted sum of the front and back detector cell signals:

$$N_1 = f_{F1}S_F + f_{B1}S_B \quad , \quad N_2 = f_{F2}S_F + f_{B2}S_B \tag{A.3}$$

In Eq. (A.3), the weighting functions, f_{F1} f_{F2} f_{B1} and f_{B2}, are easily obtained by examination of Eq. (A.2). Photons detected in the front cell are weighted by f_{F1} and f_{F2} regardless of where in the front cell they are detected. Similarly, photons contributing to the back cell signal are weighted by f_{B1} and f_{B2}. Thus, we can interpret the contribution of photons detected at various depths in the detector as shown graphically in Fig. A.1 for a representative design. Because most of the low energy x-rays are absorbed in the front cell while most of the high energy x-rays penetrate to the back cell, the low energy intensity (N_1, the top subplot in Fig. A.1) is largely from the front cell. A small amount of the back cell signal is subtracted, as noted by the negative weighting, in order to remove the effect of high energy x-rays absorbed in the front detector. Likewise, the high energy intensity (N_2) has a small negative weighting for the front cell signal. The weightings as functions of depth are discontinuous at the boundary between the front and back cells. From this, we expect that signal generated near the boundary is not being optimally utilized, and that segmenting the detector more finely in depth could be beneficial.

A.2.2 Multi-cell Detector

A derivation similar to that above can be made for a detector which is segmented into N cells along the path of the incident x-rays. The detector signals from each of the N cells are:

$$S_i = \alpha_1 \eta_{i1} N_1 + \alpha_2 \eta_{i2} N_2 \quad , \quad i = 1 \dots N \tag{A.4}$$

Here, η_{ij} is the detector efficiency of cell i at energy E_j, which includes the effect of the cells in front of the ith cell; while N_j and α_j are as before. Eq. (A.4) can be solved for the number of low and high energy x-rays as weighted functions of the cell signals, as was done above for the two cell case. Since the system of equations is overdetermined, in order to solve this in the general N cell case, a weighted least squares approach is used. The weighted sum of the squared differences between the measured signal and the modeled signal given (Eq. (A.4)) is:

$$\chi^2 = \sum_{i=1}^{N} [\tilde{S}_i - \alpha_1 \eta_{i1} N_1 - \alpha_2 \eta_{i2} N_2]^2 w_i \tag{A.5}$$

Here, $\tilde{S}_i$ is the measured signal from the ith cell, and w_i is a weighting factor. For optimal SNR, the ideal choice for w_i is the inverse of the variance of $\tilde{S}_i$ [110], which can be approximated by the inverse of the variance of the modeled signal. Setting the partial derivatives of Eq. (A.5) with respect to N_1 and N_2 equal to zero and solving for the number of low and high energy x-rays as weighted sums of the detector signals yields:

$$N_j = \sum_{i=1}^{N} f_{ij} \tilde{S}_i \quad , \quad j = 1, 2 \tag{A.6}$$

where

$$f_{ij} = \frac{w_i}{\alpha_j} \frac{(\sum_{k=1}^{N} \eta_{k,3-j}^2 w_k)\eta_{ij} - (\sum_{k=1}^{N} \eta_{k1}\eta_{k2} w_k)\eta_{i,3-j}}{(\sum_{k=1}^{N} \eta_{k1}^2 w_k)(\sum_{k=1}^{N} \eta_{k2}^2 w_k) - (\sum_{k=1}^{N} \eta_{k1}\eta_{k2} w_k)^2} \tag{A.7}$$

As the number of cells increases, the weighting functions in Eq. (A.7) more closely approximate continuous functions. Example weighting functions for a 100 cell detector are shown in Fig. A.1. As expected, the low energy signal is derived mainly from the front region of the detector, with a negative weighting for the deeper cells. A detector with only two cells is hindered because it must use a constant weighting over a range of detector depths in which the optimal weighting changes significantly. A detector which is segmented into more cells is better able to accommodate the region of the detector where comparable number of low and high energy x-rays are absorbed. An additional advantage of the multi-cell detector is its flexibility to adapt to changes in the spectral composition due either to hardening of the beam or changes in the technique. The front back detector is unable to adapt to these changes. This simple derivation shows the increased flexibility of the multi-cell detector, which can more finely differentiate the regions of x-ray absorbance in the detector.

A.3 Methods

A.3.1 Bone Imaging

We derive first the well-known relationship for dual monoenergetic imaging and then generalize for polychromatic beams. Use of more then two energies is then studied.

Two Energy Measurements

Given the motivation of how detectors record energy dependent signals, consider the task of extracting the thickness of bone in the object from the detector signals. The simplest conceptual approach to this problem is to use two single energy measurements (i.e., each measurement is sensitive to photons of only a single energy). As is well known, this could be achieved, for example, by two successive measurements of two monoenergetic beams incident on a single cell detector. The amount of bone present is a simple linear combination of the log signals at the two energies, L_1 and L_2:

$$B = \frac{\mu_{W2} L_1 - \mu_{W1} L_2}{\mu_{W2}\mu_{B1} - \mu_{W1}\mu_{B2}} \tag{A.8}$$

Here, L_j is the logarithm of the ratio of the radiation incident on the body to the radiation transmitted through the body, μ_{Wj} and μ_{Bj} represent the energy dependent linear attenuation coefficients of water and bone, respectively. The numerical subscripts denote energy, and B is the thickness of bone (alternatively, one can use mass attenuation coefficients to compute bone mass per unit area.) The expected noise in the calculated bone can be derived using propagation of errors. Assuming the measurements have uncorrelated noise, the expected noise is:

$$\sigma_B^2 \equiv \sum_{j=1}^{2} (\frac{\partial B}{\partial L_j})^2 (\frac{\partial L_j}{\partial S_j})^2 \sigma_{S_j}^2 \quad = \quad \frac{\mu_{W2}^2 \alpha_1 S_2 + \mu_{W1}^2 \alpha_2 S_1}{S_1 S_2 (\mu_{W2}\mu_{B1} - \mu_{W1}\mu_{B2})^2} \tag{A.9}$$

S_j is the detector signal at energy E_j, which has a variance of $\alpha_j S_j$. Inherent in Eq. (A.9) is the assumption that the incident intensity is well known from prior measurements, or is relatively noiseless. If this is not the case, a more general form of Eq. (A.9) can account for the additional noise source.

In the case of DEXA measurements using x-ray tubes, the spectra are broader. Because of this, the signal equations are not as easy to linearize. Normally, linearization is performed using beam hardening corrections such as a polynomials in the log signals. Because our criterion for comparing detector systems is noise in quantitated bone, we will use a simpler approach. We seek to quantify the effect of signal fluctuation due to quantum noise on the measured amount of bone. We allow the system to operate differentially about a reference operating point, which is the expected value of tissue and bone. The detector signals are expressed as these reference signals modified by attenuation through additional small amounts of water and bone. Over a small range of thicknesses, attenuation of the polychromatic beam can be approximated as exponential, characterized by the effective attenuation coefficients for bone and water, which are defined as:

$$\overline{\mu}_{Bi} \equiv \frac{-\frac{\partial S_i}{\partial \delta B}}{S_i} \quad , \quad \overline{\mu}_{Wi} \equiv \frac{-\frac{\partial S_i}{\partial \delta W}}{S_i} \tag{A.10}$$

For small δB and δW, the two DEXA signals can be approximated as:

$$S_i = (\sum_{j=1}^{M} N_j^{ref} \alpha_j \eta_{ij}) e^{-\overline{\mu}_{Bi}\delta B - \overline{\mu}_{Wi}\delta W} \quad , \quad i = 1 \ldots 2 \tag{A.11}$$

Here, N_j^{ref} is the expected number of x-rays to penetrate through the reference amount of tissue and bone at energy E_j, and M is the number of energy bins in the discretized x-ray spectrum. Eq. (A.11) can be solved directly for the incremental amount of bone:

$$\delta B = \frac{\overline{\mu}_{W2} \ln(\frac{S_1^{ref}}{S_1}) - \overline{\mu}_{W1} \ln(\frac{S_2^{ref}}{S_2})}{\overline{\mu}_{B1}\overline{\mu}_{W2} - \overline{\mu}_{W1}\overline{\mu}_{B2}} \tag{A.12}$$

where S_j^{ref} is the signal with δB and δW equal to zero. The variance, as proven by Morgan [106], is:

$$\sigma_B^2 = \frac{\overline{\mu}_{W2}^2 S_2^2 (\sum_{j=1}^{M} N_j \alpha_j^2 \eta_{1j}) + \overline{\mu}_{W1}^2 S_1^2 (\sum_{j=1}^{M} N_j \alpha_j^2 \eta_{2j})}{(S_1 S_2)^2 (\overline{\mu}_{B1}\overline{\mu}_{W2} - \overline{\mu}_{W1}\overline{\mu}_{B2})^2} \tag{A.13}$$

where each signal has variance $\sum_{j=1}^{M} N_j \alpha_j^2 \eta_{ij}$. In Eq. (A.12), δB can also be interpreted as the fluctuation in the computed bone due to the fluctuation of the measured signals (S_j) about the expected values (S_j^{ref}). Eqs. (A.12) and (A.13) reduce to Eqs. (A.8) and (A.9) in the case of two separate energy measurements ($M = 2$, $\eta_{12}, \eta_{21} = 0$), with the attenuation coefficients replaced by effective attenuation coefficients. Numerical simulations were performed and validated the accuracy of this approach to calculate the noise in measured bone thickness. Eq. (A.13) can be used to calculate the variance in computed bone for techniques that use two polyenergetic measurements, such as dual kV DEXA or measurements with a front-back detector.

More Than Two Energy Measurements

To analyze the performance of the proposed multi-cell detector, we need to develop a method to calculate the amounts of tissue and bone given more than two energy measurements. A detailed derivation of the equations in this section is given in Sec.

A.7. Suppose that measurements with more than two energies are available, e.g. for an energy-discriminating detector and an x-ray spectrum containing M different energies. For $M > 2$, the problem of quantitating a two-component mixture (i.e., bone and water) is overdetermined. A weighted least squares solution may be employed to optimally solve for the amount of bone present. The log of the x-ray transmission at each energy is related to the amount of bone and water. We solve for the amounts of bone and water that minimize the weighted sum of the squared difference between the actual log measurements and the expected values for a given amount of bone and tissue. The optimal weights are the inverse of the log signal variances, as previously noted. The weighted least squares solution for the amount of bone is:

$$B = \frac{(\sum_{j=1}^{M} \mu_{Wj}^2 w_j)(\sum_{j=1}^{M} \mu_{Bj} L_j w_j) - (\sum_{j=1}^{M} \mu_{Bj}\mu_{Wj} w_j)(\sum_{j=1}^{M} \mu_{Wj} L_j w_j)}{(\sum_{j=1}^{M} \mu_{Bj}^2 w_j)(\sum_{j=1}^{M} \mu_{Wj}^2 w_j) - (\sum_{j=1}^{M} \mu_{Bj}\mu_{Wj} w_j)^2} \tag{A.14}$$

For the two energy case ($M = 2$, $w_1, w_2 = 1$), Eq. (A.14) reduces to Eq. (A.8), as expected. As before, one may calculate the expected noise in the measured bone:

$$\sigma_B^2 = \sum_{n=1}^{M} [\frac{(\sum_{j=1}^{M} \mu_{Wj}^2 w_j)\mu_{Bn} w_n - (\sum_{j=1}^{M} \mu_{Bj}\mu_{Wj} w_j)\mu_{Wn} w_n}{(\sum_{j=1}^{M} \mu_{Bj}^2 w_j)(\sum_{j=1}^{M} \mu_{Wj}^2 w_j) - (\sum_{j=1}^{M} \mu_{Bj}\mu_{Wj} w_j)^2}]^2 \frac{\alpha_n}{S_n} \tag{A.15}$$

As before, the variance in each signal is $\alpha_n S_n$.

Equations A.14 and A.15 describe the case of M monoenergetic measurements. For the case in which we have more than two polychromatic measurements, we replace the attenuation coefficients with effective attenuation coefficients and operate about a reference amount of bone and tissue:

$$\delta B = \frac{(\sum_{i=1}^{K} \overline{\mu}_{Wi}^2 w_i)(\sum_{i=1}^{K} \overline{\mu}_{Bi} L_i w_i) - (\sum_{i=1}^{K} \overline{\mu}_{Bi}\overline{\mu}_{Wi} w_i)(\sum_{i=1}^{K} \overline{\mu}_{Wi} L_i w_i)}{(\sum_{i=1}^{K} \overline{\mu}_{Bi}^2 w_i)(\sum_{i=1}^{K} \overline{\mu}_{Wi}^2 w_i) - (\sum_{i=1}^{K} \overline{\mu}_{Bi}\overline{\mu}_{Wi} w_i)^2} \tag{A.16}$$

Here, K refers to the number of polychromatic measurements, while M is still the number of energies in the spectrum. L_i is the logarithm of the ratio of the expected signal for the reference amount of bone and tissue to the ith measured signal. From this, the variance in the computed bone can be analytically predicted:

$$\sigma_B^2 = \sum_{n=1}^{K} [\frac{(\sum_{i=1}^{K} \overline{\mu}_{Wi}^2 w_i)\overline{\mu}_{Bn} w_n - (\sum_{i=1}^{K} \overline{\mu}_{Bi}\overline{\mu}_{Wi} w_i)\overline{\mu}_{Wn} w_n}{(\sum_{i=1}^{K} \overline{\mu}_{Bi}^2 w_i)(\sum_{i=1}^{K} \overline{\mu}_{Wi}^2 w_i) - (\sum_{i=1}^{K} \overline{\mu}_{Bi}\overline{\mu}_{Wi} w_i)^2}]^2 \frac{1}{S_n^2} \sum_{j=1}^{M} N_j \alpha_j^2 \eta_{nj} \quad (A.17)$$

As before, the variance in each signal is $\sum_{j=1}^{M} N_j \alpha_j^2 \eta_{ij}$. We stress here that with a single effective attenuation coefficient at each measurement, Eq. (A.16) may not be accurate over a wide dynamic range and beam hardening corrections may be needed. However, Eq. (A.17) can still be used to predict the noise performance for bone quantitation.

A.3.2 Radiographic Imaging

When generating a "radiographic" image, we are mainly interested in the ability to form a single "anatomic" image from all the energy measurements, and we are particularly interested in the ability of this image to portray subtle details in the bone present. Consider a small region of the image over which we can consider the total thickness to be relatively constant. We want to examine the ability of a single combined image to depict a small change T in the thickness of bone. For a single energy measurement, the expected signal can be expressed as:

$$S_T = S^{ref} e^{-(\mu_B - \mu_W)T} \quad (A.18)$$

Here, S^{ref} is the signal for the reference operating point, and T is the incremental thickness of water replaced by bone. The monoenergetic x-ray measurement of T using Eq. (A.18) has a variance of:

$$\sigma_T^2 = \frac{\alpha}{S_T(\mu_B - \mu_W)^2} \quad (A.19)$$

where α is the signal per photon. For a single polychromatic measurement, the attenuation coefficients in Eqs. (A.18) and (A.19) would be replaced by effective attenuation coefficients.

If more than one energy measurement is available, the problem is overdetermined.

That is, a radiograph can be formed at each energy and we seek the ideal combination of these. These multiple measurements could result from detecting more than one monoenergetic beam or from using segmented detectors to make multiple measurements of a polychromatic spectrum. For monoenergetic x-rays, each photon energy produces a signal of the form given by Eq. (A.18) and therefore an estimate of T. Using the same optimization methodology as before, the minimum least squares linear combination of these is:

$$T = \frac{\sum_{i=1}^{K} L_i(\mu_{Bi} - \mu_{Wi})w_i}{\sum_{i=1}^{K}(\mu_{Bi} - \mu_{Wi})^2 w_i} \tag{A.20}$$

L_i is the log signal relative to the reference amount of tissue and bone, and K is the number of measurements. As before, the optimal weights are the inverse of the log signal variances. Each signal S_n has variance $\alpha_n S_n$. The variance in the estimated value of T is:

$$\sigma_T^2 = \sum_{n=1}^{K} \frac{\alpha_n[(\mu_{Bn} - \mu_{Wn})w_n]^2}{S_n[\sum_{i=1}^{K}(\mu_{Bi} - \mu_{Wi})^2 w_i]^2} \tag{A.21}$$

Eq. (A.20) describes how the multiple single energy radiographic images should be combined, and Eq. (A.21) is a measure of the image quality (variance) to be expected.

For multiple polychromatic measurements (e.g. with a depth segmented detector), Eqs. (A.20) and (A.21) hold with slight modifications. The attenuation coefficients are replaced by effective attenuation coefficients, and the signals have variances $\sum_{j=1}^{M} N_j \alpha_j^2 \eta_{nj}$ (M denotes the number of energy bins in the discretized spectrum). Thus, for a polychromatic beam:

$$T = \frac{\sum_{i=1}^{K} L_i(\overline{\mu}_{Bi} - \overline{\mu}_{Wi})w_i}{\sum_{i=1}^{K}(\overline{\mu}_{Bi} - \overline{\mu}_{Wi})^2 w_i} \tag{A.22}$$

and

$$\sigma_T^2 = \sum_{n=1}^{K} \frac{[(\overline{\mu}_{Bn} - \overline{\mu}_{Wn})w_n]^2 \sum_{j=1}^{M} N_j \alpha_j^2 \eta_{nj}}{S_n^2[\sum_{i=1}^{K}(\overline{\mu}_{Bi} - \overline{\mu}_{Wi})^2 w_i]^2} \tag{A.23}$$

A.3.3 Simulations

The algorithms described in Secs. A.3.1 and A.3.2 were employed in computer simulations to model system performances over a range of body compositions. The systems simulated were: (1) a perfect energy-discriminating system, (2) a front-back detector with and (3) without an inter-detector filter, and (4) a multi-cell detector. In these simulations, the total thickness of the detectors was chosen to be 5 g/cm^2 of NaI, as in Kelcz *et al.* [109]. This total thickness was divided into segments of unequal thickness for the front-back detectors, and into 100 uniformly sized cells for the segmented detector proposed in this appendix. While a detector segmented into this many cells may not be practical, a 100 cell design was used in order to study the maximum possible benefit of depth segmentation of the type envisioned here. Unless otherwise mentioned, the detectors were assumed to be intensity-based ($\alpha_j = E_j$). The attenuation coefficients for the detector, filters, and tissues used for the calculations are from NIST [111]. The bone attenuation coefficient was based on cortical bone (% by weight: 3.4% H, 15.5% C, 4.2% N, 43.5% O, 0.1% Na, 0.2% Mg, 10.3% P, 0.3% S, 22.5% Ca) [112]. The simulations were run for a range of bone (0.8 - 1.8 cm) and water (15 - 25 cm) thicknesses. A density of 1.65 g/cm^3 was assumed for bone, and a density of 1.04 g/cm^3 for water (to mimic muscle tissue) [15]. Simplifying assumptions of no scatter and no cross-talk between cells in the detectors were made in order to carry out the noise analysis. All analytical algorithms were verified using numerical simulations.

A two monochromatic energy simulation was run using a spectrum containing x-rays at 44 keV and 100 keV, modeling the emissions of ^{153}Gd. The ratio of the incident intensities at the two energies was optimized for the front-back detector without a filter, keeping the total number of x-rays fixed. Alternatively, one could choose this ratio by holding the dose constant, but this should not greatly change the comparison among systems for this simple case. The segmentation into front and back cells was optimized to minimize the variance in the measured amount of bone for an object composed of 1.3 cm of bone and 20 cm of water, keeping the total detector thickness fixed. This optimization yielded a ratio of 18:1 low to high energy x-rays, and front and back cells of 0.12 g/cm^2 and 4.88 g/cm^2, respectively, for the front-back detector without an inter-detector filter. For the front-back with a filter, the filter material was assumed to also be NaI, as in Cardinal and Fenster where the filter layer was composed of the same material as the detector [104]. Part of the total 5 g/cm^2 of the detector was assigned to be the filter (i.e., the filter is essentially an inactive NaI cell). The optimal apportionment of the total thickness was 0.08 g/cm^2 for the front cell, 0.11 g/cm^2 for the filter, and 4.81 g/cm^2 for the back cell.

Simulations were also run for photon counting detectors ($\alpha_j = 1$). The ratio of x-rays was re-optimized, yielding a ratio of 8.7:1 low to high energy x-rays. Optimal cell sizes were 0.15 g/cm^2 for the front cell and 4.85 g/cm^2 for the back cell for the front-back detector with no filter, and 0.10 g/cm^2 for the front cell, 0.12 g/cm^2 for the filter, and 4.78 g/cm^2 for the back cell for the front-back detector with a filter.

Polychromatic beam simulations were run using a 150 kVp beam filtered with 1mm Al (to model inherent filtration) and an additional 0.17mm Hf (as in Cardinal and Fenster [104]). The Hf filtration is beneficial because hafnium, with a K-edge at 65.35 keV, produces a bimodal spectrum. The spectrum was calculated using in-house software based on theory by Storm *et al.* [113] and data from Dyson [114], and is shown in Fig. A.2. For this polychromatic spectrum, the optimal cell sizes were 0.23 g/cm^2 and 4.77 g/cm^2 respectively for the front-back detector without a filter, and 0.16 g/cm^2, 0.30 g/cm^2, and 4.54 g/cm^2 for the front-back detector with a filter. The cell sizes were not re-optimized for the construction of a radiographic image (Eq. (A.20)), as the goal was to compare the image noise from detectors optimized for quantitative bone measurements. We also considered a system with photon counting front-back detectors. The optimal cell sizes for this configuration were 0.26 g/cm^2 for the front cell and 4.74 g/cm^2 for the back cell for the front-back detector with no filter, and 0.16 g/cm^2 for the front cell, 0.31 g/cm^2 for the filter, and 4.53 g/cm^2 for the back cell for the front-back detector with a filter.

For each of the simulations, the predicted standard deviation in the thickness of bone was calculated. This standard deviation was used to compare the expected performance of each of the detector systems. The precision at the optimization point was used to compare how well each detector works at its optimal performance. Examination of the results away from the optimization point allows a comparison of

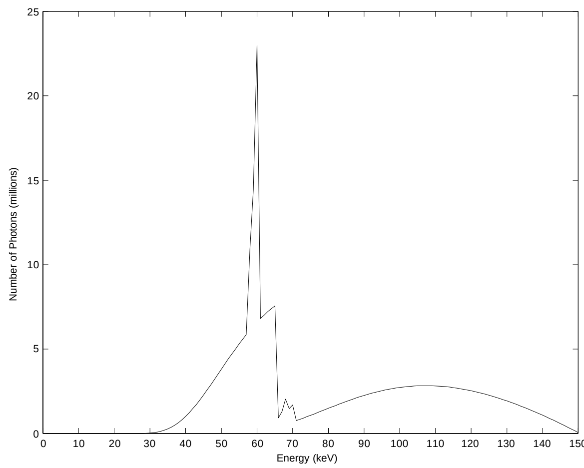

Figure A.2: X-ray spectrum used in polychromatic bone imaging and radiographic imaging (150kVp beam with 1mm Al and 0.17mm Hf filtration).

how the detectors perform relative to one another as the bone and water thicknesses move away from the design point. This demonstrates the relative flexibility of the detectors for use with different patients. In addition, a perfect energy-discriminating detector of the same overall thickness was simulated to be used as an ideal detector for comparison. In the case of polychromatic simulations, the signals from this ideal detector were combined optimally using the weighted least squares technique.

A.4 Results

A.4.1 Dual Energy Bone Imaging

Simulations using a dual energy spectrum (44 and 100 keV) show all of the segmented detectors to be significantly poorer than the ideal system (which has perfect energy separation). Fig. A.3 shows the noise performance of the front-back detector without a filter layer relative to the ideal energy-discriminating detector. From our simulations, the performance of the front-back detector can be improved by around 5% by the addition of the inactive filter layer. The improvement afforded by the addition of the filter layer was roughly uniform over the range of composition, ranging from

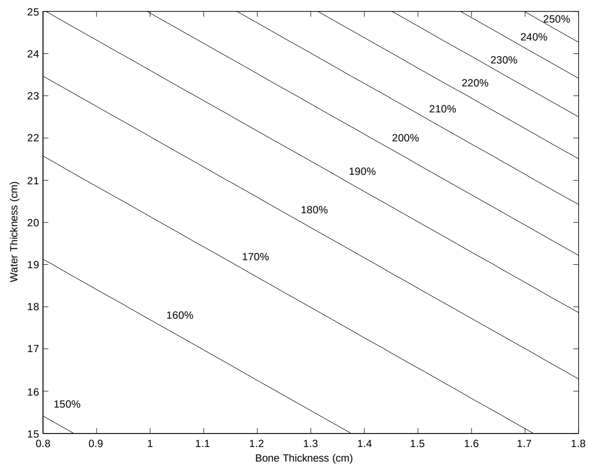

Figure A.3: Standard deviation in computed bone for the two cell detector relative to the ideal energy discriminating detector, for a two energy x-ray beam. The numerical values on the plot correspond to the contour lines to the left of the numbers. A value of 100% indicates equal standard deviations for the two cell detector and the ideal detector.

4.2% at 1.25 cm bone, 15 cm water to 5.0% at 1.80 cm bone, 25 cm water. The segmented detector achieves an additional 2-3% gain over the two cell detector with an intradetector filter, the greatest improvements being for thicker objects. These improvements are summarized in Table A.1.

A.4.2 Polychromatic Bone Imaging

In the case of a polychromatic beam, the performance of the two cell detector is even further from the ideal detector. Fig. A.4 shows that the intensity-based front-back detector without a filter yields a calculated bone thickness that has a standard deviation of approximately three times that of the equivalent measurement by a perfect energy-discriminating detector. An improvement of just over 6% can be made with the addition of an inactive filter layer. This improvement is quite homogeneous, ranging from 6.0% at 0.80 cm bone, 15 cm water to 6.4% at 1.80 cm bone, 20.0 cm water. An additional 5% gain can be achieved by using the segmented detector. Table A.1 summarizes the improvements for polychromatic bone imaging.

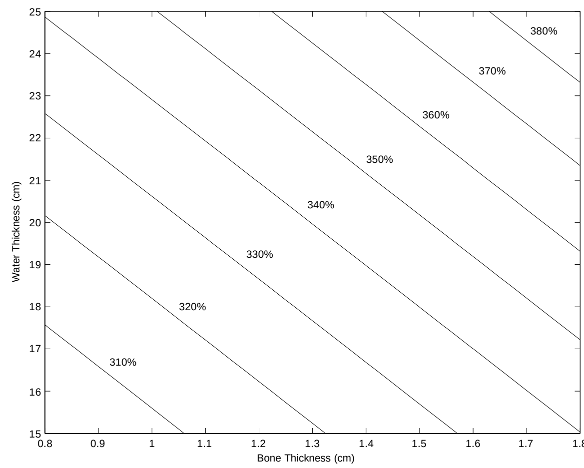

Figure A.4: Standard deviation in computed bone for the two cell detector relative to the ideal energy discriminating detector, for a filtered 150 kVp beam. The numerical values on the plot correspond to the contour lines to the left of the numbers. A value of 100% indicates equal standard deviations for the two cell detector and the ideal detector.

For all detector types (except the ideal energy discriminating detector), the photon counting mode ($\alpha_j = 1$) is superior to the intensity mode ($\alpha_j = E_j$). For example, for bone quantitation with a front-back detector with no filter and a polychromatic beam, photon counting reduces the standard deviation by about 30%. For this system, use of an inter-detector filter provides an additional 6% improvement, as is summarized in Table A.2. The segmented detector provides an additional improvement of 4-5% as compared to the front-back detector with a filter. Thus, the improvement provided by the segmented detector is slightly larger in an intensity detector than in photon counting mode.

A.4.3 Radiographic Imaging

For constructing a single radiographic image from multiple measurements, the depth discriminating detectors no longer perform as poorly as compared to the ideal energy-discriminating detector. Shown in Fig. A.5 is the standard deviation for a front-back detector relative to the ideal detector for a polychromatic beam. This figure shows

Spectrum	Front-back with filter	Segmented
44 and 100 keV	4.2 % - 5.0 %	6.0 % - 8.1 %
150kVp, 1 mm Al, 0.17 mm Hf	6.0 % - 6.4 %	10.4 % - 11.5 %

Table A.1: Reductions in standard deviation in the measured bone as compared to a front-back detector for the front-back detector with a filter and for the multi-cell detector, for the dual energy and polychromatic cases.

that the two cell detector without a filter is only 20-28% noisier than the ideal system. In the case of the front-back detector with a filter, the loss of information from wasting photons absorbed in the filter results in a further increase in noise of 16-17% throughout the range of water and bone thicknesses. The segmented detector, which retains these photons, yields a 1% improvement over the front-back detector without a filter and a 15% improvement over the front-back detector with a filter.

A.5 Discussion

Our dual energy simulations show all of the segmented detectors to be far inferior to the ideal system because of their incomplete energy separation. It can be seen in Figs. A.3 and A.4 that the relative performance worsens as a function of the total body thickness. All of the detectors behave similarly in this regard, and results from a shift in the x-ray spectrum incident on the detector due to beam hardening. As the total thickness increases, a higher percentage of high energy x-rays are retained in the beam and the signal from the front cell is increasingly less representative of a low energy

Spectrum	Front-back	Front-back with filter	Segmented
44 and 100 keV	22.8 % - 26.5 %	26.3 % - 30.4 %	27.7 % - 32.6 %
150kVp, 1 mm Al, 0.17 mm Hf	27.0 % - 32.9 %	31.6 % - 37.2 %	34.5 % - 40.3 %

Table A.2: Reductions in standard deviation in the measured bone as compared to a intensity-based front-back detector for the photon counting front-back detector without a filter, for the photon counting front-back detector with a filter, and for the photon counting multi-cell detector, for the dual energy and polychromatic cases.

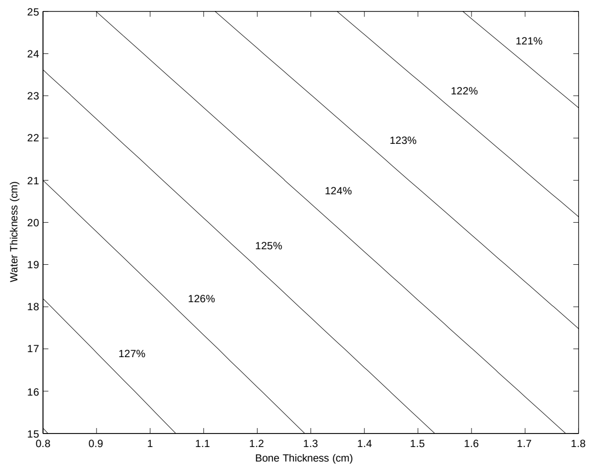

Figure A.5: Standard deviation in a single component image for a two cell detector relative to an ideal energy discriminating detector for a filtered 150 kVp beam. The numerical values on the plot correspond to the contour lines to the left of the numbers. A value of 100% indicates equal standard deviations for the two cell detector and the ideal detector.

measurement. The situation is further worsened for the two cell detectors because of their fixed cell size. Ideally, as the beam becomes richer in high energy photons, one should reduce the thickness of the front cell. These fixed systems, however, are unable to shrink the front cell size to counteract the larger proportion of high energy x-rays in the beam.

Our simulations demonstrate an improvement of around 6% for a two cell detector by the addition of an inactive filter layer. This is in agreement with previously published results on two cell detectors. Cardinal and Fenster [104] demonstrated an improvement of 6-7% for a similar attenuating object and filtered spectrum. Kelcz *et al.* [109] showed an improvement of 3-4% in high Z compounds, Gauntt and Barnes [107] showed an improvement of 4-6% for various object compositions, and Chakraborty and Barnes [108] showed an improvement of around 4% for a theoretical mammography setup.

A main purpose of our study was to evaluate whether a more finely segmented detector could improve on this performance. For a simple dual energy spectrum, the additional improvement in the standard deviation of bone provided by using a segmented detector is modest as compared to a front-back detector with a filter. For a polychromatic beam, the additional improvement in bone quantitation provided by the segmented detector over a front-back detector with a filter is larger than for the simple dual energy spectrum, and is significant. This suggests that the use of a filter is not as efficient at removing spectral overlap in this more complex case. All the divided detectors (i.e., front-back detectors with and without a filter, and the segmented detector) are hindered when used with polychromatic spectra because of the inherent averaging over energy which takes place in each cell.

In the additional role of using multiple measurements to construct a single "radiographic" image, the main factor in image quality is the number of x-rays absorbed in the detector. For this case, the depth discriminating detectors no longer perform as poorly as compared to the ideal energy-discriminating detector. Because the front-back detector with a filter wastes photons absorbed in the filter layer, the system has higher noise throughout the range of water and bone thicknesses. Thus, the use of a filter to increase the performance of a two cell detector for bone quantitation comes at the cost of increased noise in "radiographic" images. Because these photons are still available in the segmented detector system, they can be used to generate a less noisy image. This demonstrates the increased flexibility of the multi-cell detector.

As part of our study, we derived an algorithm to measure the composition of a two component system (e.g. tissue and bone) from more than two energy measurements (Eqs. (A.14) and (A.16)). The derivation was motivated by the need to use the data from the segmented detector, but the method may find more utility in other systems, for example with pulse height analysis.

A.6 Conclusions

We have developed a noise-based analysis to study the merit of a detector that is segmented in the depth direction for quantitative bone absorptiometry and for "radiographic" imaging. The detector allows the x-ray absorption as a function of depth to be used for energy discrimination. Because of the additional information available as compared to front-back detectors which combine photons into only two groups, we hypothesized that this approach would lead to lower noise and a level of performance closer to that of the ideal energy discriminating detector. Somewhat surprisingly, this segmented detector adds little improvement to the gain that an inactive filter layer makes to a front-back detector if the spectrum contains photons of only two energies. In the case of a polychromatic beam, this multi-cell detector approximately doubles the benefit of the inactive filter layer. A more significant advantage over the front-back detector with a filter is that the improved performance is achieved without discarding any photons. This results in significantly improved performance for "radiographic" imaging.

The simulations presented here assumed the new detector was segmented into 100 equal thickness portions. This large number of segments was selected in order to examine the full potential benefit of depth segmentation. Clearly, most of the gain could be achieved with a much more modest design. For example, a detector in which the photons absorbed in the filter layer would be allowed to generate signal (i.e., three segments of unequal thickness), such as suggested by Ergun *et al.* [105], would have performance comparable to the front-back detector with a filter for bone quantitation, and comparable to a system without the filter for "radiographic" imaging.

A.7 Supplement: More Than Two Energy Measurements

A.7.1 Single Cell Detector

In the case of a single cell, energy discriminating detector and a polychromatic beam, the energy signals are:

$$S_j = N_{0j}\alpha_j\eta_j e^{-\mu_{Bj}B-\mu_{Wj}W} \quad j = 1\ldots M \tag{A.24}$$

where N_{0j} is the number of photons at energy E_j which are incident on the body, α_j has value E_j for an intensity-based detector and value 1 for a photon counting detector, η_j is the detector efficiency at energy E_j, and M is the number of energy bins in the discretized spectrum. Log signals can be defined as:

$$L_j \equiv ln(\frac{N_{0j}\alpha_j\eta_j}{S_j}) = \mu_{Bj}B + \mu_{Wj}W \tag{A.25}$$

Because this system is overdetermined for quantitating bone, a weighted least squares technique can be used to solve for the amount of bone. A least squares statistic is defined as the weighted sum of the squared difference between the expected log signal at each energy (Eq. (A.25)), and the measured log signal $\tilde{L}_j$:

$$\chi^2 = \sum_{j=1}^{M}(\mu_{Bj}B + \mu_{Wj}W - \tilde{L}_j)^2 w_j \tag{A.26}$$

The optimal weights are the inverse of the log signal variances [110], where the variance in each signal S_j is $\alpha_j S_j$. Minimizing χ^2 (Eq. (A.26)) with respect to the amount of bone and water yields the amount of bone:

$$B = \frac{(\sum_{j=1}^{M}\mu_{Wj}^2 w_j)(\sum_{j=1}^{M}\mu_{Bj}L_j w_j) - (\sum_{j=1}^{M}\mu_{Bj}\mu_{Wj}w_j)(\sum_{j=1}^{M}\mu_{Wj}L_j w_j)}{(\sum_{j=1}^{M}\mu_{Bj}^2 w_j)(\sum_{j=1}^{M}\mu_{Wj}^2 w_j) - (\sum_{j=1}^{M}\mu_{Bj}\mu_{Wj}w_j)^2} \tag{A.27}$$

The expected noise in the bone can be calculated using propagation of errors:

$$\sigma_B^2 = \sum_{j=1}^{M}(\frac{\partial B}{\partial L_j})^2(\frac{\partial L_j}{\partial S_j})^2\sigma_{S_j}^2 \tag{A.28}$$

The expected variance in B is thus:

$$\sigma_B^2 = \sum_{n=1}^{M}[\frac{(\sum_{j=1}^{M}\mu_{Wj}^2 w_j)\mu_{Bn} - (\sum_{j=1}^{M}\mu_{Bj}\mu_{Wj}w_j)\mu_{Wn}}{(\sum_{j=1}^{M}\mu_{Bj}^2 w_j)(\sum_{j=1}^{M}\mu_{Wj}^2 w_j) - (\sum_{j=1}^{M}\mu_{Bj}\mu_{Wj}w_j)^2}]^2\frac{\alpha_n w_n^2}{S_n} \tag{A.29}$$

A.7.2 Segmented Detectors

The signal from each cell of a segmented detector (composed of K individual cells) used with a polychromatic beam can be approximated using effective attenuation coefficients. For each signal, a reference amount of bone and water is modified by attenuation through incremental thicknesses:

$$S_i = (\sum_{j=1}^{M} N_j^{ref} \alpha_j \eta_{ij}) e^{-\overline{\mu}_{Bi}\delta B - \overline{\mu}_{Wi}\delta W}, \quad i = 1 \ldots K \tag{A.30}$$

where effective attenuation coefficients for bone and water are defined as:

$$\overline{\mu}_{Bi} \equiv \frac{-\frac{\partial S_i}{\partial \delta B}}{S_i} \quad , \quad \overline{\mu}_{Wi} \equiv \frac{-\frac{\partial S_i}{\partial \delta W}}{S_i} \tag{A.31}$$

Here, N_j^{ref} is the expected number of x-rays to penetrate through the reference amount of tissue and bone at energy E_j, and M is the number of energy bins in the discretized x-ray spectrum. Log signals for each of the cells can be defined:

$$L_i \equiv ln(\frac{\sum_{j=1}^{M} N_j^{ref} \alpha_j \eta_{ij}}{S_i}) = \overline{\mu}_{Bi}\delta B + \overline{\mu}_{Wi}\delta W \tag{A.32}$$

As before, this system is overdetermined for quantitating bone, and we use a weighted least squares technique to solve for the amount of bone. The least squares statistic is written:

$$\chi^2 = \sum_{i=1}^{K} (\overline{\mu}_{Bi}\delta B + \overline{\mu}_{Wi}\delta W - \tilde{L}_i)^2 w_i \tag{A.33}$$

where $\tilde{L}_i$ is the measured log signal. Minimizing Eq. (A.33) with respect to the amount of bone and water yields the amount of bone present:

$$\delta B = \frac{(\sum_{i=1}^{K} \overline{\mu}_{Wi}^2 w_i)(\sum_{i=1}^{K} \overline{\mu}_{Bi} L_i w_i) - (\sum_{i=1}^{K} \overline{\mu}_{Bi}\overline{\mu}_{Wi} w_i)(\sum_{i=1}^{K} \overline{\mu}_{Wi} L_i w_i)}{(\sum_{i=1}^{K} \overline{\mu}_{Bi}^2 w_i)(\sum_{i=1}^{K} \overline{\mu}_{Wi}^2 w_i) - (\sum_{i=1}^{K} \overline{\mu}_{Bi}\overline{\mu}_{Wi} w_i)^2} \tag{A.34}$$

where w_i is the inverse of the expected variance in each signal S_i, i.e., $w_i^{-1} = \sigma_{S_i}^2 = \sum_{j=1}^{M} N_j \alpha_j^2 \eta_{ij}$. The expected noise in the bone can be calculated using propagation of errors:

$$\sigma_B^2 = \sum_{i=1}^{K} (\frac{\partial B}{\partial L_i})^2 (\frac{\partial L_i}{\partial S_i})^2 \sigma_{S_i}^2 \tag{A.35}$$

This yields:

$$\sigma_B^2 = \sum_{n=1}^{K} [\frac{(\sum_{i=1}^{K} \overline{\mu}_{Wi}^2 w_i)\overline{\mu}_{Bn} - (\sum_{i=1}^{K} \overline{\mu}_{Bi}\overline{\mu}_{Wi} w_i)\overline{\mu}_{Wn}}{(\sum_{i=1}^{K} \overline{\mu}_{Bi}^2 w_i)(\sum_{i=1}^{K} \overline{\mu}_{Wi}^2 w_i) - (\sum_{i=1}^{K} \overline{\mu}_{Bi}\overline{\mu}_{Wi} w_i)^2}]^2 \frac{w_n^2}{S_n^2} \sum_{j=1}^{M} N_j \alpha_j^2 \eta_{nj} \tag{A.36}$$

Bibliography

[1] O. Glasser, "W.C. Roentgen and the Discovery of the Roentgen Rays," American Journal of Roentgenology **165,** 1033–1040 (1995).

[2] P. Goodman, "The New Light: Discovery and Introduction of the X-Ray," American Journal of Roentgenology **165,** 1041–1045 (1995).

[3] P. Goodman, "The X-Ray Enters the Hospital," American Journal of Roentgenology **165,** 1046–1050 (1995).

[4] T. S. Curry III, J. F. Dowdey, and R. C. Murry Jr., *An Introduction to the Physics of Diagnostic Radiology* (Lea & Febiger, Philadelphia, 1984).

[5] D. G. Grant, "Tomosynthesis: A Three-Dimensional Radiographic Imaging Technique," IEEE Transactions on Biomedical Engineering **19,** 20–28 (1972).

[6] R. A. J. Gröenhuis, R. L. Webber, and U. E. Ruttimann, "Computerized Tomosynthesis of Dental Tissues," Oral Surgery Oral Medicine Oral Pathology Oral Radiology and Endodontics **56,** 206–214 (1983).

[7] A. Macovski, *Medical Imaging Systems* (Prentice Hall, New Jersey, 1983).

[8] S. J. Carter, J. J. Martin, J. H. Middlemiss, and F. G. M. Ross, "Polytome Tomography," Clinical Radiology **14,** 405–413 (1963).

[9] L. Stanton, "Conventional Tomography," In *Radiology: Diagnosis-Imaging-Intervention*, J. M. Taveras and J. T. Ferrucci, eds.,**3,** Ch. 12 (J.B. Lippincott Company, Philadelphia, PA, 1988).

[10] J. Rowlands and S. Kasap, "Amorphous Semiconductors Usher in Digital X-ray Imaging," Physics Today **50,** 24–30 (1997).

[11] H. G. Chotas, J. T. Dobbins III, and C. E. Ravin, "Principles of Digital Radiography with Large-Area, Electronically Readable Detectors: A Review of the Basics," Radiology **210,** 595–599 (1999).

[12] L. Antonuk, Y. El-Mohri, J. Siewerdsen, J. Yorkston, W. Huang, V. Scarpine, and R. Street, "Empirical Investigation of the Signal Performance of a High-Resolution, Indirect Detection, Active Matrix Flat-Panel Imager (AMFPI) for Fluoroscopic and Radiographic Operation," Medical Physics **24,** 51–70 (1997).

[13] D. Sashin and E. Sternglass, "The Role of Solid State Imaging Devices in the Future of Radiography," In *Electronic Imaging in Medicine*, pp. 130–144 (American Institute of Physics, New York, New York, 1984).

[14] S. Vedantham *et al.*, "Full Breast Digital Mammography with an Amorphous Silicon-Based Flat Panel Detector: Physical Characteristics of a Clinical Prototype," Medical Physics **27,** 558–567 (2000).

[15] H. E. Johns and J. R. Cunningham, *The Physics of Radiology* (Thomas, Springfield, IL, 1983).

[16] R. Fahrig and D. Holdsworth, "Three-Dimensional Computed Tomographic Reconstruction Using a C-arm Mounted XRII: Correction of Image Intensifier Distortion," Medical Physics **24,** 1097–1106 (1997).

[17] P. van der Zwet, D. Meyer, and J. Reiber, "Automated and Accurate Assessment of the Distribution, Magnitude, and Direction of Pincushion Distortion in Angiographic Images," Investigative Radiology **30,** 204–213 (1995).

[18] P. S. Cho, R. H. Johnson, and T. W. Griffin, "Cone-Beam CT for Radiotherapy Applications," Physics in Medicine and Biology **40,** 1863–1883 (1995).

[19] S. A. Feig and M. Yaffe, "Digital Mammography," RadioGraphics **18,** 893–901 (1998).

[20] P. R. Granfors and R. Aufrichtig, "Performance of a 41x41-cm^2 Amorphous Silicon Flat Panel X-ray Detector for Radiographic Imaging Applications," Medical Physics **27,** 1324–1331 (2000).

[21] W. Que and J. Rowlands, "X-ray Imaging Using Amorphous Selenium: Inherent Spatial Resolution," Medical Physics **22,** 365–374 (1995).

[22] L. T. Niklason *et al.*, "Digital Tomosynthesis in Breast Imaging," Radiology **205,** 399–406 (1997).

[23] R. L. Webber, H. R. Underhill, and R. I. Freimanis, "A Controlled Evaluation of Tuned-Aperture Computed Tomography Applied to Digital Spot Mammography," Journal of Digital Imaging **13,** 90–97 (2000).

[24] R. L. Webber and J. K. Messura, "An In Vivo Comparison of Diagnostic Information Obtained from Tuned-Aperture Computed Tomography and Conventional Dental Radiographic Imaging Modalities," Oral Surgery Oral Medicine Oral Pathology Oral Radiology and Endodontics **88,** 239–247 (1999).

[25] G. M. Stiel, L. S. G. Stiel, and C. A. Nienaber, "Potential of Digital Flashing Tomosynthesis for Angiocardiographic Evaluation," Journal of Digital Imaging **5,** 194–205 (1992).

[26] J. T. Dobbins III, R. L. Webber, and S. M. Hames, "Tomosynthesis for Improved Pulmonary Nodule Detection," In *Supplement to Radiology, 1998 Scientific Program, Radiological Society of North America,* p. 280 (1998).

[27] R. D. Zwicker and N. A. Atari, "Transverse Tomosynthesis on a Digital Simulator," Medical Physics **24,** 867–871 (1997).

[28] G. Messaris, Z. Kolitsi, C. Badea, and N. Pallikarakis, "Three-Dimensional Localisation Based on Projectional and Tomographic Image Correlation: An Application for Digital Tomosynthesis," Medical Engineering & Physics **21,** 101–109 (1999).

[29] Z. Kolitsi, G. Panayiotakis, V. Anastassopoulos, A. Scodras, and N. Pallikarakis, "A Multiple Projection Method for Digital Tomosynthesis," Medical Physics **19,** 1045–1050 (1992).

[30] C. Badea, Z. Kolitsi, and N. Pallikarakis, "A Wavelet-Based Method for Removal of Out-of-Plane Structures in Digital Tomosynthesis," Computerized Medical Imaging and Graphics **22,** 309–315 (1998).

[31] G. Lauritsch and W. H. Härer, "A Theoretical Framework for Filtered Backprojection in Tomosynthsis," Proceedings of the SPIE Medical Imaging Conference, Image Processing **3338,** 1127–1137 (1998).

[32] R. Fahrig and D. Holdsworth, "Three-Dimensional Computed Tomographic Reconstruction Using a C-arm Mounted XRII: Image-Based Correction of Gantry Motion Nonidealities," Medical Physics **27,** 30–38 (2000).

[33] J. A. Concepcion, J. D. Carpinelli, G. Kuo-Petravic, and S. Reisman, "CT Fan Beam Reconstruction with a Nonstationary Axis of Rotation," IEEE Transactions on Medical Imaging **11,** 111–116 (1992).

[34] C. R. Crawford, G. T. Gullberg, and B. M. Tsui, "Reconstruction for Fan Beam with an Angular-Dependent Displaced Center-of-Rotation," Medical Physics **15,** 67–71 (1988).

[35] A. Rougée, C. Picard, C. Ponchut, and Y. Trousset, "Geometrical Calibration of X-Ray Imaging Chains for Three-Dimensional Reconstructions," Computerized Medical Imaging and Graphics **17,** 295–300 (1993).

[36] J. Esthappan, H. Harauchi, and K. R. Hoffman, "Evaluation of Imaging Geometries Calculated from Biplane Images," Medical Physics **25,** 965–975 (1998).

[37] K. R. Hoffmann, J. Esthappan, S. Li, and C. Pelizzari, "A Simple Techniuque for Calibrating Imaging Geometries," Proceedings of the SPIE Medical Imaging Conference, Image Processing **2708,** 371–376 (1996).

[38] G. T. Gullberg, B. M. W. Tsui, C. R. Crawford, J. G. Ballard, and J. T. Hagius, "Estimation of Geometrical Parameters and Collimator Evaluation for Cone Beam Tomography," Medical Physics **17,** 264–272 (1990).

[39] P. Rizo, P. Grangeat, and R. Guillemaud, "Geometric Calibration Method for Multiple-Head Cone-Beam SPECT System," IEEE Transactions on Nuclear Science **41,** 2748–2760 (1994).

[40] A. V. Bronnikov, "Virtual Alignment of X-Ray Cone-Beam Tomography System Using Two Calibration Aperture Measurements," Optical Engineering **38,** 381–386 (1999).

[41] R. L. Webber, "Self-Calibrated Tomosynthetic, Radiographic-Imaging System, Method, and Device," U.S. Patent # 5,668,844 (1997).

[42] R. L. Webber, "Method and System for Creating Task-Dependent Three-Dimensional Images," U.S. Patent # 6,081,577 (2000).

[43] R. Fahrig, A. Fox, and D. Holdsworth, "Characterization of a C-arm Mounted XRII for 3D Image Reconstruction During Interventional Neuroradiology," Proceedings of the SPIE Medical Imaging Conference, Image Processing **2708,** 30–38 (1996).

[44] W. H. Press, S. A. Teukolsky, W. T. Vetterling, and B. P. Flannery, *Numerical Recipes in C: The Art of Scientific Computing* (Cambridge University Press, New York, 1992).

[45] U. E. Ruttiman, X. Qi, and R. L. Webber, "An Optimal Synthetic Aperture for Circular Tomosynthesis," Medical Physics **16,** 398–405 (1989).

[46] D. N. Ghosh Roy, R. A. Kruger, B. Yih, and P. Del Rio, "Selective Plane Removal in Limited Angle Tomographic Imaging," Medical Physics **12,** 65–70 (1985).

[47] N. J. Pelc, Ph.D. thesis, Harvard University, Boston, Massachusetts, 1979.

[48] A. Papoulis, *Probability, Random Variables, and Stochastic Processes* (McGraw-Hill, New York, 1991), p. 385.

[49] P. Haaker, E. Klotz, R. Koppe, R. Linde, and H. Möller, "A New Digital Tomosynthesis Method with Less Artifacts for Angiography," Medical Physics **12,** 431–436 (1985).

[50] S. H. Landis, T. Murray, S. Bolden, and P. A. Wingo, "Cancer Statistics, 1998," CA - A Cancer Journal for Clinicians **48,** 6–29 (1998).

[51] J. C. Chang, "A Review of Breast Cancer Chemoprevention," Biomedicine & Pharmacotherapy **52,** 133–136 (1998).

[52] J. F. Forbes, "The Incidence of Breast Cancer: The Global Burden, Public Health Considerations," Seminars in Oncology **24,** S1–20–S1–35 (1997).

[53] L. M. Apantaku, "Breast Cancer Diagnosis and Screening," American Family Physician **62,** 596–602 (2000).

[54] M. Primic-Zakelj, "Screening Mammography for Early Detection of Breast Cancer," Annals of Oncology **10,** Suppl 6, S121–S127 (1999).

[55] C. J. Baines *et al.*, "Sensitivity and Specificity of First Screen Mammography in the Canadian National Breast Screening Study: A Preliminary Report from Five Centers," Radiology **160,** 295–298 (1986).

[56] L. W. Bassett, D. H. Bunnell, R. Jahanshahi, R. H. Gold, R. D. Arndt, and J. Linsman, "Breast Cancer Detection: One Versus Two Views," Radiology **165,** 95–97 (1987).

[57] R. E. Bird, T. W. Wallace, and B. C. Yankaskas, "Analysis of Cancers Missed at Screening Mammography," Radiology **184,** 613–617 (1992).

[58] E. A. Sickles, "Breast Calcifications: Mammographic Evaluation," Radiology **160,** 289–293 (1986).

[59] D. Franceschi, J. Crowe, R. Zollinger, R. Duchesneau, R. Shenk, G. Stefanek, and J. M. Shuck, "Biopsy of the Breast for Mammographically Detected Lesions," Surgery Gynecology & Obsetrics **171,** 449–455 (1990).

[60] *Mammography Quality Control Manual*, American College of Radiology, Reston, Virginia, 1999.

[61] J. Liu, Ph.D. thesis, Stanford University, Palo Alto, California, 1991.

[62] *ULTRANET SA Operator Manual*, General Electric Medical Systems, Milwaukee, Wisconsin, 1996.

[63] M. J. DeVivo, "Causes and Costs of Spinal Cord Injury in the United States," Spinal Cord **35,** 809–813 (1997).

[64] J. Lasfargues, D. Custis, F. Morrone, J. Carswell, and T. Nguyen, "A Model for Estimating Spinal Cord Injury Prevalence in the United States," Paraplegia **33,** 62–68 (1995).

[65] M. Berkowitz, "Assessing the Socioeconomic Impact of Improved Treatment of Head and Spinal Cord Injuries," Journal of Emergency Medicine **11,** 63–67 (1993).

[66] M. D. Grossman, P. M. Reilly, T. Gillett, and D. Gillett, "National Survey of the Incidence of Cervical Spine Injury and Approach to Cervical Spine Clearance in U.S. Trauma Centers," Journal of Trauma **47,** 684–690 (1999).

[67] J. W. Davis, D. L. Phreaner, D. B. Hoyt, and R. C. Mackersie, "The Etiology of Missed Cervical Spine Injuries," Journal of Trauma **34,** 342–346 (1993).

[68] R. M. Vandemark, "Radiology of the Cervical Spine in Trauma Patients: Practice Pitfalls and Recommendations for Improving Efficiency and Communication," American Journal of Roentgenology **155,** 465–472 (1990).

[69] S. E. Mirvis, J. N. Diaconis, P. A. Chirico, B. I. Reiner, J. N. Joslyn, and P. Militello, "Protocol-Driven Radiologic Evaluation of Suspected Cerivcal Spine Injury: Efficacy Study," Radiology **170,** 831–834 (1989).

[70] T. E. Keats *et al.*, "Cervical Spine Trauma," In *ACR Appropriateness Criteria*, pp. 243–246 (American College of Radiology, Reston, Virginia, 2000).

[71] O. C. West, M. M. Anbari, T. K. Pilgram, and A. J. Wilson, "Acute Cervical Spine Trauma: Diagnostic Performance of Single-View Versus Three-View Radiographic Screening," Radiology **204,** 819–823 (1997).

[72] R. H. Daffner, *Imaging of Vertebral Trauma* (Lippincrott-Raven, Philadelphia, PA, 1996), pp. 51–94.

[73] B. L. Hart, W. W. Orrison Jr., and E. C. Benzel, "Imaging Spinal Trauma," In *SPINE: State of the Art Reviews*, **9,** 93–118 (Hanley & Belfus, Inc., Philadelphia, PA, 1995).

[74] J. H. Harris Jr. and S. E. Mirvis, *The Radiology of Acute Cervical Spine Trauma* (Williams & Wilkins, Baltimore, MD, 1996), pp. 180–211.

[75] B. Freemyer, R. Knopp, J. Piche, L. Wales, and J. Williams, "Comparison of Five-View and Three-View Cervical Spine Series in the Evaluation of Patients with Cervical Trauma," Annals of Emergency Medicine **18,** 818–821 (1989).

[76] L. D. Russin and F. C. Guinto Jr., "Multidirectional Tomography in Cervical Spine Injury," Journal of Neurosurgery **45,** 9–11 (1976).

[77] K. R. Maravilla, P. R. Cooper, and F. H. Sklar, "The Influence of Thin-Section Tomography on the Treatment of Cervical Spine Injuries," Radiology **127,** 131–139 (1978).

[78] T. E. Gammal and B. S. Brooks, "Radiologic Evaluation of the Craniovertebral Junction," In *Radiology: Diagnosis-Imaging-Intervention*, J. M. Taveras and J. T. Ferrucci, eds.,**3,** Ch. 79 (J.B. Lippincott Company, Philadelphia, PA, 1988).

[79] S. Ehara, G. Y. El-Khoury, and C. R. Clark, "Radiologic Evaluation of Dens Fracture: Role of Plain Radiography and Tomography," Spine **17,** 475–479 (1992).

[80] M. Baumgarten, W. Mouradian, D. Boger, and R. Watkins, "Computed Axial Tomography in C1-C2 Trauma," Spine **10,** 187–192 (1985).

[81] T. M. Link, G. Schuierer, A. Hufendiek, C. Horch, and P. E. Peters, "Substantial Head Trauma: Value of Routine CT Examinations of the Cervicocranium," Radiology **196,** 741–745 (1995).

[82] M. F. Blacksin and H. J. Lee, "Frequency and Significance of Fractures of the Upper Cervical Spine Detected by CT in Patients with Severe Neck Trauma," American Journal of Roentgenology **165,** 1201–1204 (1995).

[83] D. B. Nuñez, A. Zuluaga, D. A. Fuentes-Bernardo, L. A. Rivas, and J. L. Becerra, "Cervical Spine Trauma: How Much More Do We Learn by Routinely Using Helical CT?," RadioGraphics **16,** 1307–1318 (1996).

[84] C. R. Clark, C. M. Igram, G. Y. El-Khoury, and S. Ehara, "Radiographic Evaluation of Cervical Spine Injuries," Spine **13,** 742–747 (1988).

[85] C. A. Ridpath, A. J. Wilson, S. G. Langer, F. A. Mann, and J. C. Hunter, "Cervical Spine Tomography with an Angiographic C-arm," Radiology **211,** 882–885 (1999).

[86] R. M. Vandemark, M. E. Fay, F. R. Porter, and G. A. Johnson, "Digital Image-Intensifier Radiography at a Level I Trauma Center," American Journal of Roentgenology **168,** 944–946 (1997).

[87] W. C. G. Peh, P. Cheng, and F. L. Chan, "Direct Coronal Computed Tomography of the Upper Cervical Spine," Spine **20,** 972–974 (1995).

[88] S. J. Lipson, "Fractures of the Atlas Associated with Fractures of the Odontoid Process and Transverse Ligament Ruptures," Journal of Bone and Joint Surgery **59A,** 940–943 (1977).

[89] M. D. Miller, J. A. Gehweiler, S. Martinez, O. P. Charlton, and R. H. Daffner, "Significant New Observations on Cervical Spine Trauma," American Journal of Roentgenology **130,** 659–663 (1978).

[90] J. H. Woodring and C. Lee, “The Role and Limitations of Computed Tomographic Scanning in the Evaluation of Cervical Trauma,” Journal of Trauma **33,** 698–708 (1992).

[91] G. M. Stevens, R. Saunders, and N. J. Pelc, “Alignment of a Volumetric Tomography System,” Medical Physics (submitted).

[92] G. M. Stevens, R. Fahrig, and N. J. Pelc, “Filtered Backprojection for Modifying the Impulse Response of Circular Tomosynthesis,” Medical Physics (submitted).

[93] G. M. Stevens, R. Fahrig, and N. J. Pelc, “Filtered-Backprojection for Improved Blurring in Circular Tomosynthesis,” In *Supplement to Radiology, 2000 Scientific Program, Radiological Society of North America*, p. 314 (2000).

[94] G. M. Stevens and N. J. Pelc, “Depth-Segmented Detector for X-ray Absorptiometry,” Medical Physics **27,** 1174 – 1184 (2000).

[95] L. A. Lehmann, R. E. Alvarez, A. Macovski, W. R. Brody, N. J. Pelc, S. J. Riederer, and A. L. Hall, “Generalized Image Combinations in Dual kVp Digital Radiography,” Medical Physics **8,** 659–667 (1981).

[96] L. T. Niklason, N. M. Hickey, D. P. Chakraborty, E. A. Sabbagh, M. V. Yester, R. G. Fraser, and G. T. Barnes, “Simulated Pulmonary Nodules: Detection with Dual-Energy Digital versus Conventional Radiography,” Radiology **160,** 589–593 (1986).

[97] T. Asaga, S. Chiyasu, S. Mastuda, H. Mastuura, H. Kato, M. Ishida, and T. Komaki, “Breast Imaging: Dual-Energy Projection Radiography with Digital Radiography,” Radiology **164,** 869–870 (1987).

[98] D. T. Baran, K. G. Faulkner, H. K. Genant, P. D. Miller, and R. Pacifici, “Diagnosis and Management of Osteoporosis: Guidelines for the Utilization of Bone Densitometry,” Calcified Tissue International **61,** 433–440 (1997).

[99] S. L. Silverman, “Calcitonin,” American Journal of Medical Science **313,** 13–16 (1997).

[100] U. A. Liberman *et al.*, "Effect of Oral Alendronate on Bone Mineral Density and the Incidence of Fractures in Postmenopausal Osteoporosis," New England Journal of Medicine **333,** 1437–1443 (1995).

[101] A. A. Licata, "Bisphosphonate Therapy," American Journal of Medical Science **313,** 17–22 (1997).

[102] J. A. Sorenson, P. R. Duke, and S. W. Smith, "Simulation Studies of Dual-Energy X-ray Absorptiometry," Medical Physics **16,** 75–80 (1989).

[103] G. T. Barnes, R. A. Sones, M. M. Tesic, D. R. Morgan, and J. N. Sanders, "Detector for Dual-Energy Digital Radiography," Medical Physics **156,** 537–540 (1985).

[104] H. N. Cardinal and A. Fenster, "Theoretical Optimization of a Split Septaless Xenon Ionization Detector for Dual-Energy Chest Radiography," Medical Physics **15,** 167–180 (1988).

[105] D. L. Ergun, C. A. Mistretta, D. E. Brown, R. T. Bystrianyk, W. K. Sze, F. Kelcz, and D. P. Naidich, "Single-Exposure Dual-Energy Computed Radiography: Improved Detection and Processing," Radiology **174,** 243–249 (1990).

[106] D. R. Morgan, R. A. Sones, and G. T. Barnes, "Performance Characteristics of a Dual-Energy Detector for Digital Scan Projection Radiography," Medical Physics **14,** 728–735 (1987).

[107] D. M. Gauntt and G. T. Barnes, "X-Ray Tube Potential, Filtration, and Detector Considerations in Dual-Energy Chest Radiography," Medical Physics **21,** 203–218 (1994).

[108] D. P. Chakraborty and G. T. Barnes, "An Energy Sensitive Cassette for Dual-Energy Mammography," Medical Physics **16,** 7–13 (1989).

[109] F. Kelcz, P. M. Joseph, and S. K. Hilal, "Noise Considerations in Dual Energy CT Scanning," Medical Physics **6,** 418–425 (1979).

[110] J. Mandel, *The Statistical Analysis of Experimental data* (Dover Publications, New York, 1964).

[111] National Institute of Standards and Technology, "http://physics.nist.gov/PhysRefData/XrayMassCoef/tab3.html,", website.

[112] National Institute of Standards and Technology, "http://physics.nist.gov/PhysRefData/XrayMassCoef/tab2.html,", website.

[113] E. Storm *et al.*, "Calculated Bremsstrahlung Spectra from Thick Tungsten targets," Physical Review A **5,** 2328–2338 (1972).

[114] N. A. Dyson, *X-Rays in Atomic and Nuclear Physics* (Longman, London, 1973).